

AD A 049054

AD No.   
 DDC FILE COPY

RADC-TR-77-385  
Final Technical Report  
November 1977



# IR ATMOSPHERIC MEASUREMENTS

Avco Everett Research Laboratory, Inc.

Sponsored by  
Defense Advanced Research Projects Agency (DoD)  
ARPA Order No. 2646



Approved for public release; distribution unlimited.

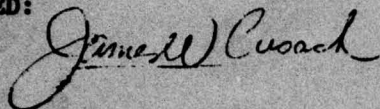
The views and conclusions contained in this document are those of the authors and should not be interpreted as necessarily representing the official policies, either expressed or implied, of the Defense Advanced Research Projects Agency or the U. S. Government.

ROME AIR DEVELOPMENT CENTER  
Air Force Systems Command  
Griffiss Air Force Base, New York 13441

This report has been reviewed by the RADC Information Office (OI) and is releasable to the National Technical Information Service (NTIS). At NTIS it will be releasable to the general public, including foreign nations.

RADC-TR-77-385 has been reviewed and is approved for publication.

APPROVED:

A handwritten signature in cursive script, reading "James W. Cusack".

JAMES W. CUSACK  
Project Engineer

If your address has changed or if you wish to be removed from the RADC mailing list, or if the addressee is no longer employed by your organization, please notify RADC (OCSE) Griffiss AFB NY 13441. This will assist us in maintaining a current mailing list.

Do not return this copy. Retain or destroy.



⑨ Final Technical rept. 29 Jun 75-31 May 77

⑥ IR ATMOSPHERIC MEASUREMENTS.

⑪ Nov 77

⑩ H. P. / Kent  
P. F. / Kellen

⑫ 113 p.

⑮ Contractor: Avco Everett Research Laboratories  
Contract Number: F30602-75-C-0235 WARPA Order-2646  
Effective Date of Contract: 29 June 1975  
Contract Expiration Date: 31 May 1977  
Short Title of Work: IR Atmospheric Measurements  
Program Code Number: 5E20  
Period of Work Covered: June 1975 - May 1977

⑬ 2646

Principal Investigators: H. P. Kent  
P. F. Kellen  
Phone: 617 389-3000 x282  
Project Engineer: James W. Cusack  
Phone: 315 330-3145

⑭  $\phi 3$

⑰ RADC

⑱ TR-77-385

Approved for public release; distribution unlimited.

This research was supported by the Defense Advanced Research Projects Agency of the Department of Defense and was monitored by James W. Cusack (OCSE), Griffiss AFB NY 13441 under Contract F30602-75-C-0235.

048450

mt

## UNCLASSIFIED

SECURITY CLASSIFICATION OF THIS PAGE (When Data Entered)

REPORT DOCUMENTATION PAGE		READ INSTRUCTIONS BEFORE COMPLETING FORM
1. REPORT NUMBER RADC-TR-77-385	2. GOVT ACCESSION NO.	3. RECIPIENT'S CATALOG NUMBER
4. TITLE (and Subtitle)  IR ATMOSPHERIC MEASUREMENTS	5. TYPE OF REPORT & PERIOD COVERED Final Technical Report 29 June 1975 - 31 May 1977	
	6. PERFORMING ORG. REPORT NUMBER N/A	
7. AUTHOR(s)  H. P. Kent P. F. Kellen	8. CONTRACT OR GRANT NUMBER(s)  F30602-75-C-0235	
9. PERFORMING ORGANIZATION NAME AND ADDRESS Avco Everett Research Laboratories 2835 Revere Beach Parkway Everett MA 02149	10. PROGRAM ELEMENT, PROJECT, TASK AREA & WORK UNIT NUMBERS  62301E 26460306	
11. CONTROLLING OFFICE NAME AND ADDRESS Defense Advanced Research Projects Agency 1400 Wilson Boulevard Arlington VA 22209	12. REPORT DATE November 1977	
	13. NUMBER OF PAGES 26	
14. MONITORING AGENCY NAME & ADDRESS (if different from Controlling Office) Rome Air Development Center ((OCSE) Griffiss AFB NY 13441	15. SECURITY CLASS. (of this report)  Unclassified	
	15a. DECLASSIFICATION/DOWNGRADING SCHEDULE N/A	
16. DISTRIBUTION STATEMENT (of this Report) Approved for public release; distribution unlimited.		
17. DISTRIBUTION STATEMENT (of the abstract entered in Block 20, if different from Report) Same		
18. SUPPLEMENTARY NOTES RADC Project Engineer: James W. Cusack (OCSE)		
19. KEY WORDS (Continue on reverse side if necessary and identify by block number) Atmospheric transmission      Atmospheric refraction structure Sky noise      LWIR 'seeing' Atmospheric radiance      IR astronomy $\lambda/\Delta\lambda$ Satellite observables      IR adaptive optics      microns		
20. ABSTRACT (Continue on reverse side if necessary and identify by block number) 1) Apparent angle of arrival fluctuations for atmosphere-perturbed irradiance from bright astronomical sources was recorded with a view to determining refractive structure scaling with wavelength. Measurements were made with low spectral dispersion, $2.5 \leq \lambda/\Delta\lambda \leq 10$ , between 1.3 and 21 $\mu\text{m}$ . Some results are presented.		

(Cont'd)

DD FORM 1473  
1 JAN 73

EDITION OF 1 NOV 65 IS OBSOLETE

UNCLASSIFIED

SECURITY CLASSIFICATION OF THIS PAGE (When Data Entered)



UNCLASSIFIED

SECURITY CLASSIFICATION OF THIS PAGE(When Data Entered)

(20)

2) Random intensity scintillation observed in star and satellite LWIR signal records is apparently related to object size. The relation may be used to distinguish between point and extended objects of equal apparent brightness. Data review results are presented.

3) The gross self-radiance of atmosphere may be measured to permit real-time computation of transmission. In circumstances where weather changes invalidate extinction measures, the technique offers promise of increasing credibility of conjectures made from observations of satellites. Preliminary results of tests are presented.

4) Modifications to an existing LWIR radiometer permit long period signal averaging and enable the thermal signatures of deep-space satellites to be measured. Some results are presented.

UNCLASSIFIED

SECURITY CLASSIFICATION OF THIS PAGE(When Data Entered)

## TABLE OF CONTENTS

<u>Section</u>	<u>Page</u>
List of Illustrations	3
1.0 INTRODUCTION	7
1.1 Purpose	7
1.2 Background	7
1.3 Need	8
1.4 Measuring Concept	8
1.5 Hardware Description	9
1.6 Measurement Constraints	15
2.0 CALIBRATION	21
3.0 DATA DISCUSSION	33
 <u>Appendices</u>	
A Atmospheric Absorption	71
B Twinkle	101

ACCESSION for		
NTIS	Write Section	<input checked="" type="checkbox"/>
DDC	Buff Section	<input type="checkbox"/>
UNANNOUNCED		<input type="checkbox"/>
JUSTIFICATION		
BY _____		
DISTRIBUTION/AVAILABILITY CODES		
Dist.	AVAIL.	SPECIAL
A		

(The reverse of this page is blank)



## LIST OF ILLUSTRATIONS

<u>Figure</u>		<u>Page</u>
1	Hartmann Screen	10
2	Optical Layout	12
3	AMTA Dewar	13
4	Subaperture Spot Size	14
5	Detectable Wavefront Tilt	17
6	Observational Particulars, Terrestrial Planets	18
7	Diffraction Blur Size	19
8	Point Source Calibration	23
	a) Point Source Temperature	
	b) Exitance Equivalent $H_{AP}$	
9	Image Displacement Response	24
	a) Typical Polar Detector	
	b) Typical Declination Detector	
10	80% Encircled Energy	25
11	Predicted Displacement Response, 11 $\mu\text{m}$	26
12	Mercury Waning	28
13	Angular Scaling Layout	31
14	Displacement Calibration	32
15	Raw Data	34
16	Filter #5 Data, Run 13	35
17	Filter #5 Data, Run 21	37
18	48-Inch Mount Declination Response	38

<u>Figure</u>		<u>Page</u>
19	Filter #5 Data, Run 14	39
20	Filter #5 Data, Run 16	40
21	Filter #4 Data, Run 78	42
22	Filter #4 Data, Run 79	43
23	Filter #4 Data, Run 30	44
24	Filter #4 Data, Run 31	45
25	Filter #4 Data, Run 33	46
26	Filter #4 Data, Run 32	47
27	Refractive Structure PSD	49
28	Refractive Structure PSD	50
29	Filter #5 Data, Run 14	51
30	Filter #5 Data, Run 16	52
31	Filter #5 Data, Run 22	53
32	Filter #5 Data, Run 23	54
33	Filter #5 Data, Run 118	55
34	Filter #3 Data, Run 75	57
35	Filter #3 Data, Run 76	58
36	Filter #1 Data, Run 54	59
37	Filter #1 Data, Run 56	60
38	Filter #9 Data, Run 97	61
39	Filter #9 Data, Run 98	62
40	Filter #9 Data, Run 99	63
41	Tilt Scaling Summary	64
42	Four-Detector Autocorrelation, Run 125	67
43	Four-Detector Autocorrelation, Run 124	68



<u>Figure</u>		<u>Page</u>
44	Scintillation Spectral Density	69
45	Scintillation Spectral Density	70
A-1	Retrieving Contrast Features	75
A-2	AMTA Signal Processing for Long Integration	76
A-3	Molniya 1-19 Thermal Signature	80
A-4	Sky Radiance Measurement	86
A-5	AMTA Add-Ons for Long Duration Observations	87
A-6	AMTA Add-Ons for Long Integration and Atmospheric Transmission	88
A-7	Air Mass Related to Detector Output	91
A-8	Sensitivity with Slewing	96
B-1	Peegasus IR Twinkle	102
B-2	Satellite Observation Noise-In-Signal	105
B-3	Stellar Scintillation Related to Irradiance	106
B-4	Stellar Scintillation Related to Zenith Distance	107
B-5	AMOS Weather	109
B-6	IR Twinkle Data	110
B-7	Target Sizing with IR Twinkle	111
B-8	NEFD Related to Object Brightness	113

## 1.0 INTRODUCTION

### 1.1 PURPOSE

This report seeks to describe experiments performed in September 1976 with an existing LWIR sensor at the AMOS Observatory. The goal of these measurements is an estimate of wavelength scaling of angle-of-arrival fluctuations for radiant energy propagating via slant paths through the whole atmosphere. The overall object of this study is to provide information relative to defining physical limits imposed by turbulent atmosphere upon imaging and collimating systems, principally at LWIR wavelengths.

### 1.2 BACKGROUND

The angle of arrival experiment is part of a wider program of measurements begun under ARPA sponsorship, through their agents, RADC, in July 1975. In its entirety, the IR Atmospheric Measurements Program (Contract No. F30602-75-C-0235) also included: (2) real-time LWIR atmospheric absorptance determination; (3) a demonstration of the effectiveness of long period signal integration for distinguishing deep-space satellite signatures from gradients associated with intervening radiant atmosphere; (4) measurement of wavelength scaling of atmosphere affected point image spread function; and (5) measurement of the spectral broadening of 'monochromatic' (ultra stable CO<sub>2</sub> laser) radiation produced by propagation through the entire turbulent atmosphere. The equipments for accomplishing items (2) and (3) (which were designed and fabricated at AERL as part of this program) were left in place at AMOS and have been used subsequently in support of satellite observations. A brief description of this hardware and some preliminary results are presented in Appendix A and References (1) and (2).

In May 1976 reevaluation of then current needs and risks produced a decision to cancel items (4) and (5). The remaining experiments were rescheduled for earlier completion.

1. Avco Everett Research Laboratory Interim Report: IR Atmospheric Measurements, Contract No. F30602-75-C-0235 (December 1976).
2. Young, L.A., IR Radiation in a Real Tropical Atmosphere, p.77 (May 1977).



### 1.3 NEED

The projected performance of surveillance and other systems which depend upon LWIR radiative transfer over slant paths through the entire atmosphere are presently based upon theoretical extension of visual turbulence data obtained from observations of stars<sup>(3)</sup> and upon monochromatic measurements along horizontal paths. The detailed configuration of large adaptive-optic collectors and projectors for imaging through atmosphere will hinge upon the scale of refractive structure and no truly representative data for confirming the utility of theoretical scaling is available. Indeed there is some observational evidence which conflicts with prediction. (See Appendix B.)

### 1.4 MEASURING CONCEPT

The measuring principle for angle-of-arrival represents an extension of the familiar Hartmann test for determining the imaging performance of large telescopes in the field. In 1904 Hartmann<sup>(4)</sup> described a procedure, using bright stars, which is less subjective than the older knife-edge (Foucault testing) observation. He suggested masking the entrance of the telescope to be characterized with an opaque screen pierced with a carefully mapped pattern of smallish holes. When light from a distant point source is imaged by the masked optic a photographic plate, positioned some distance from focus, records a facsimile of the hole pattern as distorted by imperfections of the optic and random atmospheric refraction structure. Any measurable differences between the resulting photograph and the screen pattern are then used to trace rays from each hole and to characterize, thereby, the performance of the optic. Atmospheric effects are a nuisance which limit the precision of these tests. To average out refractive disturbances, produced by wind driven eddies, long exposures (typically greater than ten seconds) are made for optical testing.

---

3. Tatarskii, V.I., Effects of Turbulent Atmosphere on Wave Propagation  
NTIS TT68-50464 (1971).

4. Hartmann, J., Zeit. f. Instrum. 24 (1904).

We, on the other hand, sought to characterize the turbulent atmosphere. The quality of the optic, as long as it remained constant, was of little importance. This was accomplished by making, in effect, a great many short exposure records and using the difference between records to determine atmosphere induced fluctuations in the apparent direction of arrival of star light across the aperture.

### 1.5 HARDWARE DESCRIPTION

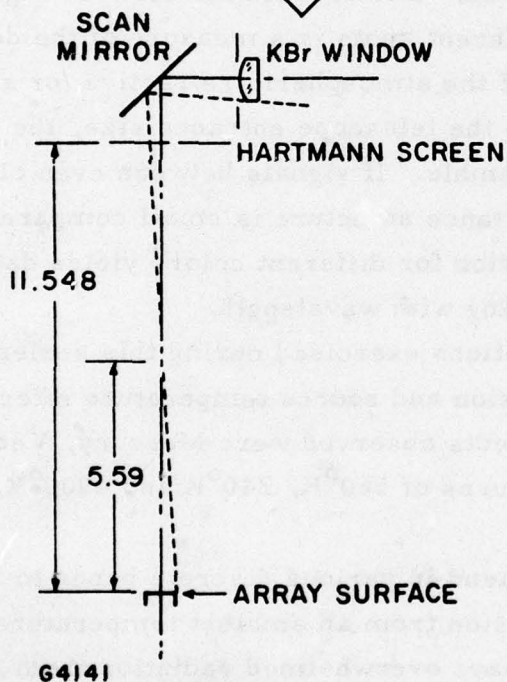
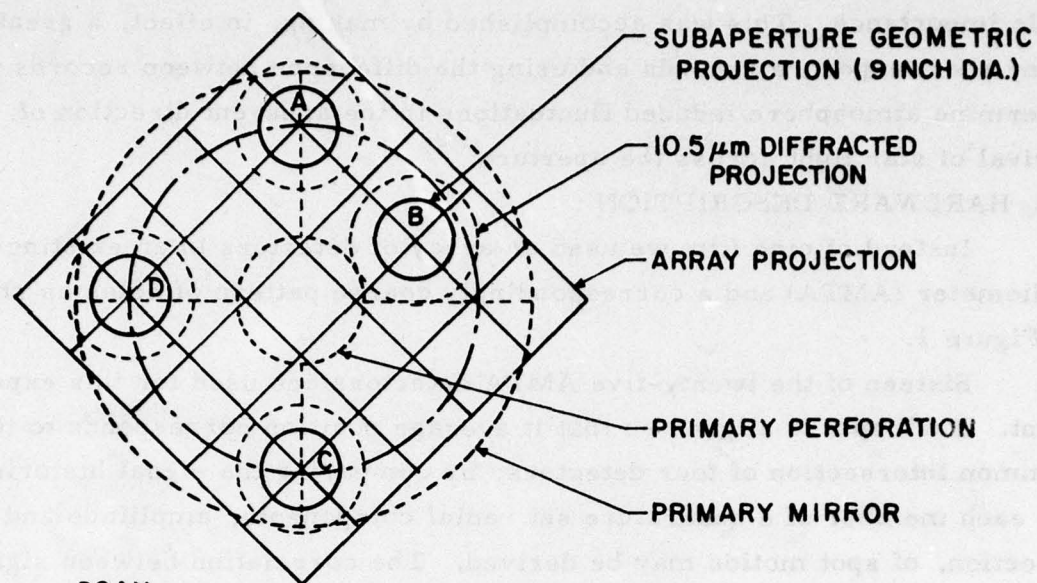
Instead of cine film we used an array of detectors in an existing radiometer (AMTA) and a correspondingly coarse pattern of holes as shown in Figure 1.

Sixteen of the twenty-five AMTA detectors are used for this experiment. Each spot is aligned so that its average position corresponds to the common intersection of four detectors; by comparing the signal histories for each member of a quadrature set radial components, amplitude and direction, of spot motion may be derived. The correlation between signal histories for detectors monitoring different spots is a measure of the degree to which spot motions are tethered. If the atmospheric refractive (or ray tilting) structure is large compared to the telescope entrance size, the spots ought to move as a tethered ensemble. If signals between even close spaced spots are uncorrelated, refractive structure is small compared to fifteen inches. Repeating the observation for different colors yields data for calculating structure function scaling with wavelength.

Table 1 lists the wavelength options exercised during this series of observations. Atmospheric transmission and source temperature effects are included. The three principal objects observed were Mercury, Venus and  $\alpha$  Bootis with effective temperatures of  $560^{\circ}\text{K}$ ,  $240^{\circ}\text{K}$  and  $4900^{\circ}\text{K}$ , respectively.

Because our measurements extend in various discrete bands to the LWIR (1.6 to  $21.5\ \mu\text{m}$ ), thermal emission from an ambient temperature mask in the entrance aperture would have overwhelmed radiation from even the most intense astronomical sources. Therefore, a small screen (detailed in Figure 2) refrigerated to  $40^{\circ}\text{K}$ , was positioned within the AMTA radiometer vacuum dewar as shown in Figure 3 near an image of the telescope pupil.





#### SAMPLING DISTANCES

COMBINATION	SEPARATION
A - B	17.1 inches
A - D	25.7
C - D	25.7
B - C	27.2
B - D	30.5
A - C	36.5

Figure 1 Hartmann Screen

TABLE 1. SPECTRAL OPTIONS

Source Temp	240°K		560°K		4900°K	
Filter #	$\lambda_{\text{eff}}$	$\Delta\lambda$	$\lambda_{\text{eff}}$	$\Delta\lambda$	$\lambda_{\text{eff}}$	$\Delta\lambda$
1	3.9 $\mu\text{m}$	0.42 $\mu\text{m}$	3.78 $\mu\text{m}$	0.67 $\mu\text{m}$	3.66 $\mu\text{m}$	0.81 $\mu\text{m}$
2	4.8	0.41	4.8	0.42		
3	8.74	0.91	8.70	0.98		
4	11.63	2.62	11.47	2.44		
5	11.04	3.55	10.51	3.81		
6	18.74	2.98	18.63	2.84		
9	4.26	1.02	3.75	1.10	1.6	0.62

Light imaged by the telescope is brought to focus again, after being spatially quantized by the screen, approximately midway between the screen and the detector array; see Figure 13. Focus was relocated by moving the radiometer reimaging mirror as shown in Figure 2. It was also necessary to move the screen and the pupil image so the former would mask interfering self-radiance of the warm scan mirror as shown in Figure 3 and this was accomplished by increasing the power of the KBr vacuum window. All these modifications were designed to be quickly reversible so the sensor could be restored, without degraded performance, to its normal measuring configuration. The holes in the screen were sized to project approximately eight inch diameter subapertures into the telescope entrance. Figure 4 illustrates the results of computations relating the diffracted hole projections in the array plane to effective entrance diameter for representative wavelengths. Detector spacing and the longest wavelength constrained the hole size. For each wavelength shown there is an effective entrance diameter below and above which the illuminated spot on the detectors increases in size due to physical and geometric optical effects, respectively. [Note: There are two curves for visible light representing absolutely still and normally turbulent (1.5 arcsecond "seeing") conditions. The Hartmann screens for telescope evaluation have two inch holes and test photographic plates, which are also exposed approximately six inches from focus, typically have .035 to .040 inch



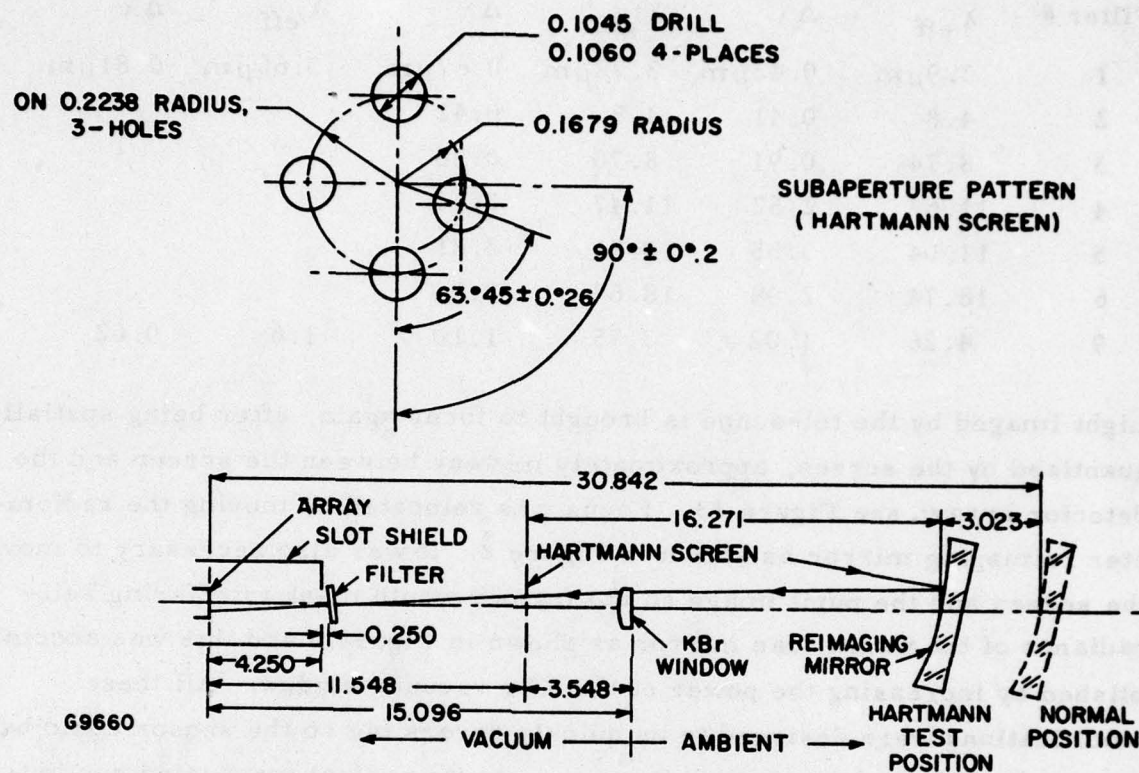


Figure 2 Optical Layout

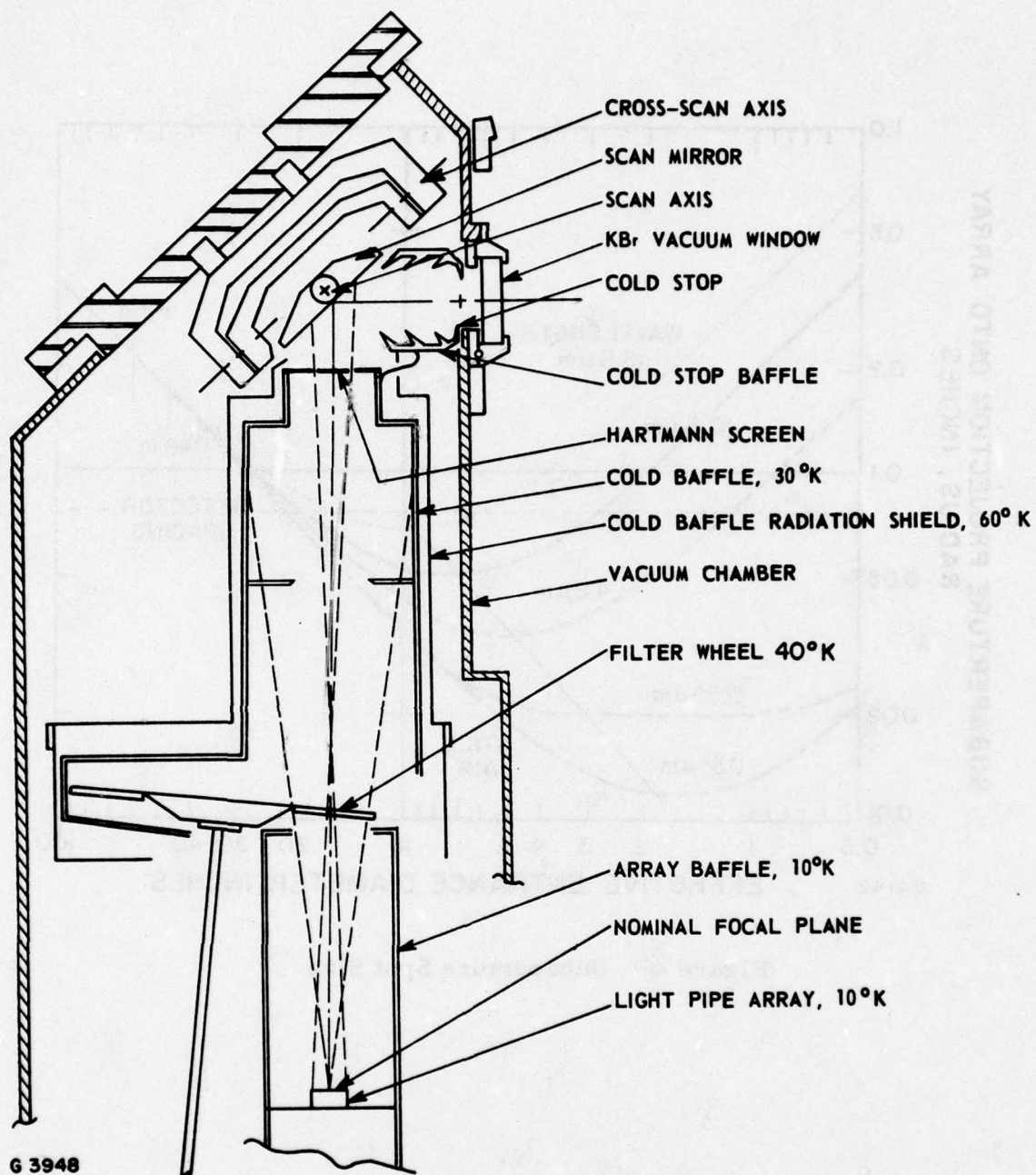


Figure 3 AMTA Dewar



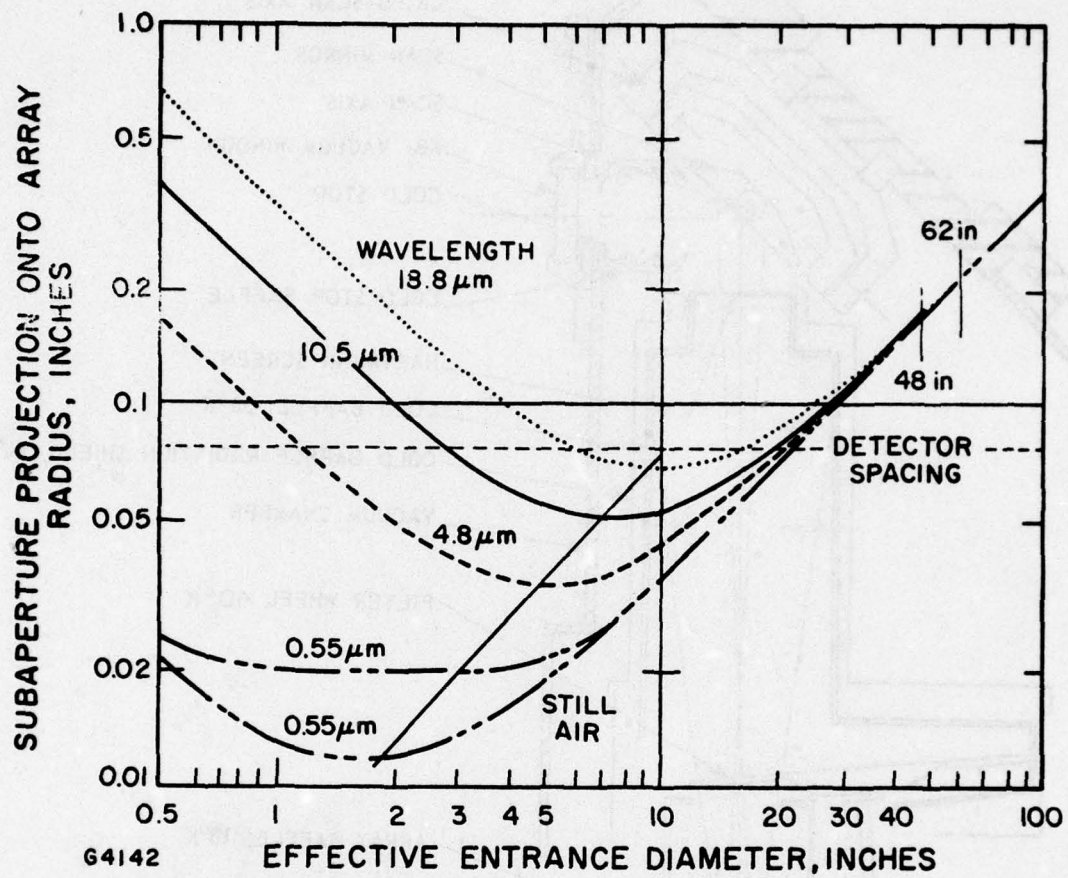


Figure 4 Subaperture Spot Size

diameter spots when seeing conditions are 'good.' Good seeing means no observable twinkle (unaided vision) above  $45^\circ$  elevation. ] The ordinal values in Figure 4 are radius for 80% encircled energy.

Signals from all twenty-five AMTA detectors are independently and simultaneously recorded on analog magnetic tape with AC bandwidth extending from 0.2 Hz to 4.4 kHz for each. Steady state values are not recorded and signal level is adjusted so that detector noise (sky radiance produced) may be retrieved from tape. Certain housekeeping information like Universal Time, spectral option (filter) number and telescope gimbal error are also recorded. Telescope line of sight wander during the experiment would, of course, produce correlated motion of the subaperture projections. To permit this effect to be unwound from the data, provisions for recording gimbal shaft-angle encoder error signals were made.

The AMOS telescopes are mounted in high speed ( $2^\circ$  per second) three-axis (azimuth, polar and declination rotations) gimbals. Shaft angle values for any two active components are read with 23 bit (0.15 arcseconds) resolution 1,000 times per second and compared with continuously recomputed desired values; the differences are converted to analog voltages. These, called 'mount error signals,' were patched to the analog sensor recorder for this experiment.

#### 1.6 MEASUREMENT CONSTRAINTS

Two identifiable sources of difficulty were anticipated: (a) mount servo instability, and (b) sensor refrigerator "thumping" which produces microphonic signals correlated between all detectors. The first named produces oscillatory or random (wind buffeting related) fine motion about the desired line of sight. If the telescope steering servo gains are set 'properly' the mount will oscillate between five and ten Hertz with an amplitude ranging between twenty and 'a few tenths' arcseconds. If the gains are backed off to decisively preclude oscillation the mount becomes compliant enough to respond to wind disturbance torques. Instability is generally confined to the declination axis; resonant or phase shift producing elements in the feedback loop had not been unambiguously identified in September. The effect is generally adjusted and left so as to produce little or no degradation for photometric or radiometric observations. We hoped to circumvent the



problem by using the error signal record and/or selecting favorable dome slot orientations and windless nights for observations.

Sensor microphonics, i. e., response to refrigerator component acceleration, affects high frequency (80 and 219 Hz) interference which we assumed would be in phase for all detectors. The effect is most pronounced for detectors far off the optical axis and is principally due to small vibration induced rocking of the scan mirror and to movement of the detector array itself. To reduce microphonic effects the scan mirror was blocked. This did reduce the effect but at insupportable cost; we needed to steer the beam with the scan mirror to establish initial alignment. Instead the problem was reduced during data processing by notching out at the principle offending frequencies.

Figure 5a/b relates tilt measuring sensitivity to source brightness. These plots are based upon calculated spot motion and upon noise equivalent flux measurements made two years ago for filters #5 and #6. Taking  $1/40$  wave of tilt with  $\pm 20\%$  measuring uncertainty as a goal leaves only a dozen candidate source objects.<sup>(5)</sup> Objects had (a) to be brighter than  $m_Q = -6$ ; (b) to be unresolvable by the eight inch subapertures at the wavelengths of interest; (c) be far enough from the sun to avoid heating the telescope's mirrors ( $> 12^\circ$ ) and finally; (d) be  $> 2^\circ$  from the moon to assure the possibility of visual guidance. We found that sensor NEFD performance had degraded by a factor of four to five from predictions based upon the old measurements and, in consequence, restricted our candidate list still further eliminating all but the terrestrial planets for LWIR observations and  $\alpha$  Boo for near IR. Figures 6 and 7 give geometric observational particulars for the planets and maximum allowable image size. Mars is sufficiently bright only for long wave measurements. Mercury is bright enough at all wavelengths during our September 1976 measurement slot but comes too close to the sun between the 14th and 24th days. Venus is bright enough also, but is of marginal size for the short wave observations.

---

5. AERL: Mission Instruction and Operation Plan #018 (attachment to A/OP-309) (July 1976).

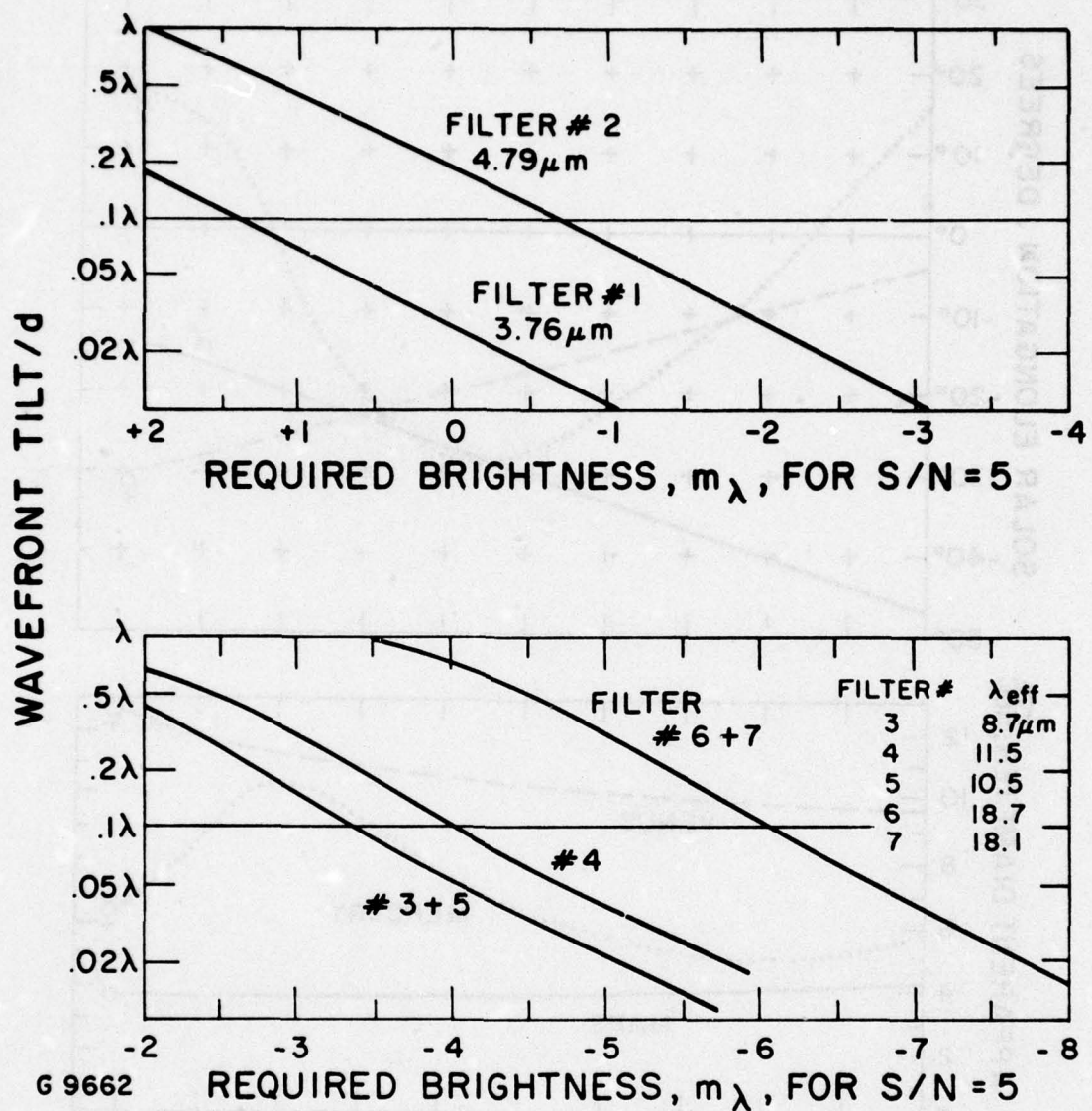
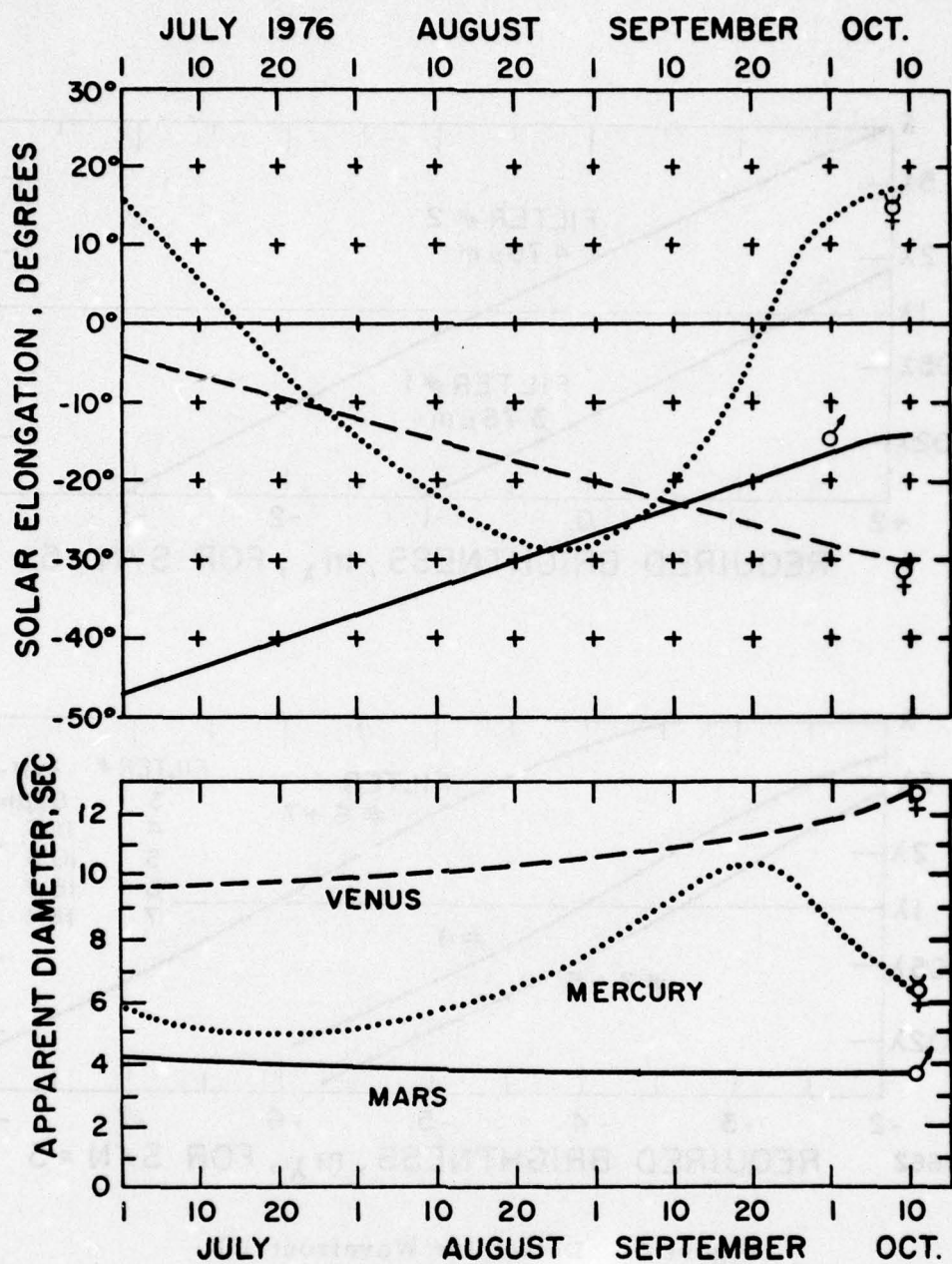


Figure 5 Detectable Wavefront Tilt





G3943

1976

Figure 6 Observational Particulars Terrestrial Planets

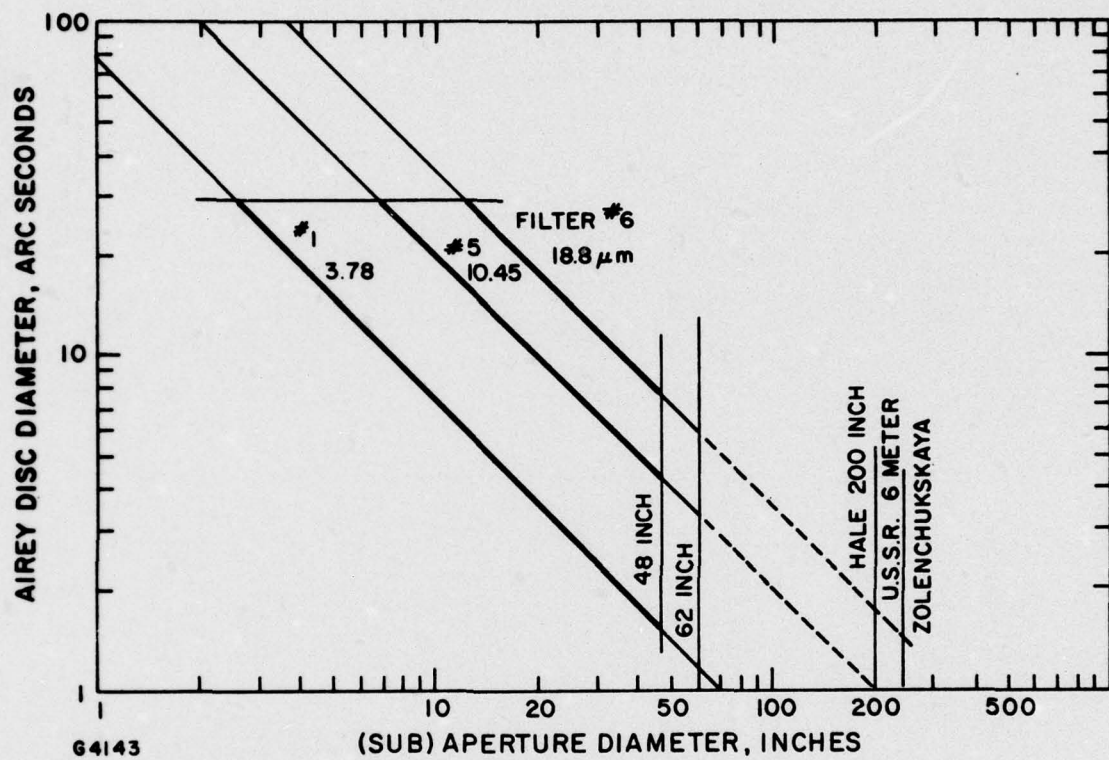


Figure 7 Diffraction Blur Size



The observations had to be terminated whether or not data was gathered by 16 September to permit restoring the sensor in preparation for satellite radiometric missions scheduled shortly thereafter.



## 2.0 CALIBRATION

To relate recorded observational data to angle of arrival, a 'point' radiance source, fitted with micrometer cross-slides, was positioned in the telescope cassegrain image surface to establish the relation between detector signals and image displacement. Tilt in microradians is given by  $\alpha_{\mu r} = \delta s / F$ ; where  $F$  and  $\delta s$  are effective focal length and off-axis image displacement, respectively. The cross-slide had sufficient range to permit changing apparent angle of arrival by  $\pm 0.5$  milliradians (polar and/or declination components) with resolution and resetability of approximately  $0.5 \mu r$ adians. A soldering iron, with the tip removed to provide a cavity six diameters deep, was used as a 'black' radiance source. [Note that only AC signals are recorded with low and high frequency corners at 0.2 Hz and 4 kHz, respectively. That is to say: a non-fibrillating and stationary star image produces no recorded signal. Any voltage changes recorded during stellar observations represent object scintillation or momentary displacements from the mean subaperture image position.] For calibration it was necessary to modulate the source. Accordingly, a room temperature shutter driven at 45 Hz was positioned between the point ( $10^{-3} \text{ cm}^2$ ) aperture and the hot cavity. Source temperature was adjusted to produce an image flux level in the same decade as that anticipated from the planet Mercury. Tape recordings were made with east-west and north-south displacements of 0, 1, 2, 4, 8, 12 and 20 microradians from the reference line of sight for AMTA filters #1, 3, 4, 6 and 9. The image was maintained at each displacement for one full minute to permit precise averaging. Exchanging a small frosted lamp for the soldering iron produces a visual image for the AMTA boresight TV camera display which could then be marked with a reference fiducial representing the quiescent line of sight. Planet and star images were brought to this mark during the course of atmospheric observations to circumvent mount model and tracking uncertainties. <sup>(6)</sup>

---

6. For recent examples see: G. Ashley; Tracking et al. Trials, Tech correspondence file nos. A/OP-346, A/TB-059.



Figures 8(a) and 8(b) relate source temperature and equivalent entrance aperture irradiance to line voltage, the measured parameter. Figures 9(a) and 9(b) relate detector signal to image displacement for representative detectors. Predictable, for small displacements, signal change is linearly related to subaperture image displacement and detectors are relatively insensitive to wander components normal to the line joining quadrature detector and subaperture image centroids. The voltages measured are functions of source intensity and wavelength as well as image displacements:

$$\Delta V = E(\lambda) [S_n(o) - S_n(\Delta r)];$$

where  $E(\lambda)$  is the effective in-band entrance aperture irradiance for filter  $\lambda$  while  $S_n(\Delta r)$  represents response in volts  $\cdot w^{-1} \cdot cm^2$  for the  $n$ th detector with the subaperture spot displaced,  $\Delta r$ , from its quiescent,  $(o)$ , position. Wavelength has two mechanisms for changing instrument response: (1) the spectral quantum efficiency,  $\eta_\lambda$ , of the detector; and (2) diffraction which changes the spot size. Figure 10 illustrates how spot size is predicted<sup>(7)</sup> to change with wavelength near focus.  $S_n(\Delta r)$  includes  $\eta_\lambda$  and the area common to spot and detector weighted by intensity contours of the former and sensitivity contours of the latter. Figure 11 shows how normalized signal should relate to image displacement for a uniform detector and a shortwave spot ( $\lambda$  to the left of the minimum in Figure 10). It is clear from Figure 11 and the calibration data (Figure 9(a)) that random spot motions about the quiescent position will produce a non-zero average signal history. The long period average value of the voltage history is, in principle, a measure of the average tilt of the wavefront and, of course, any quiescent misregistration of the image illumination centroids.

The calibration procedure produced a table of tilt responsivities,  $S(\Delta r)$ , for each detector/spectral option combination against, in effect, a standard irradiance source. To reduce observational data to tilt structure size, it was necessary only to determine the in-band aperture irradiance

---

7. See for example: E. Wolf, Proc. Roy. Soc. A, 204, p. 533 (1951).

8. For example: N. Carleton (editor), Methods of Experimental Physics, 12, Part A, p. 453 (1974).

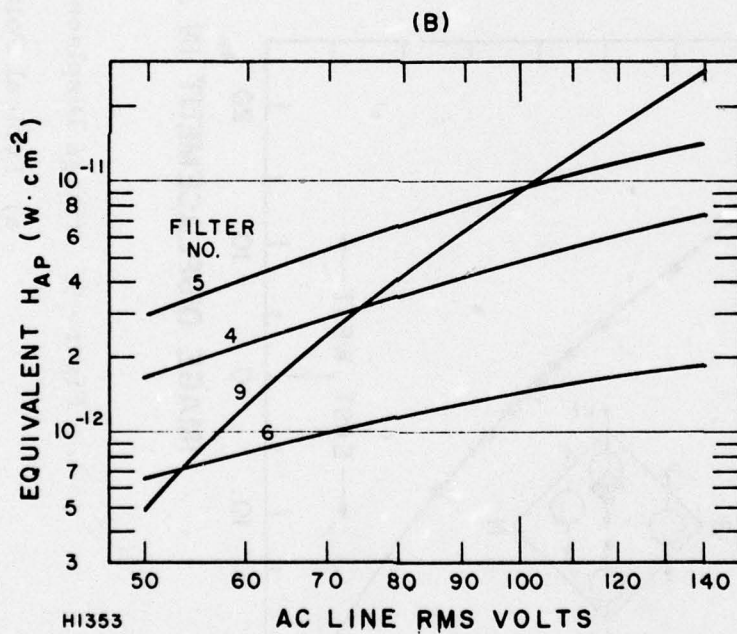
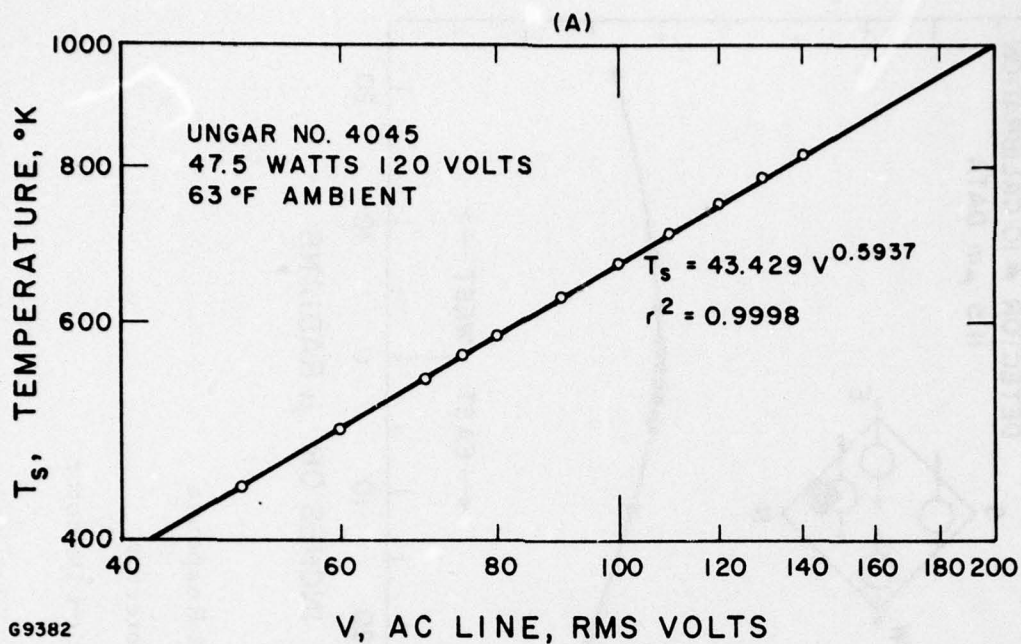


Figure 8 Point Source Calibration

a) Point Source Temperature

b) Exitance Equivalent  $H_{AP}$



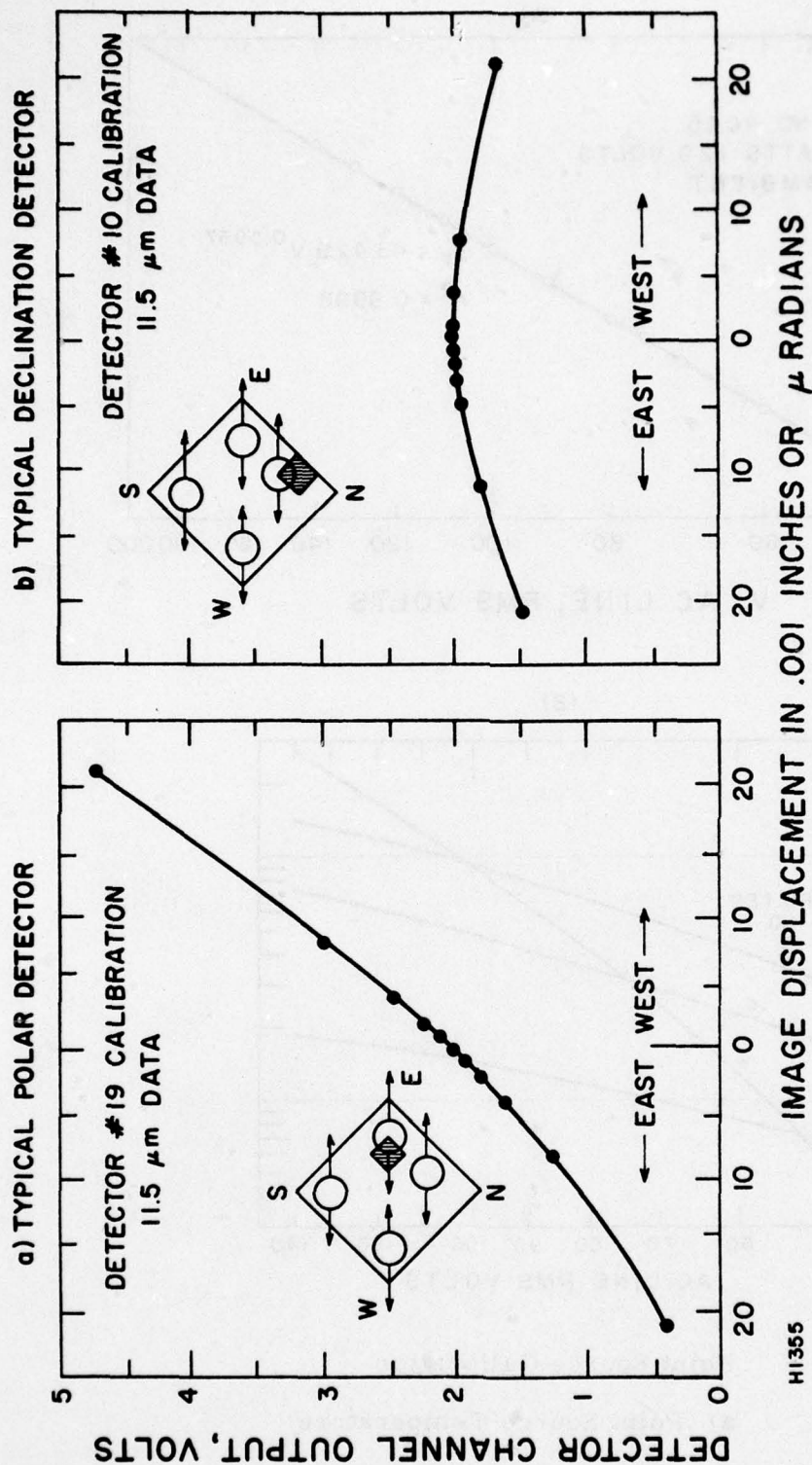


Figure 9 Image Displacement Response

a) Typical Polar Detector

b) Typical Declination Detector

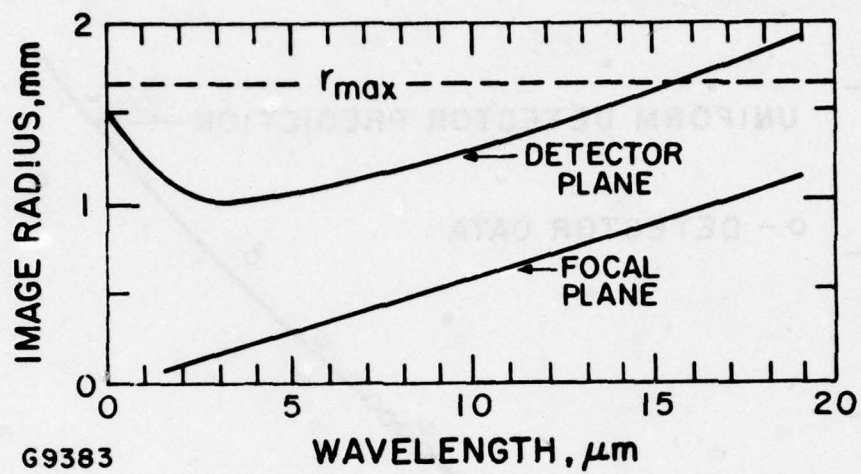


Figure 10 80% Encircled Energy



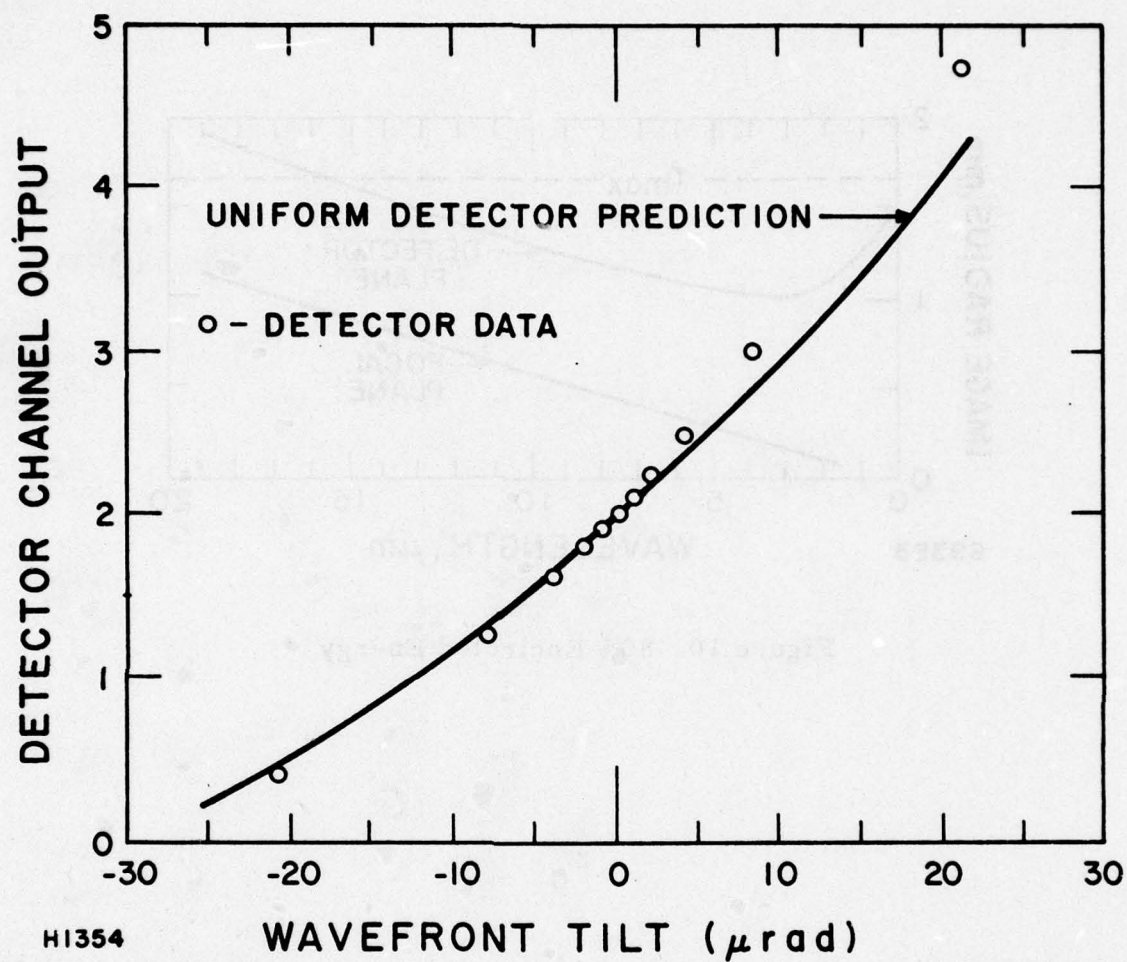


Figure 11 Predicted Displacement Response, 11  $\mu\text{m}$

produced by the one star  $\alpha$  Bootis, and the three planets observed. The former comes directly from astronomical surveys.<sup>(8)</sup> Computation of irradiance from solar system objects is a tedious but straightforward task with marked differences in approach for each planet. Mercury, for example, has no atmosphere and travels in a rather eccentric orbit. Its subsolar point has a grey body temperature of  $493^\circ\text{K}/\sqrt{R_{\text{A. U.}}}$  and an emissivity of 0.82;<sup>(9)</sup> where  $R_{\text{A. U.}}$  is its distance from the Sun, in astronomical units, at the time of the observation. Its dark side temperature is taken to be  $111^\circ\text{K}$  from the measurements of Murdock and Ney.<sup>(10)</sup> The illumination geometry can be calculated from American Ephemeris<sup>(11)</sup> tabulations. The subsolar point on Mercury was not visible during our observations and a limb cooling law<sup>(12)</sup>  $T(\phi) = T_{\text{ssp}} \cos^{1/6} \phi$  was used to calculate radiant intensity; where  $T(\phi)$  is the temperature of any area increment at a planet centered angular distance,  $\phi$ , from the subsolar point at temperature  $T_{\text{ssp}} = 493^\circ\text{K} f(\text{date})$ . The calculated signatures for Mercury during our observations is shown in Figure 12.

Venus, with its dense atmosphere, is essentially a uniform temperature disc and its long wave signature is a function of range only and not solar phase angle. Mars has a tenuous atmosphere and represents complicated intermediate case wherein both the surface and atmosphere contribute to the signature. Fortunately, owing to its solar distance, Mars can appear only slightly gibbous from Earth and the planet is, moreover, a very popular subject for infrared observations. Thus, its illumination geometry does not alter its observed signature greatly and many measurements of its irradiance are available in the literature.

- 
9. O. L. Hansen, Ap. J. 190, p. 715 (June 1974).
  10. T. L. Murdock, E. P. Ney: Science, 170, p. 535 (October 1970).
  11. USN Obs. The American Ephemeris and Nautical Almanac for 1976, U. S. G. P. O. (1976).
  12. Mercury is similar to our moon; see Saari and Shorthill in: AAS Sci. and Technology Series, 13, p. 57 (1967).



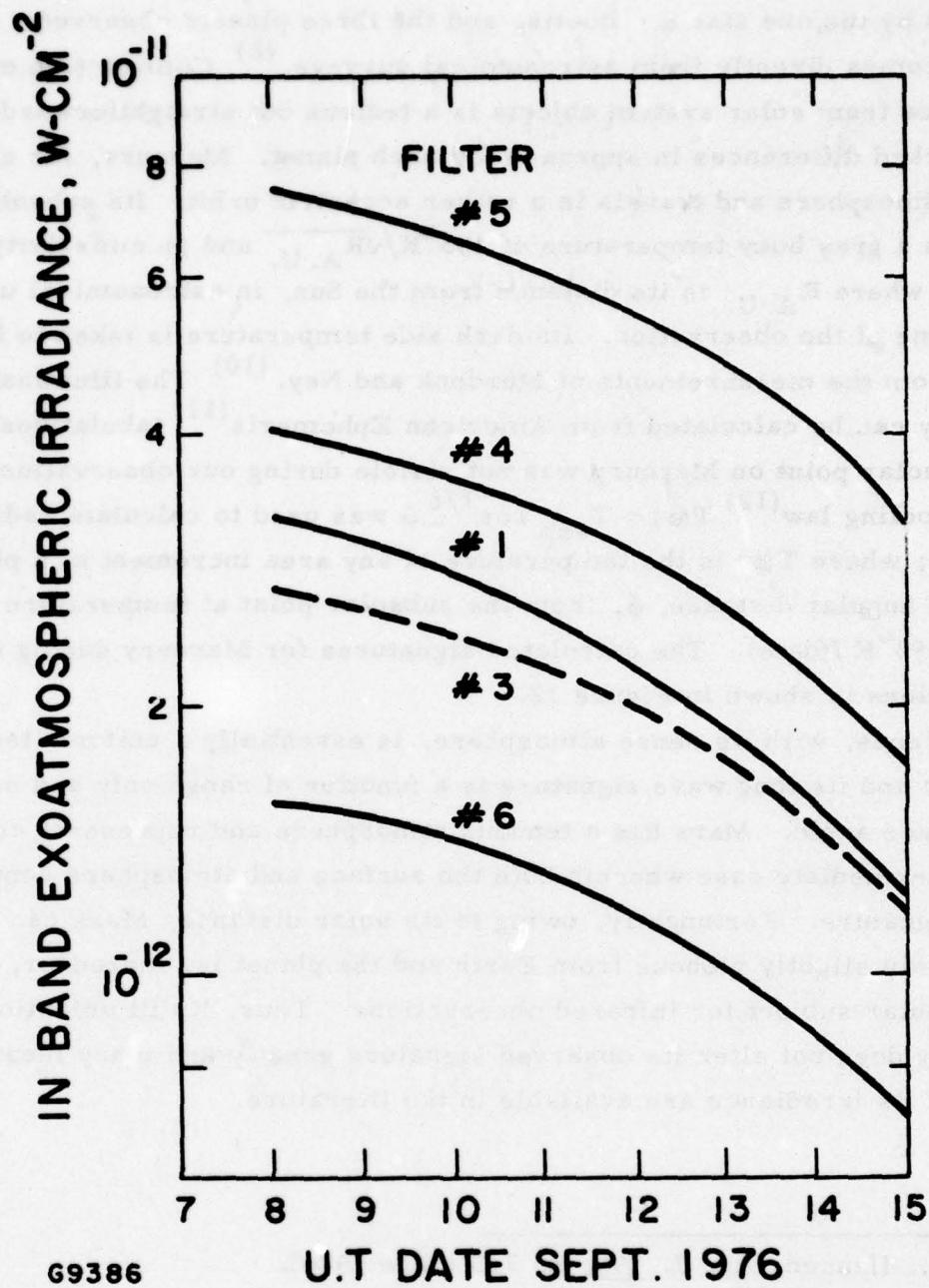


Figure 12 Mercury Waning

The LOWTRAN<sup>(13)</sup> Program was used to calculate atmospheric transmission and to trim effective center wavelength and bandpass for AMTA spectral options. Passband,  $\Delta\lambda$ , and center wavelength,  $\lambda_{\text{eff}}$ , are given by

$$\Delta\lambda = \frac{1}{R_{\text{max}}(\lambda)} \int_{R=0.005 \text{ points}}^{\overbrace{R(\lambda)}} S(\lambda) W(\lambda, T) \tau_a(\lambda) d\lambda \quad (1)$$

and

$$\lambda_{\text{eff}} = \frac{1}{\Delta\lambda} \int \lambda R(\lambda) d\lambda \quad (2)$$

respectively, where  $S(\lambda)$  is the throughput and response of optical/sensor components combined and given by manufacturer's measurements;  $\tau_a(\lambda)$  is atmospheric transmission given by LOWTRAN 3; and,  $W(\lambda, T)$  is the Planck radiance function for source temperature  $T^\circ\text{K}$ . While source temperature generally does not impact AMTA spectral parameters strongly, in this instant it did: Filter #9 has a passband  $1.1 \mu\text{m}$  wide centered at  $3.8 \mu\text{m}$  for the planet Mercury and shifts to  $\Delta\lambda = 0.6 \mu\text{m}$  centered  $\lambda_{\text{eff}} = 1.6 \mu\text{m}$  when  $\alpha \cdot \text{Bootis}$  ( $4900^\circ\text{K}$ ) is observed.

A set of sixteen detector angular responsivity functions,  ${}^n\langle R \rangle_f$ , was derived from the calibration data for each of the five spectral options.

$${}^n\langle R \rangle_f = \frac{E_{\text{ap}}(\lambda) F \text{ mS}}{r(\lambda) \Delta F} \frac{\delta a}{\delta v} \text{ microradian} \cdot \text{watt} \cdot \text{cm}^{-2} \cdot \text{volt}^{-1} \quad (3)$$

Sixteen detectors encompass the four subaperture images.  ${}^n\langle R \rangle_f$  is angular responsivity for the  $n^{\text{th}}$  detector and  $f^{\text{th}}$  filter option.  $r(\lambda)$  is the image radius;  $F$  is the telescope focal length ( $960.1$  inches, for this experiment);

13. See for example: J. E. A. Selby and R. A. McClatchey, Atmospheric Transmittance from 0.25 to 28.5  $\mu\text{m}$  LOWTRAN-3, AFCRL-TR-75-0255 (May 1975).



m is magnification of the reimaging optic, while S and  $\Delta F$  are scaling distances shown in Figure 13.  $E_{ap}(\lambda)$  is the entrance aperture equivalent inband irradiance from the test source. To scale the cross correlation between  $i^{th}$  and  $j^{th}$  detectors during planet Mercury observations, for example, the convolved voltage histories are multiplied by  $i\langle R \rangle_f^k \langle R \rangle_f / E_{ap}^2(\lambda, \phi)$  to yield squared microradians of tilt.

Scales for the scintillation or 'twinkle' autocorrelation functions were established by squaring the sum of peak voltages put out by four detectors, comprising a quadrature set, with the reference source on-axis. The sum signal is relatively insensitive to image position. This is illustrated in Figure 14 which presents calibration data. The lower (staircase) trace results from changing common area between the illuminated sub-aperture projection and the detector pair shown, as the point image source is translated. The upper trace records the output of all four detectors at the same time. Signal changes at extreme excursions are due to convolution of spot intensity and differing detector sensitivity contours. The extreme excursion moves all spots through approximately half their individual radii. The data shown is for spectral option #9 P which is centered at  $3.6 \mu m$ .

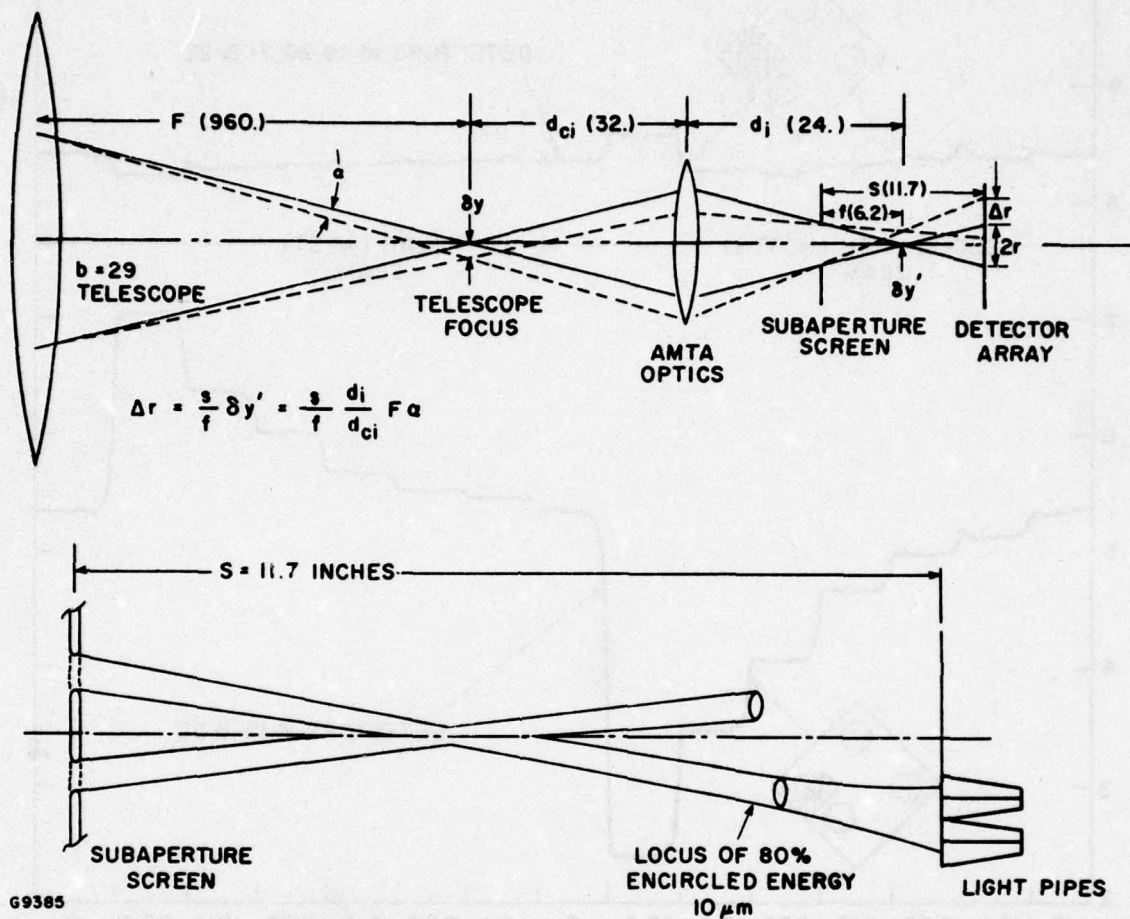


Figure 13 Angular Scaling Layout



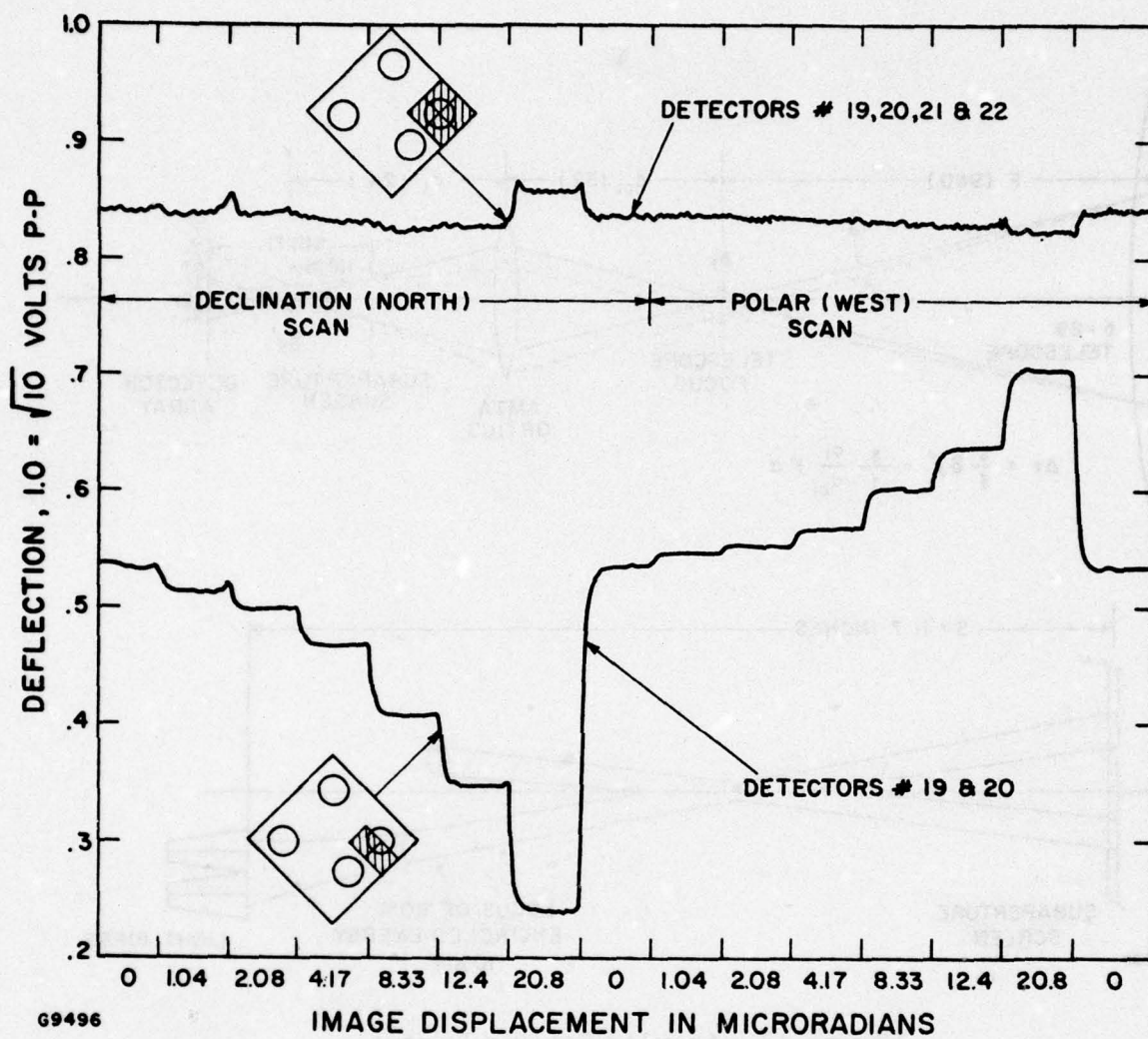


Figure 14 Displacement Calibration

### 3.0 DATA DISCUSSION

The atmospheric and calibration data obtained between 8 and 16 September 1976 was returned to the Everett Laboratory for analysis. Monitoring equipment used during observations gave some indication the signals recorded in the 1.7, 10.5 and 11.5 micron bands were correlated between certain detectors.<sup>(14)</sup> The existence of correlation was estimated in a rather crude way: The voltage of four detectors, monitoring different subapertures, were written out simultaneously with a multipen chart record. The traces appear to track more frequently when a target is in the field than when we 'stepped-off' to look at background (see Figure 15); thus it wasn't a totally blind experiment. At Everett the signals from pairs of detectors were band limited and correlated with results shown in accompanying illustrations.

Figure 16 is a plot of the cross correlation function:

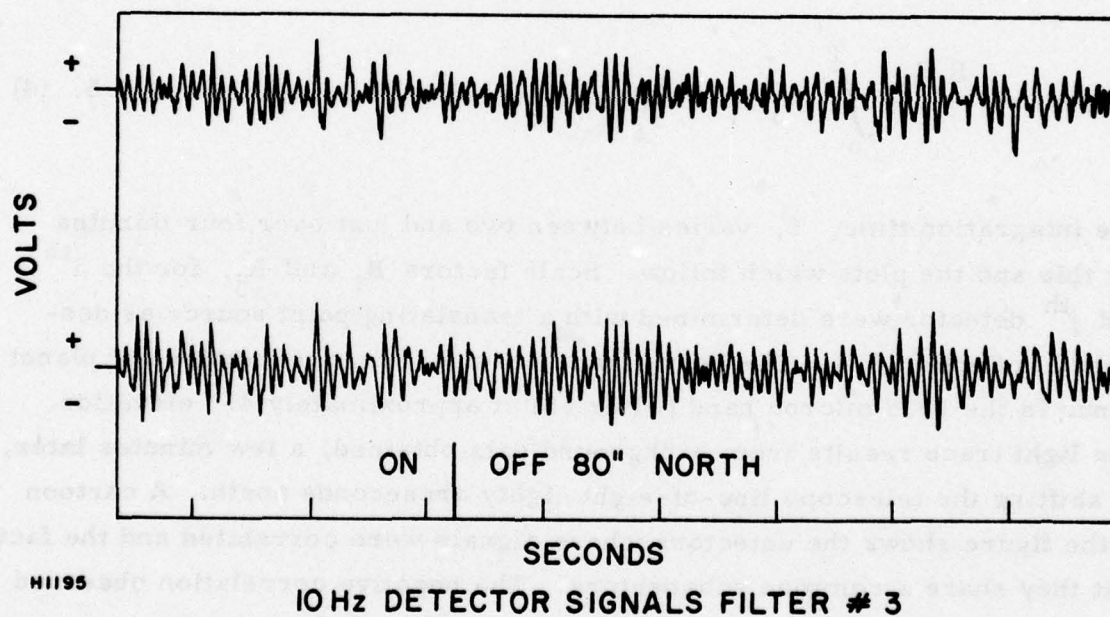
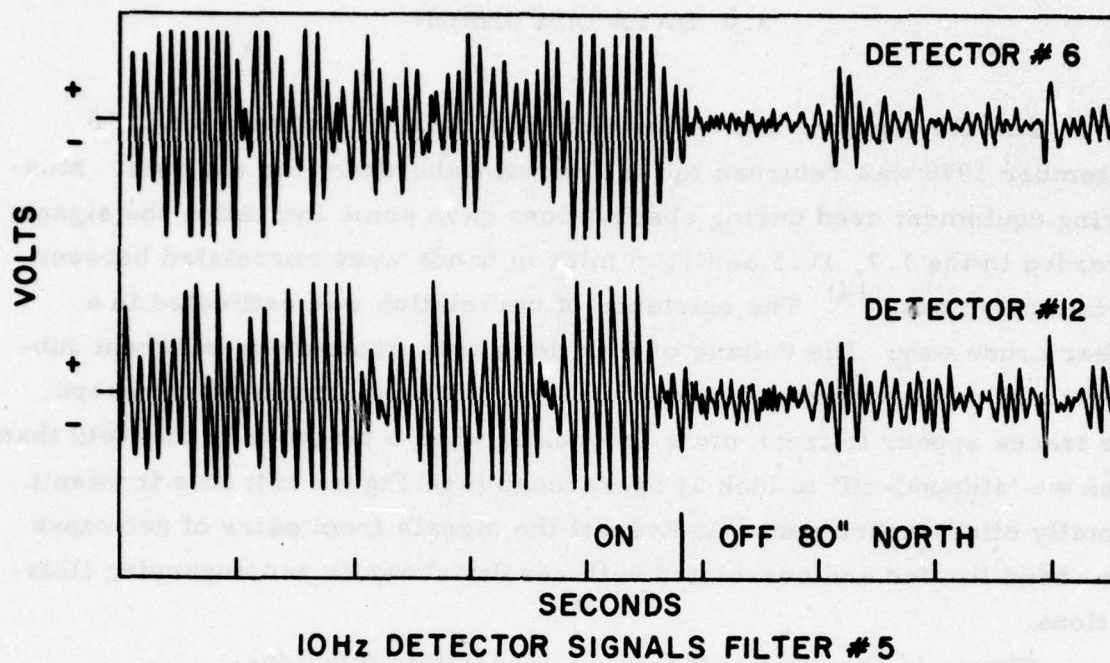
$$r(\tau) = \frac{R_i R_j}{T} \int_0^T V_i(t) \cdot V_j(t - \tau) dt, \text{ where } -0.5 \text{ sec} \leq \tau \leq 0.5. \quad (4)$$

The integration time,  $T$ , varies between two and just over four minutes for this and the plots which follow. Scale factors  $R_i$  and  $R_j$ , for the  $i^{\text{th}}$  and  $j^{\text{th}}$  detector were determined with a translating point source as described in Section 2.0. The heavy trace results from observations of planet Venus in the 10.5 micron band (filter #5) at approximately  $47^\circ$  elevation. The light trace results from background data obtained, a few minutes later, by shifting the telescope line-of-sight eighty arcseconds north. A cartoon in the figure shows the detectors whose signals were correlated and the fact that they share a common subaperture. The negative correlation observed near  $\tau = 0$  must be due to east-west motion of the light spot; that is to say, the polar component of angle-of-arrival change. The peak variance of the tilt amounts to approximately  $3.2 \mu\text{radians}^2$ . This measurement was obtained

---

(14) R&D Status Report, 27 October 1976, Contract F30602-75-C-0235.





H1195

Figure 15 Raw Data

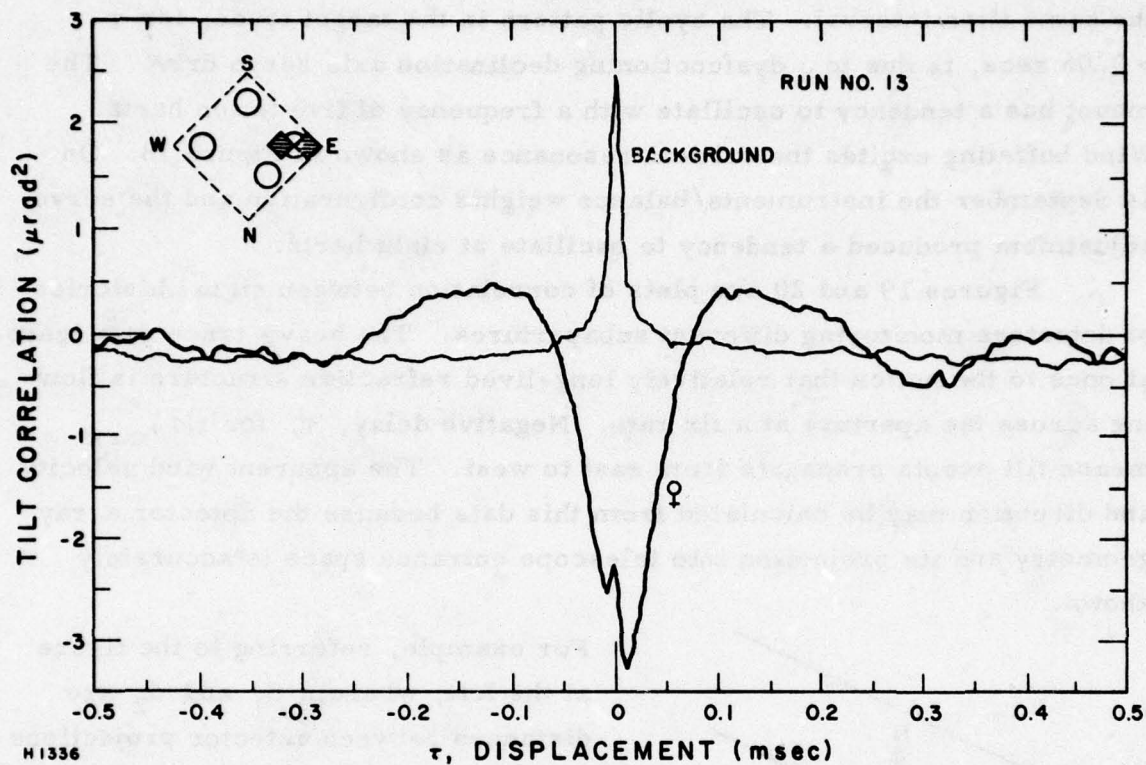
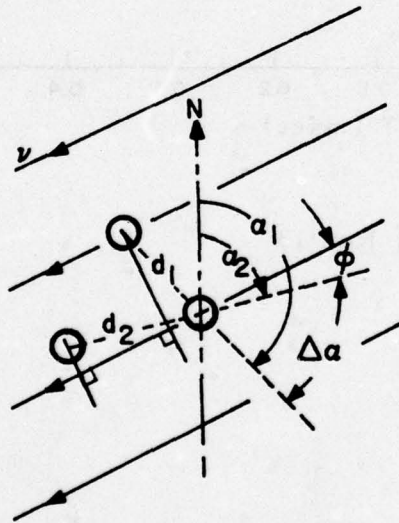


Figure 16 Filter #5 Data, Run 13



with an eight-inch (sub)aperture. We attribute the background trace to microphonic noise (refrigerator thumping) and large scale radiant atmospheric structure. The notch in the heavy trace, at  $\tau = 0$  is probably also microphonic and perhaps intensity scintillation which will be discussed presently. Figure 17 shows what the orthogonal detectors observed during the same time interval. The cyclic pattern in the target trace, for  $\tau > 0.06$  secs, is due to a dysfunctioning declination axis servo drive. The mount has a tendency to oscillate with a frequency of five to ten hertz. Wind buffeting excites the critical resonance as shown in Figure 18. On 14 September the instruments/balance weights configuration and the servo adjustment produced a tendency to oscillate at eight hertz.

Figures 19 and 20 are plots of correlation between signal histories of detectors monitoring different subapertures. The heavy-trace data leads at once to the notion that relatively long-lived refractive structure is flowing across the aperture at a fix rate. Negative delay,  $\tau$ , for  $r(\tau)_{\max}$  means tilt events propagate from east to west. The apparent wind velocity and direction may be calculated from this data because the detector array geometry and its projection into telescope entrance space is accurately known.



For example, referring to the figure at the left, wherein  $d_1$  and  $d_2$  are distances between detector projections and  $\vec{v}$  is the wind vector, it is clear by inspection that:

$$\frac{d_1 \cos \phi}{\Delta t_1} = v = \frac{d_2 \cos (\Delta \alpha + \phi)}{\Delta t_2}$$

from which it follows that:

$$\phi = \arctan \left[ \frac{1}{\sin \Delta \alpha} \left( \cos \Delta \alpha - \frac{\Delta t_2 d_1}{\Delta t_1 d_2} \right) \right]$$

The Table 2 shows wind speed and direction calculated from 11.5 micron data obtained 9 September.

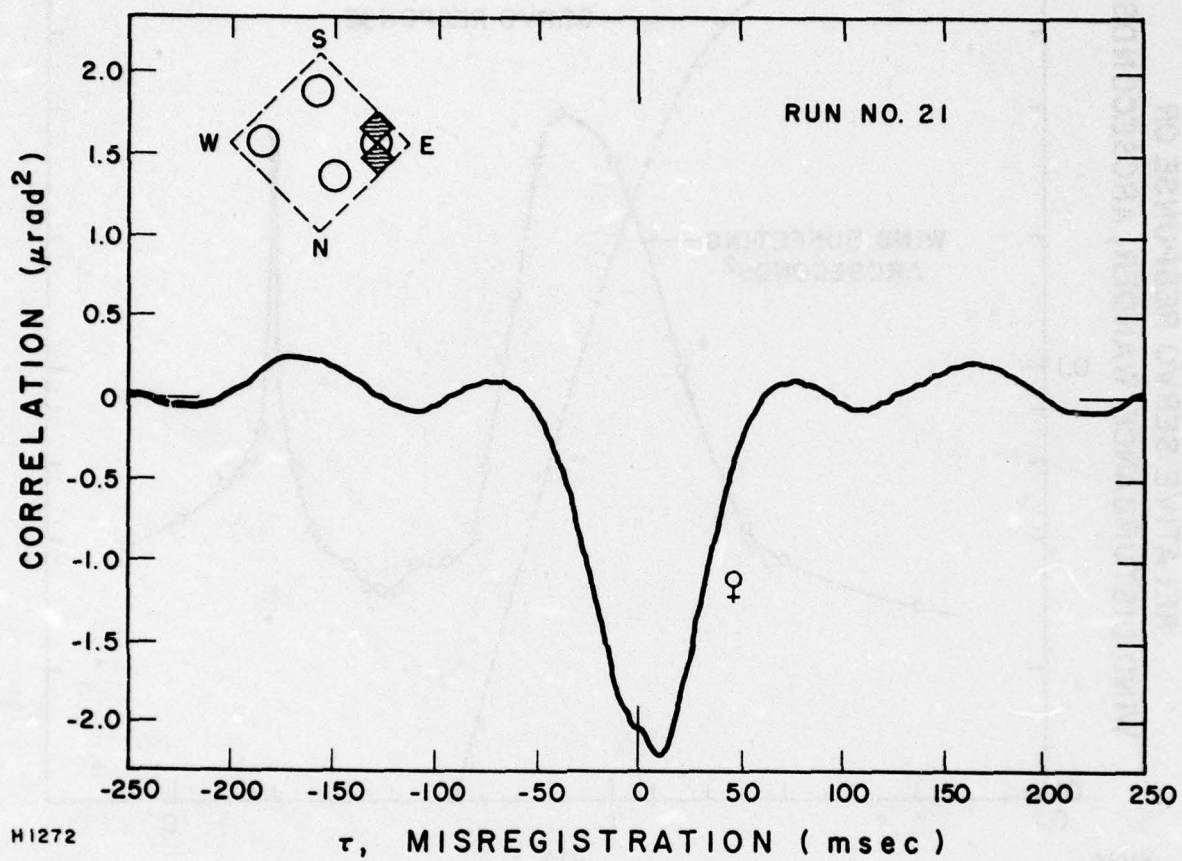


Figure 17 Filter #5 Data, Run 21



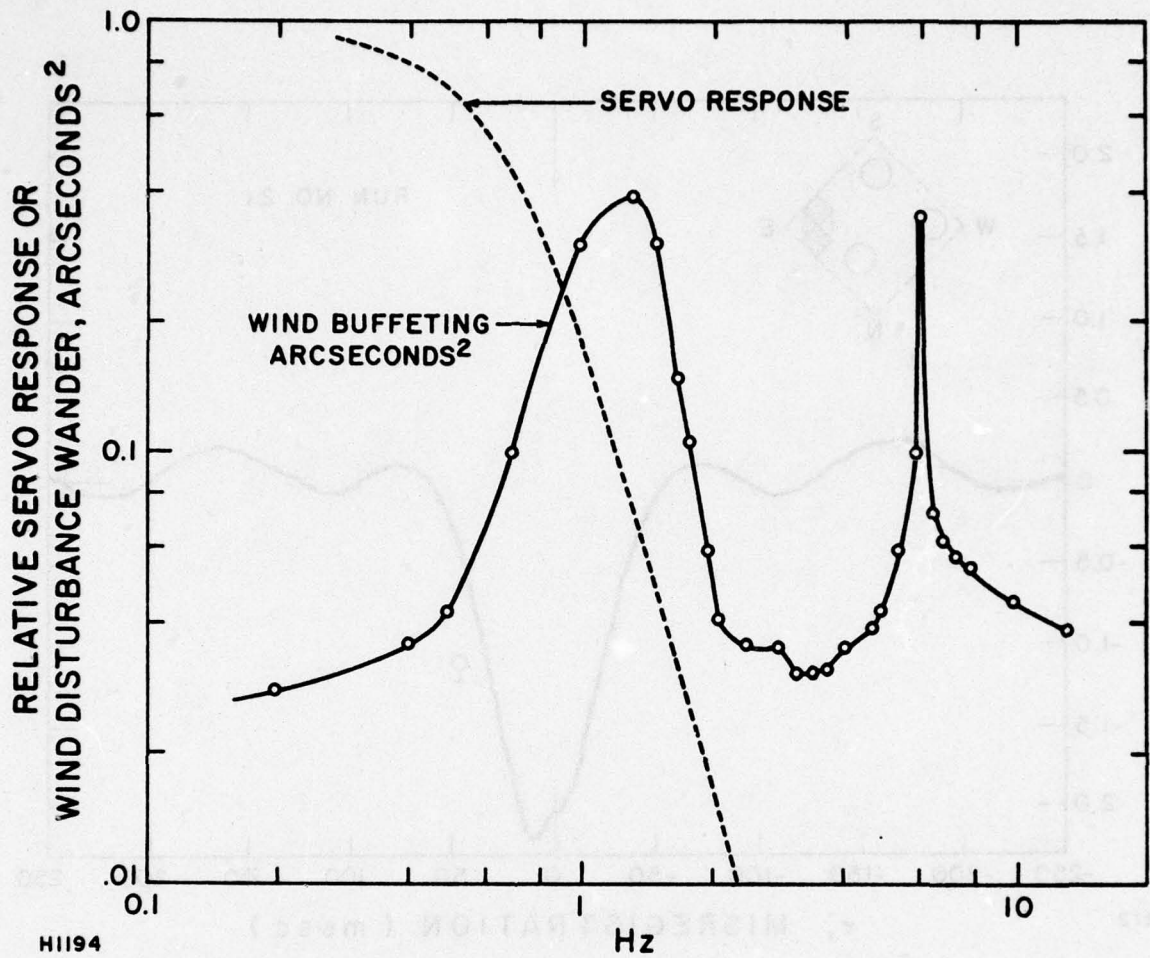


Figure 18 48-Inch Mount Declination Response

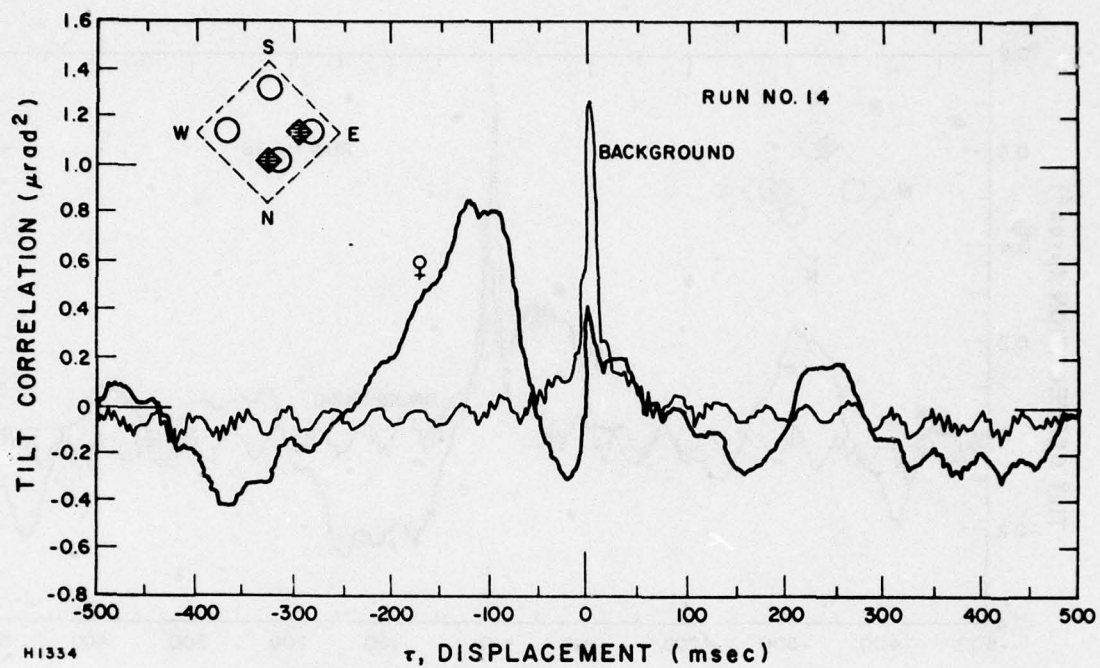


Figure 19 Filter #5 Data, Run 14



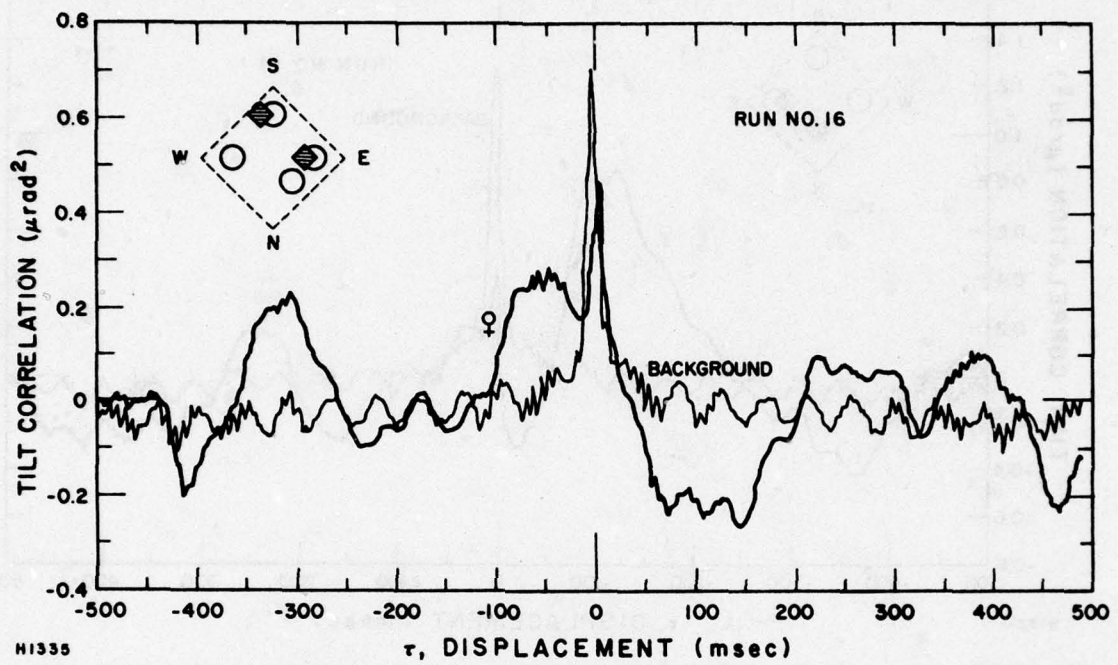


Figure 20 Filter #5 Data, Run 16

TABLE 2. FILTER #4, 11.5  $\mu$ m, 9 SEPTEMBER 1976

<u>Data Run #</u>	<u>Detectors</u>	<u>Velocity</u>	<u>Wind</u> <u>Direction</u>
92	21 x 6	8.1 m/sec	
90	21 x 5	6.86	
89	21 x 7	6.34	} 116.19°
88	21 x 25	6.34	
87	21 x 17	6.69	
86	11 x 17	(5.44)	
84	21 x 24	7.21	} 116.05°
83	21 x 9	(9.50)	
82	21 x 11	7.05	
35	21 x 24	7.21	} 116.01°
34	21 x 5	6.59	
31	19 x 16	7.53	
Average (10 pts.)		6.99 $\pm$ 0.17 meters/second	

Calculated angles and velocities are the result of four minute observations. The experimenter's notes indicate local winds were '15 mph from the south-east' at this time. As expected, the air eddies producing the refractive disturbances are evidently close to the telescope. NOAA balloon survey records, taken 1-1/2 hours later above Hilo (Hawaii) 100 miles southeast, show transition between surface trade winds (general northeasterlies) and the jet stream from the west is already well developed at 5 km altitude. AMOS Observatory is at 3.05 km altitude. NOAA data from Lihue (Kauai) 250 miles northwest, indicates the transition occurs at 6.7 km.

The 11.5 micron data was obtained by observing the planet Mercury at approximately sixty degrees elevation and 22:30 hours, 9 September U. T.

Figures 21, 22, 23, 24, 25 and 26 show correlation computed for the detector pairs illustrated in each figure. We can see wind refractive structure propagating across the line-of-sight and the following features are evident:



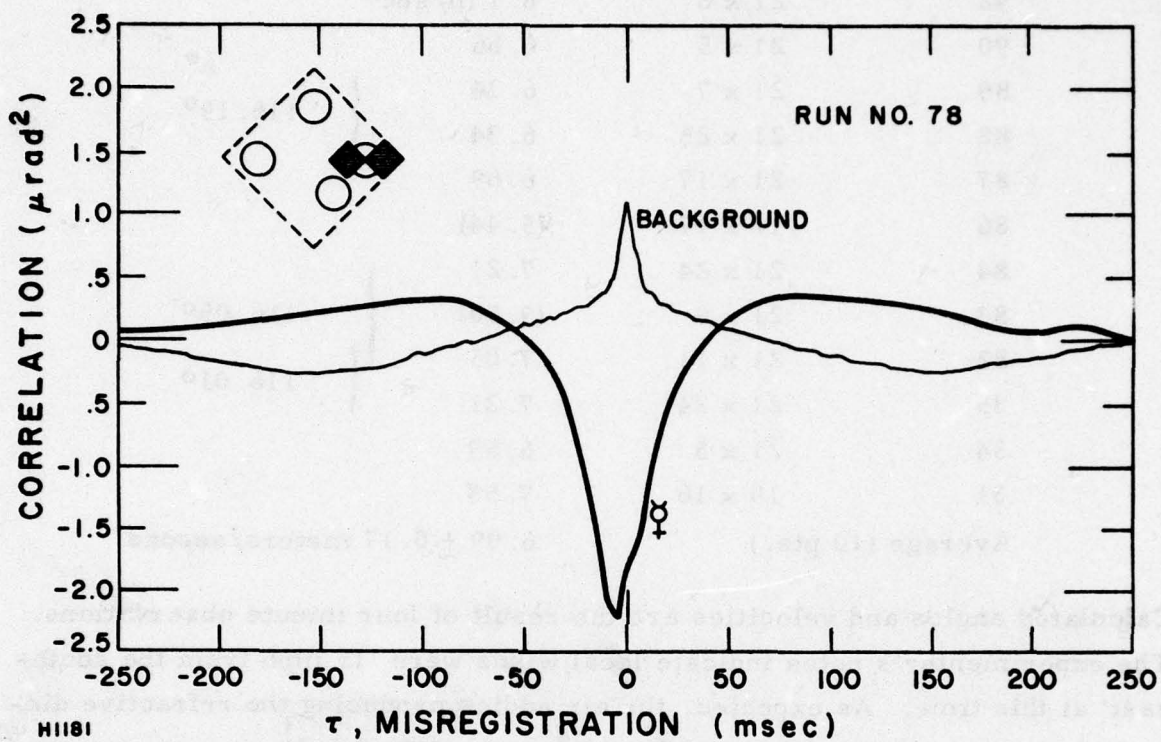


Figure 21 Filter #4 Data, Run 78

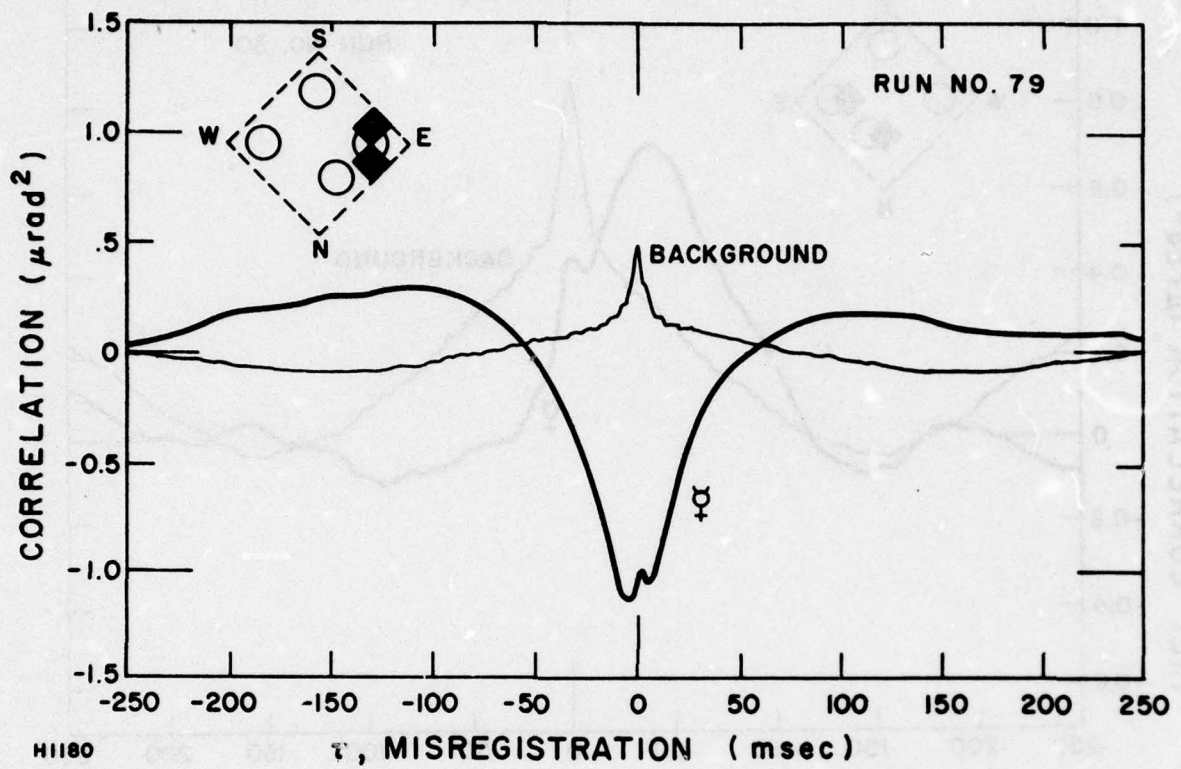
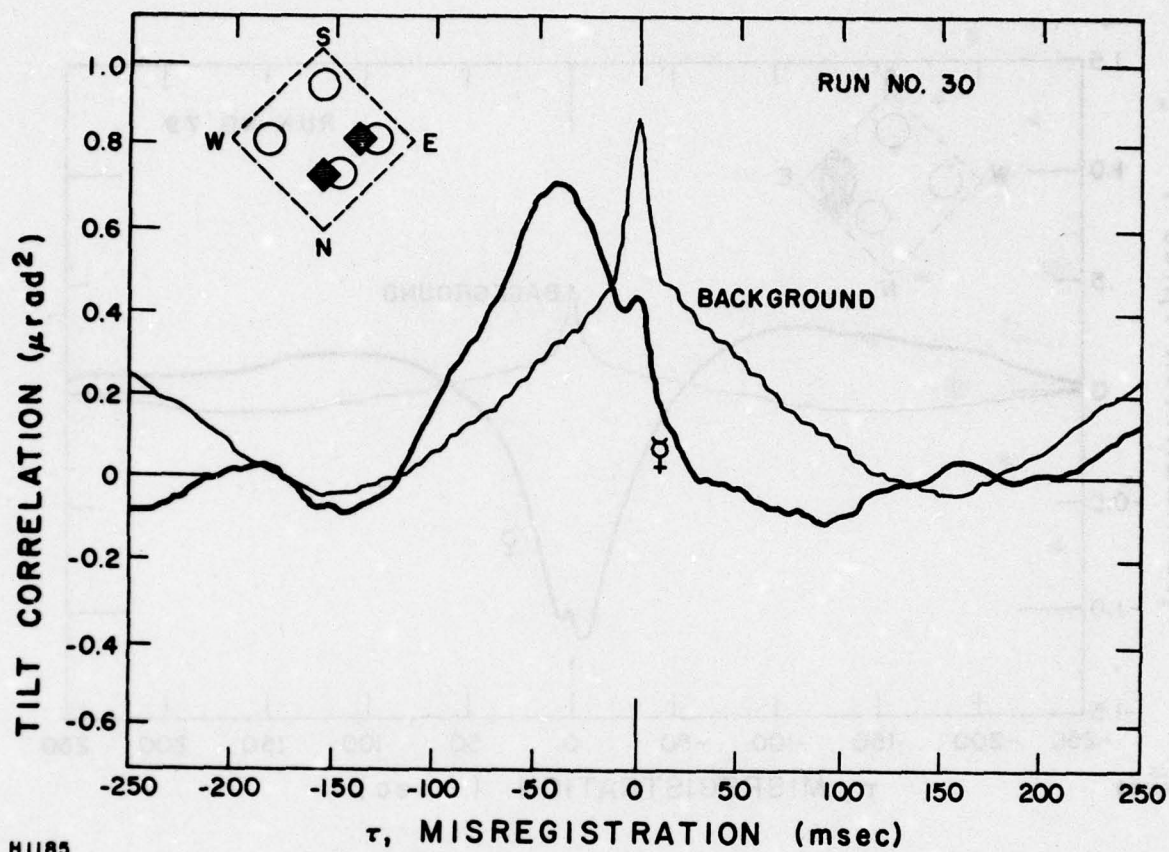


Figure 22 Filter #4 Data, Run 79





H1185

Figure 23 Filter #4 Data, Run 30

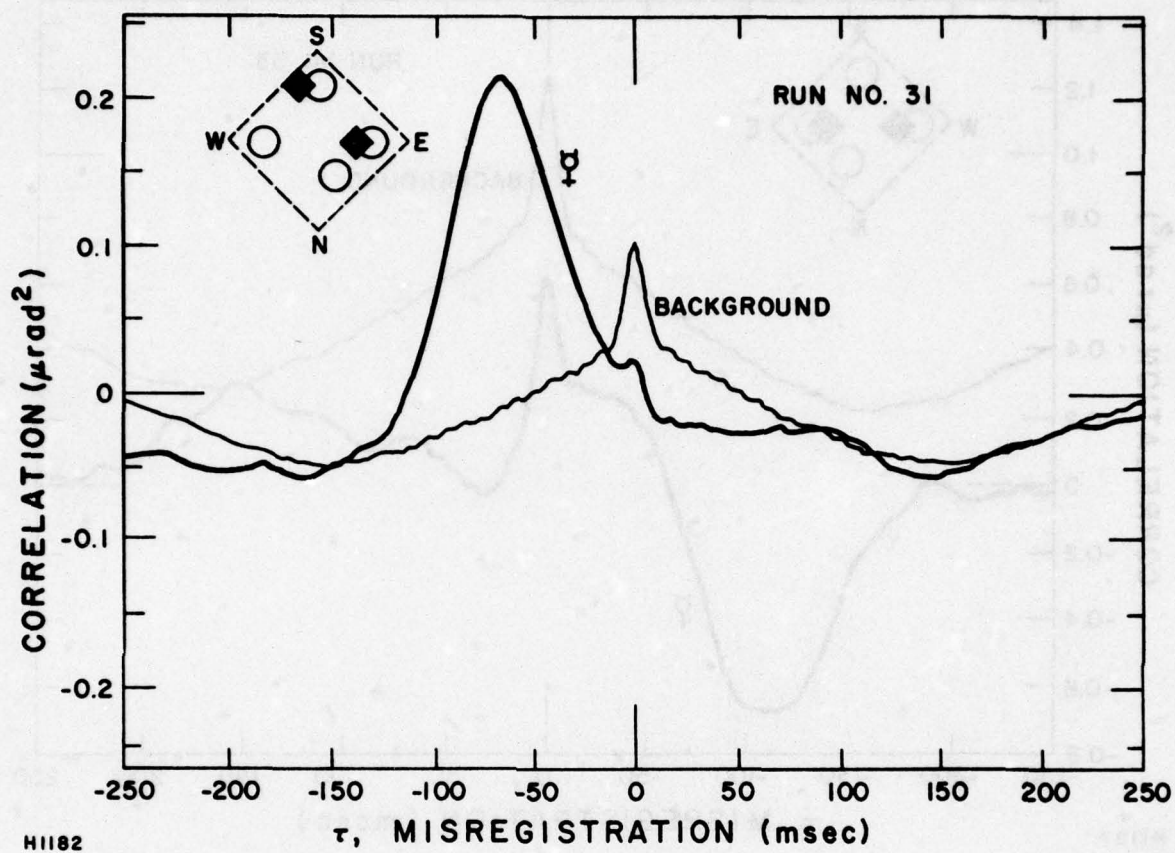
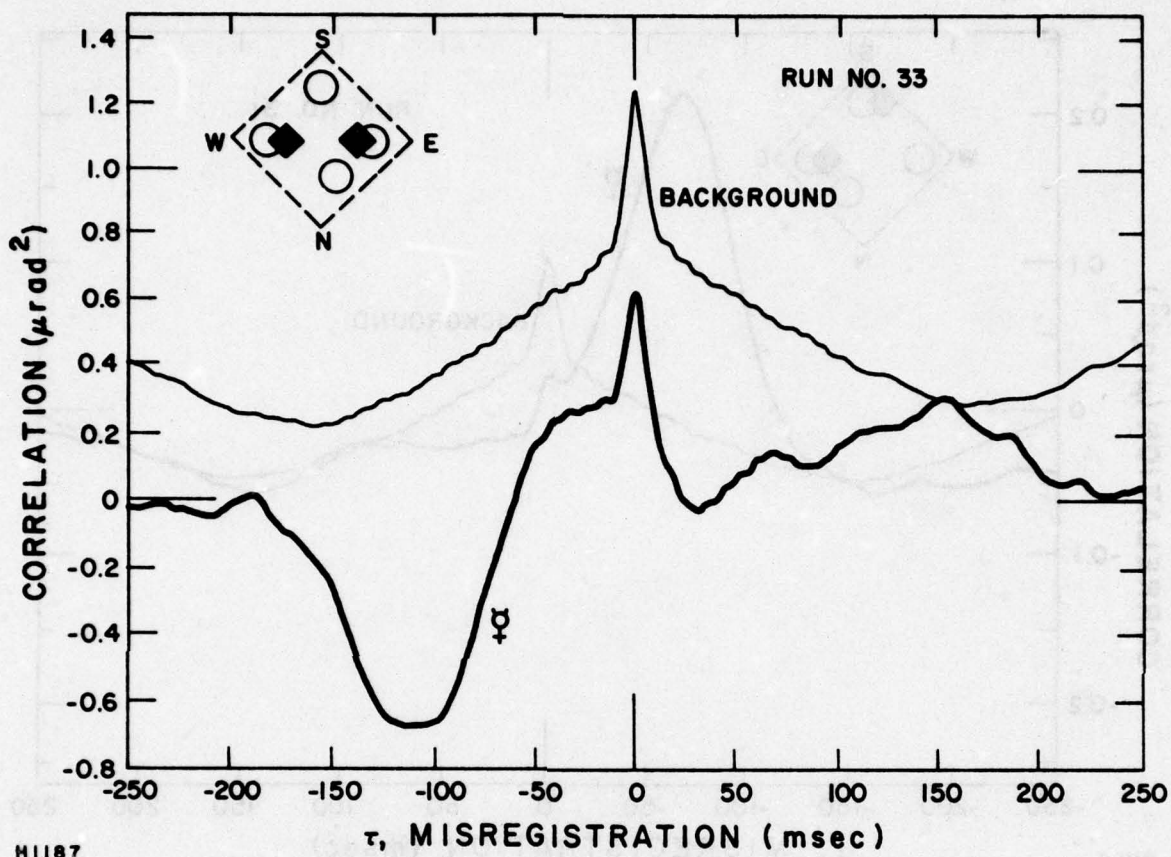


Figure 24 Filter #4 Data, Run 31



H1187

Figure 25 Filter #4 Data, Run 33



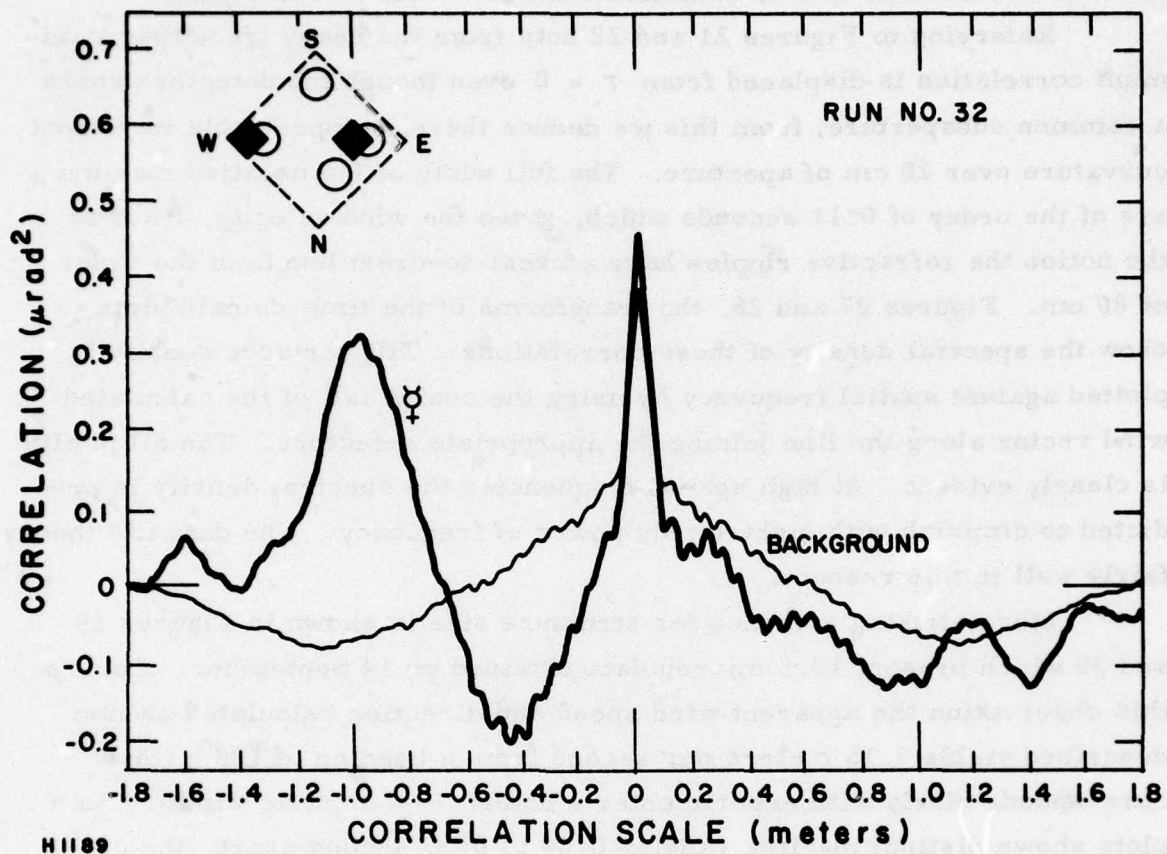


Figure 26 Filter #4 Data, Run 32

- a) Structure is of the order of half the size of the telescope.
- b) The refraction features may be highly elliptical, perhaps even striated like water waves.

We have insufficient data to establish whether or not this is typical.

Referring to Figures 21 and 22 note from the heavy trace that maximum correlation is displaced from  $\tau = 0$  even though the detectors share a common subaperture; from this we deduce there is appreciable wavefront curvature over 20 cm of aperture. The full width of the negative maxima are of the order of 0.11 seconds which, given the wind velocity, leads to the notion the refractive ripples have a crest-to-crest length of the order of 80 cm. Figures 27 and 28, the transforms of the time-domain plots, show the spectral density of these correlations. Tilt variance density is plotted against spatial frequency by using the cosine fall of the calculated wind vector along the line joining the appropriate detectors. The ellipticity is clearly evident. At high spatial frequencies the spectral density is predicted to diminish with eight-thirds power of frequency. The data fits theory fairly well in this respect.

More striking evidence for structure size is shown in Figures 29 and 30 which present 10.5 micron data obtained on 14 September. During this observation the apparent wind speed and direction calculated as just described yields 3.16 meters per second from a heading of  $128^\circ$ ; (this corresponds nicely with experimenter's notes: '5-7 mph SE wind'). Both plots shown distinct maxima ranging 0.09 to 0.35 second apart: the corresponding crest-to-crest distance appears to be 0.28 to 1.1 meters. Each plot is the result of averaging 131 contiguous one second cross-correlations.

A qualitative verification of the  $128^\circ$  wind heading is at once evident in Figures 31 and 32 wherein the traces are the result of averaging 500 half-second correlations of Venus data obtained with the detectors shown. Wind direction is given in each figure and the sign of maximum correlation is readily predicted; the wind quarter can also be deduced from Figure 31 because  $r(\tau)_{\max}$  occurs at  $\tau < 0$ . Negative  $\tau$  means the signal history of the corner detector must be delayed to produce a match.

The reproducibility of these results may be judged from Figure 33 which illustrates two data runs separated by  $7^m40^s$ . Each trace is the

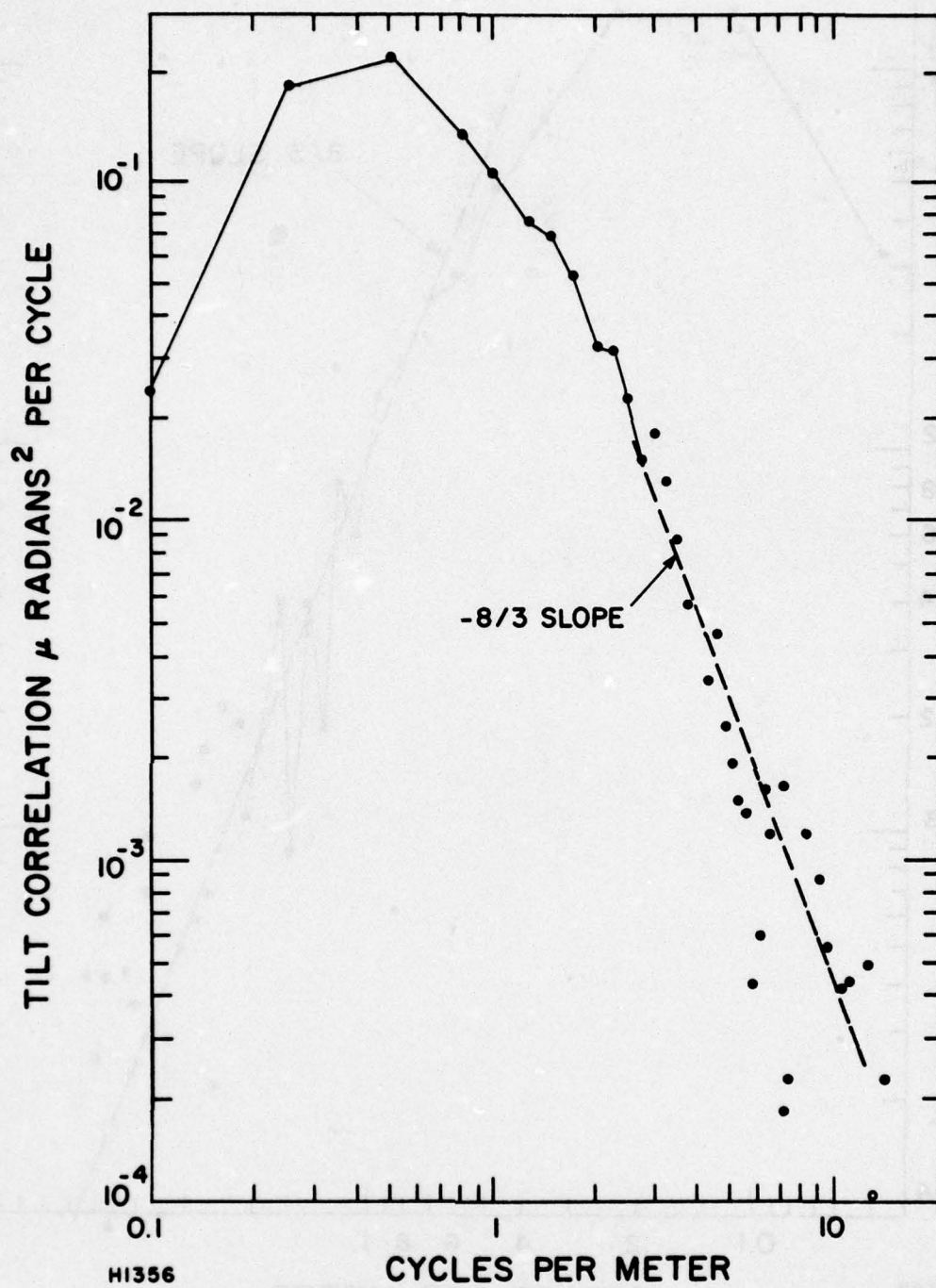


Figure 27 Refractive Structure PSD



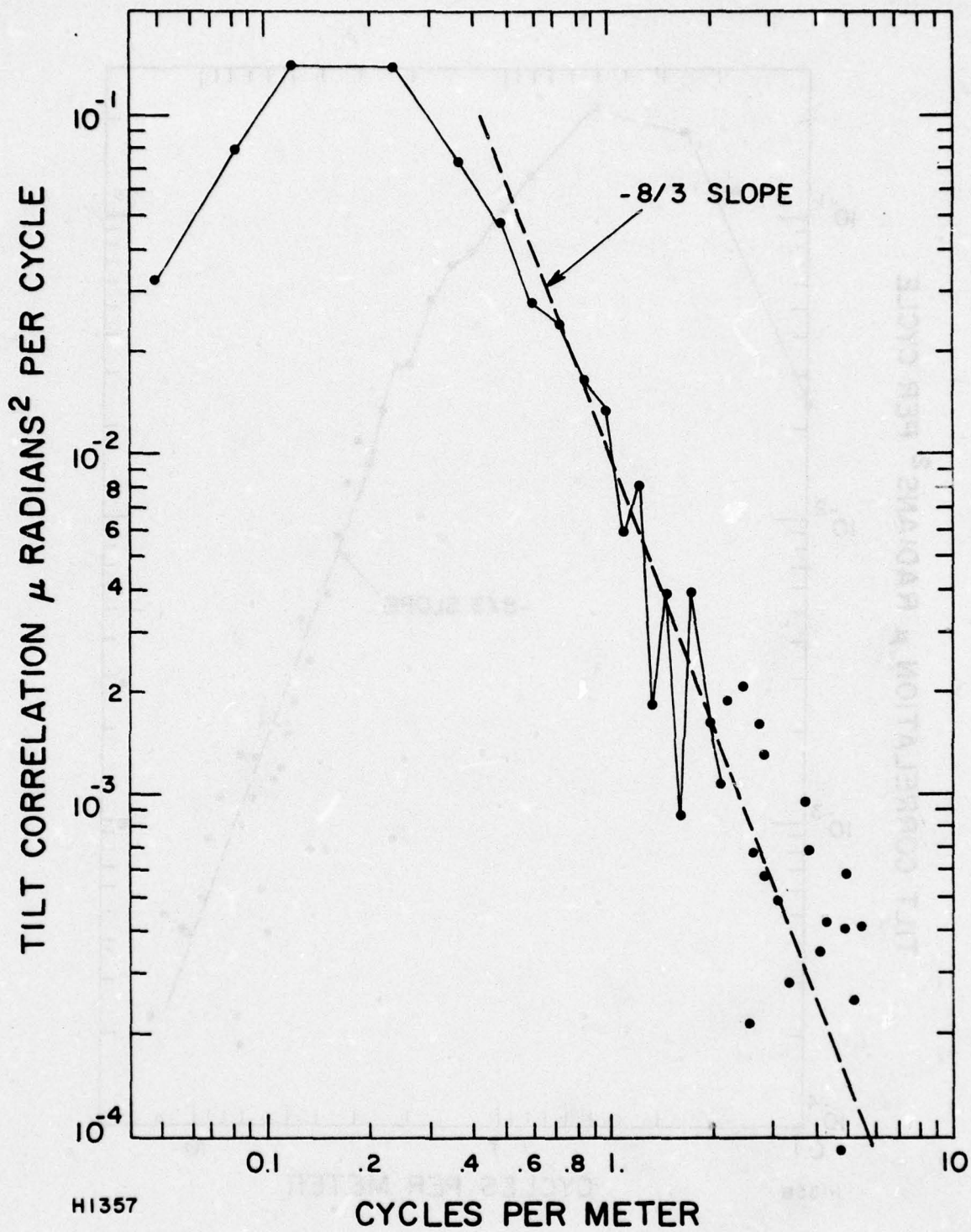


Figure 28 Refractive Structure PSD

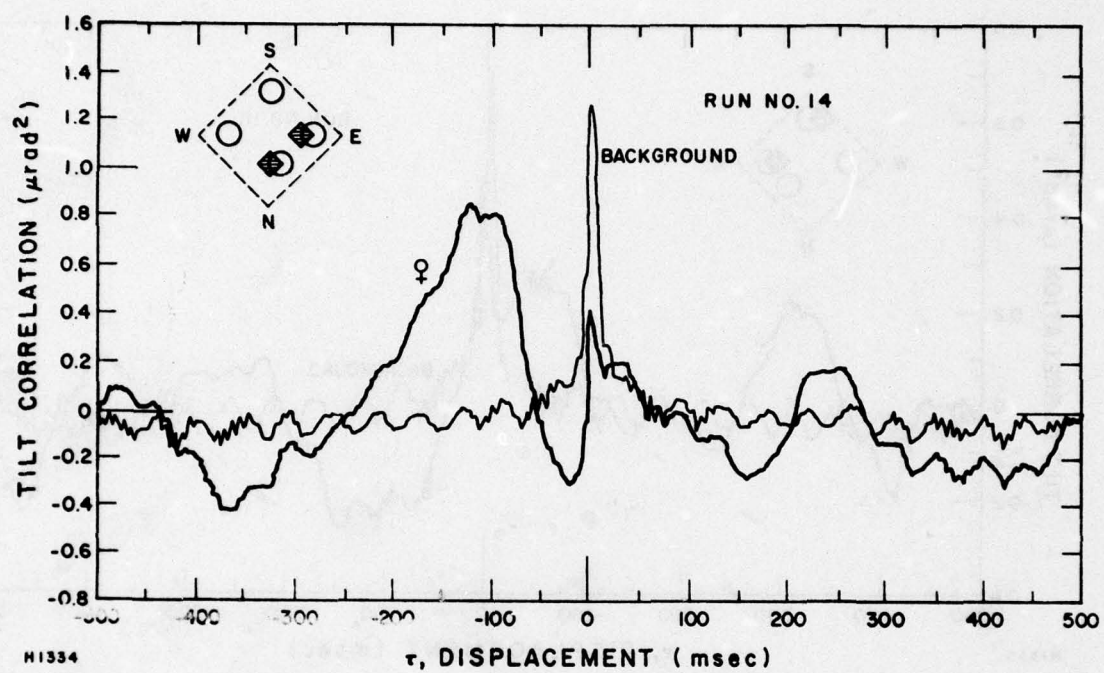


Figure 29 Filter #5 Data, Run 14

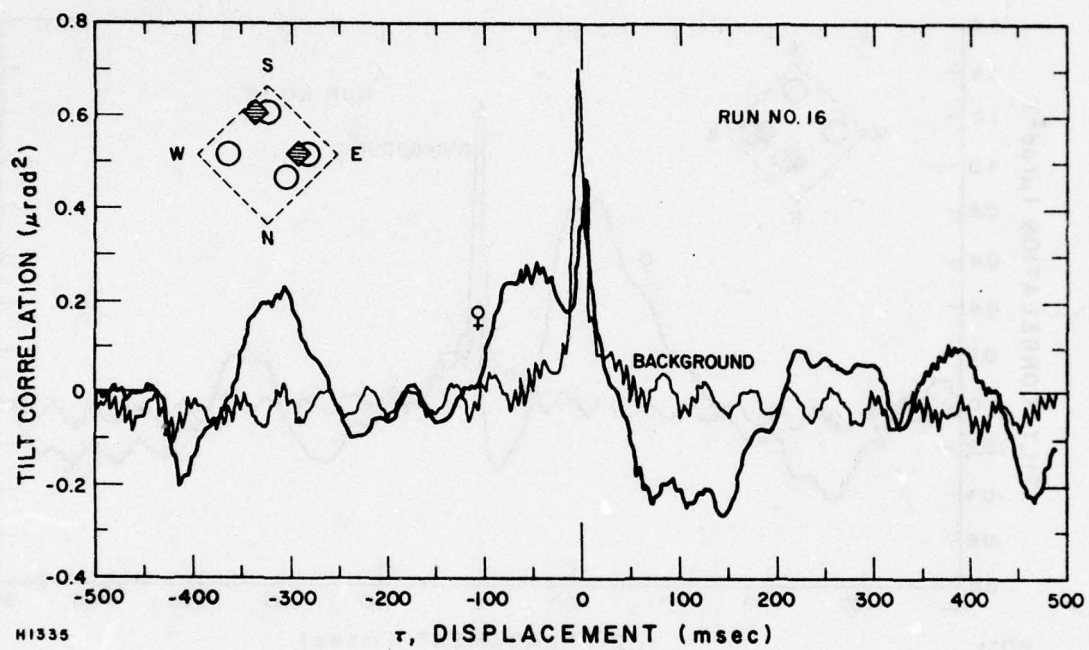


Figure 30 Filter #5 Data, Run 16



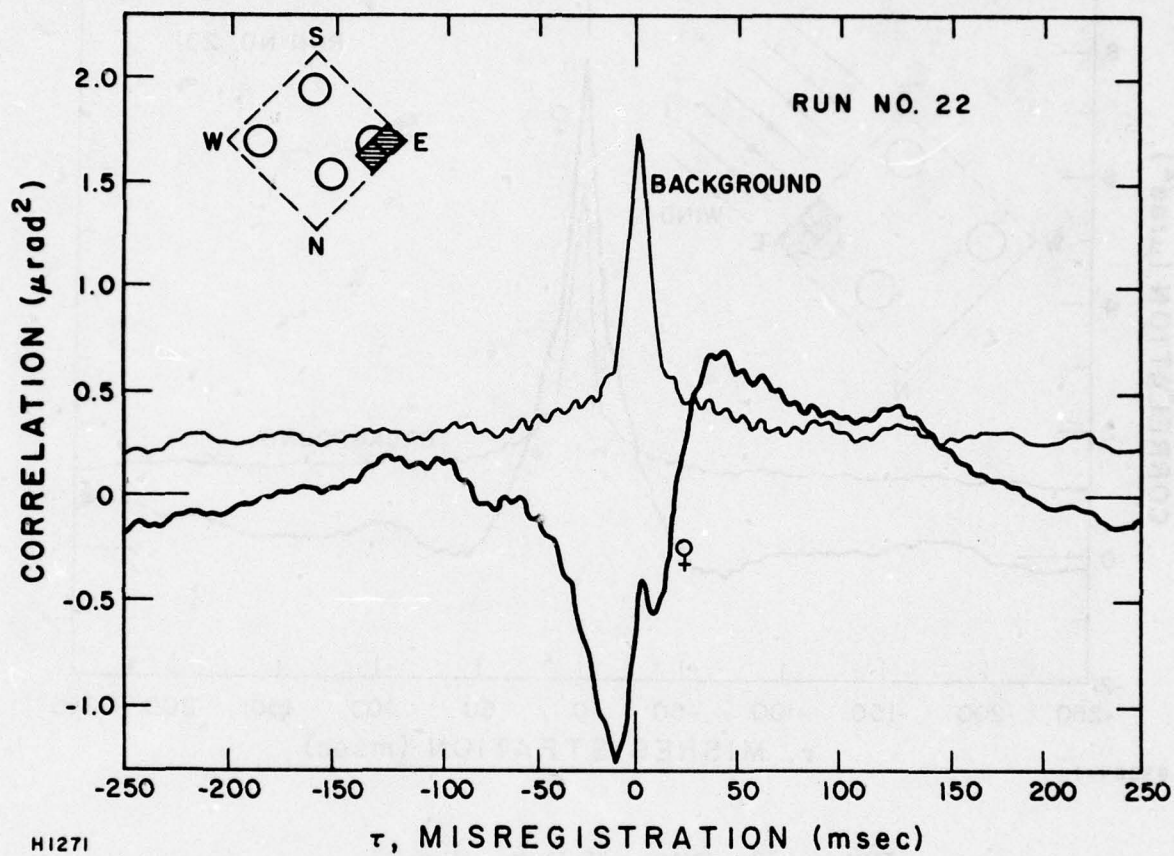


Figure 31 Filter #5 Data, Run 22

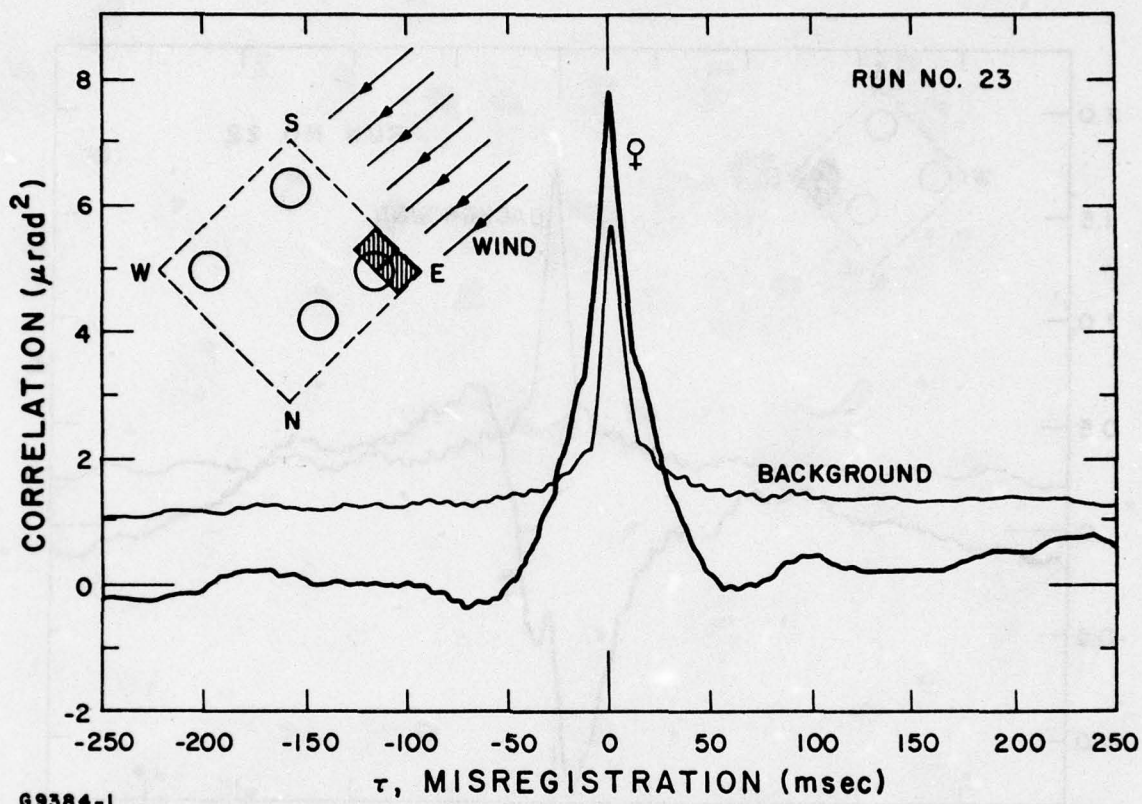


Figure 32 Filter #5 Data, Run 23

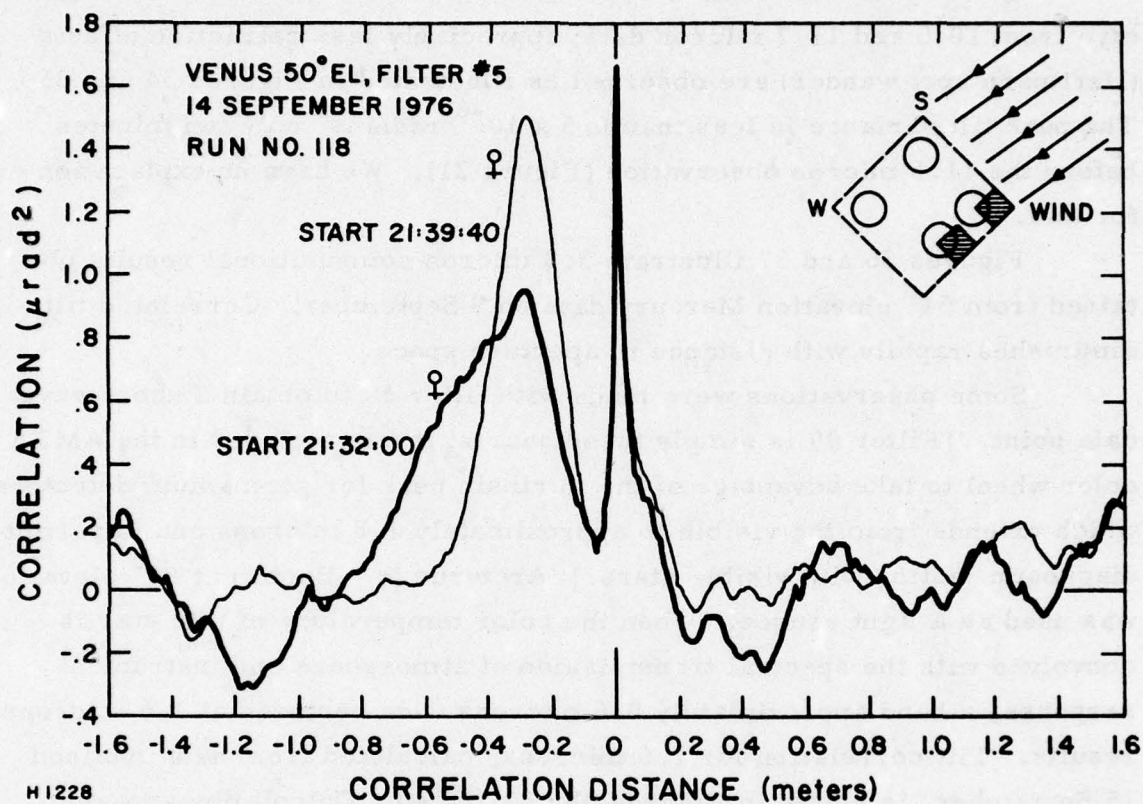


Figure 33 Filter #5 Data, Run 118



average of 256 one-second correlations, between 10.5 micron-band Venus signal histories for the cross-hatched detector pair. The crest-to-crest measurement is reasonably reproducible at 1.2 meters but the width of the maximum changes from 40 to 50 cm.

The results with filter #3 (8.7 microns) show an unexpected departure from 10.5 and 11.7 micron data; appreciably less refraction effects (Hartmann spot wander) are observed as illustrated in Figures 34 and 35. The peak tilt variance is less than  $0.5 \times 10^{-6}$  radians<sup>2</sup> only ten minutes before the 11.5 micron observation (Figure 21). We have no explanation for this.

Figures 36 and 37 illustrate 3.8 micron computational results obtained from 54° elevation Mercury data on 9 September. Correlated tilt diminishes rapidly with distance in aperture space.

Some observations were made with filter #9 to obtain a short wave data point. [Filter #9 is simply fused quartz; it was included in the AMTA color wheel to take advantage of the intrinsic peak for germanium detectors which extends from the visible to approximately 1.8 microns and to permit diagnostic testing with visible stars.] Arcturus ( $\alpha$  Bootis) at 80° elevation was used as a light source. When the color temperature of this star is convolved with the spectral transmission of atmosphere and instrument response, a band approximately 0.6 microns wide centered at 1.6 microns results. Tilt correlation for 1.6 microns, calculated from data obtained 15 September, is shown in Figures 38, 39 and 40. Calculating apparent wind speed as described earlier yields the correlation scale (in space instead of time) shown in Figure 40.

Data obtained at 4.8 microns and 18.8 microns requires special treatment and wasn't reduced. Figure 41 assembles results obtained thus far onto a single page. The plots illustrate how wavefront tilt correlation between detectors scales with detector separation and wavelength. The straight lines represent least squares power law fits to points computed from the data. There appears to be some trending with wavelength.

As explained in Section 2.0, amplitude scintillation effects are embedded in the data and are expected to produce positive signed correlation between temporally aligned detector signal histories. By summing together

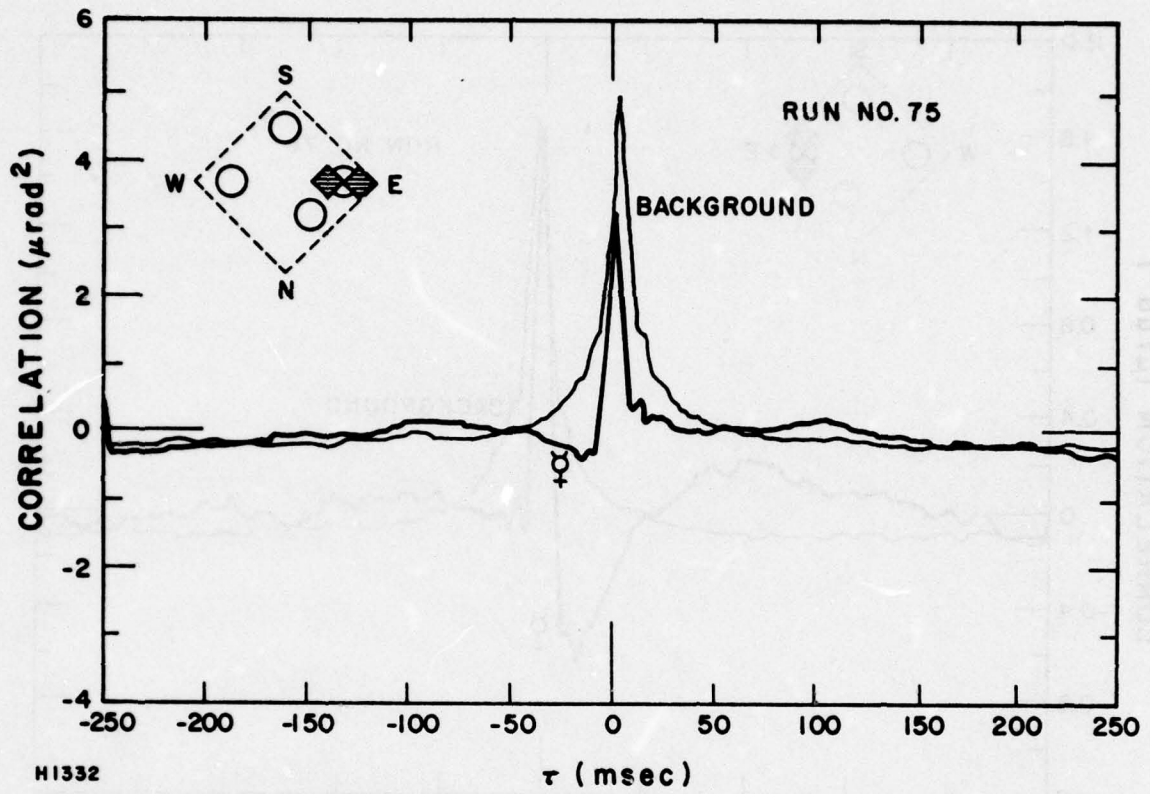


Figure 34 Filter #3 Data, Run 75

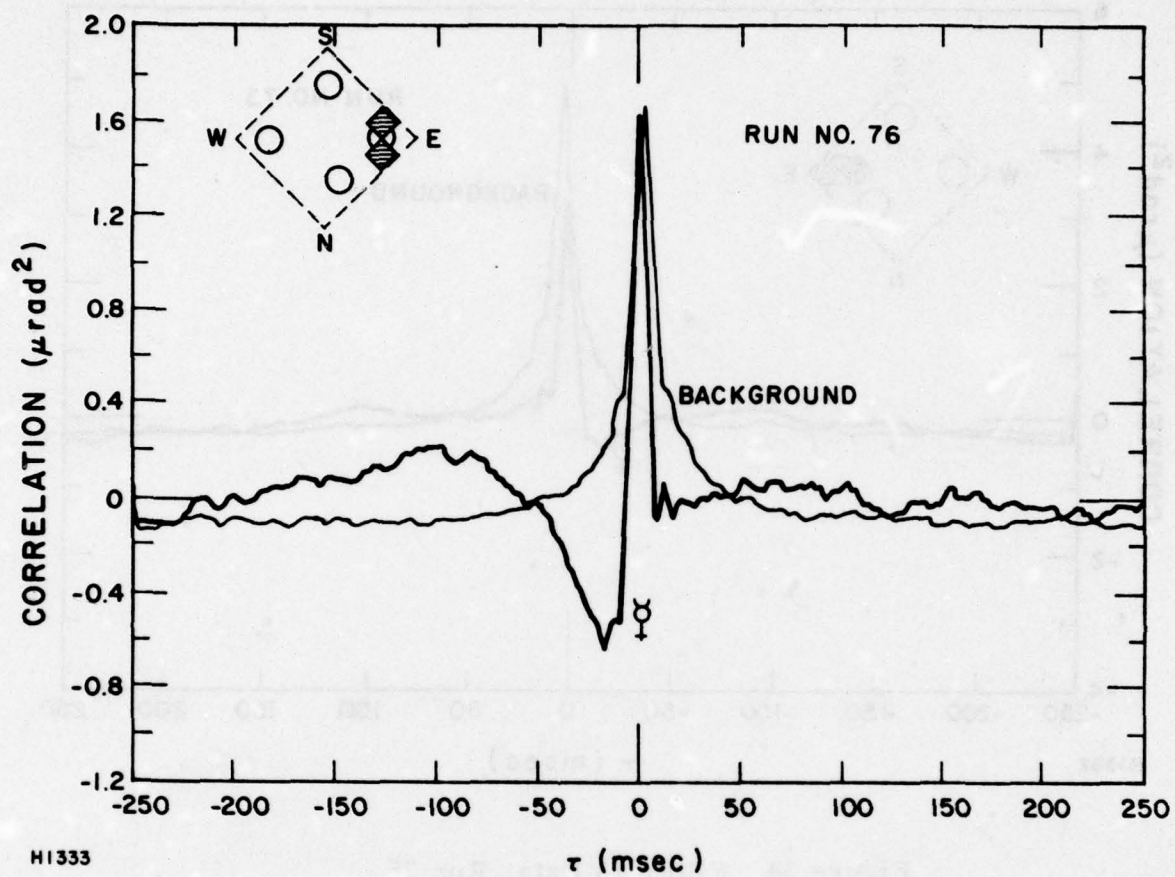


Figure 35 Filter #3 Data, Run 76



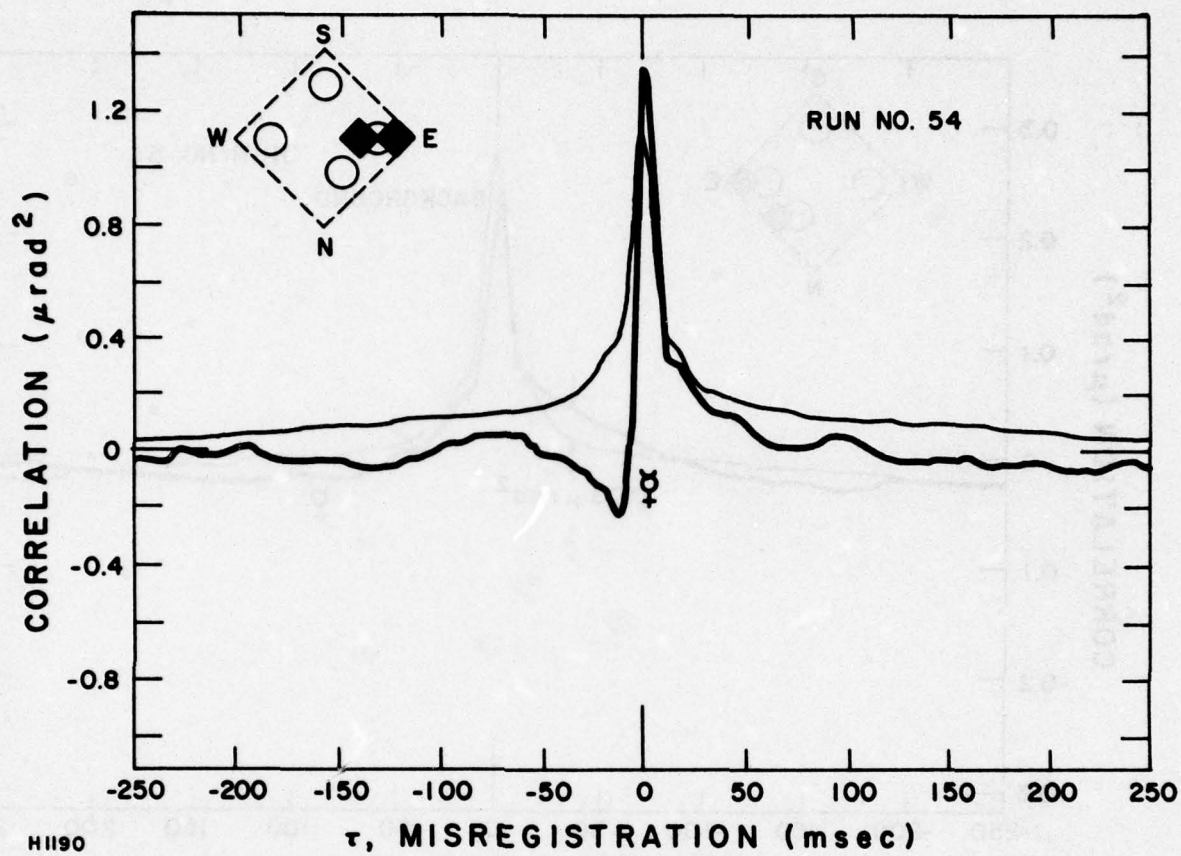
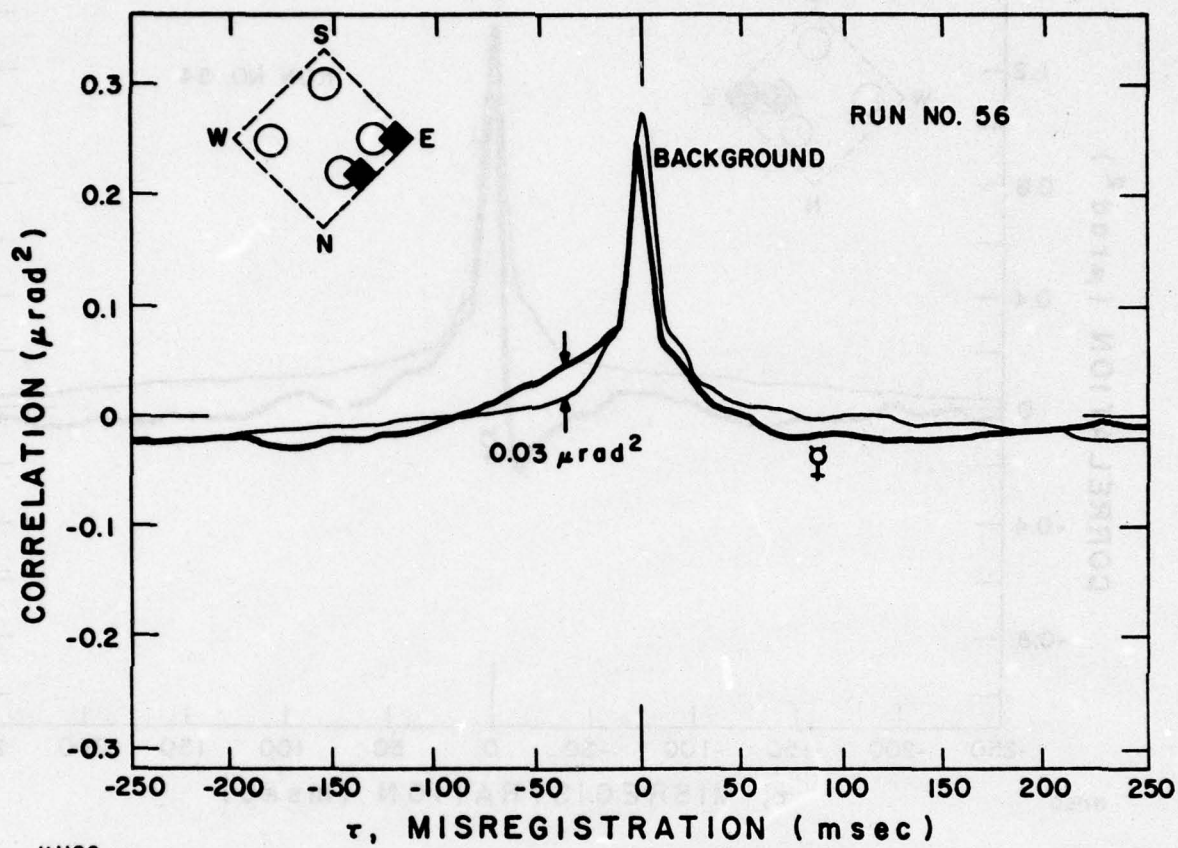


Figure 36 Filter #1 Data, Run 54



H1186

Figure 37 Filter #1 Data, Run 56

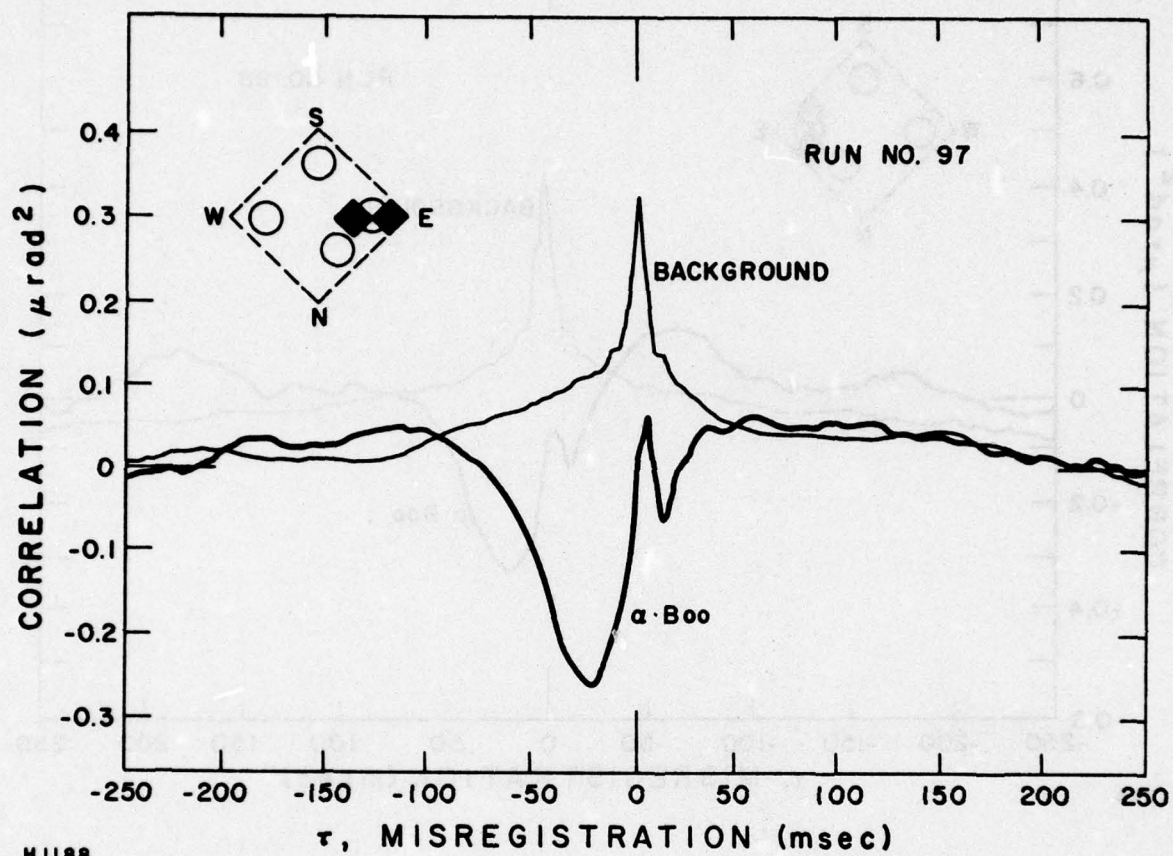
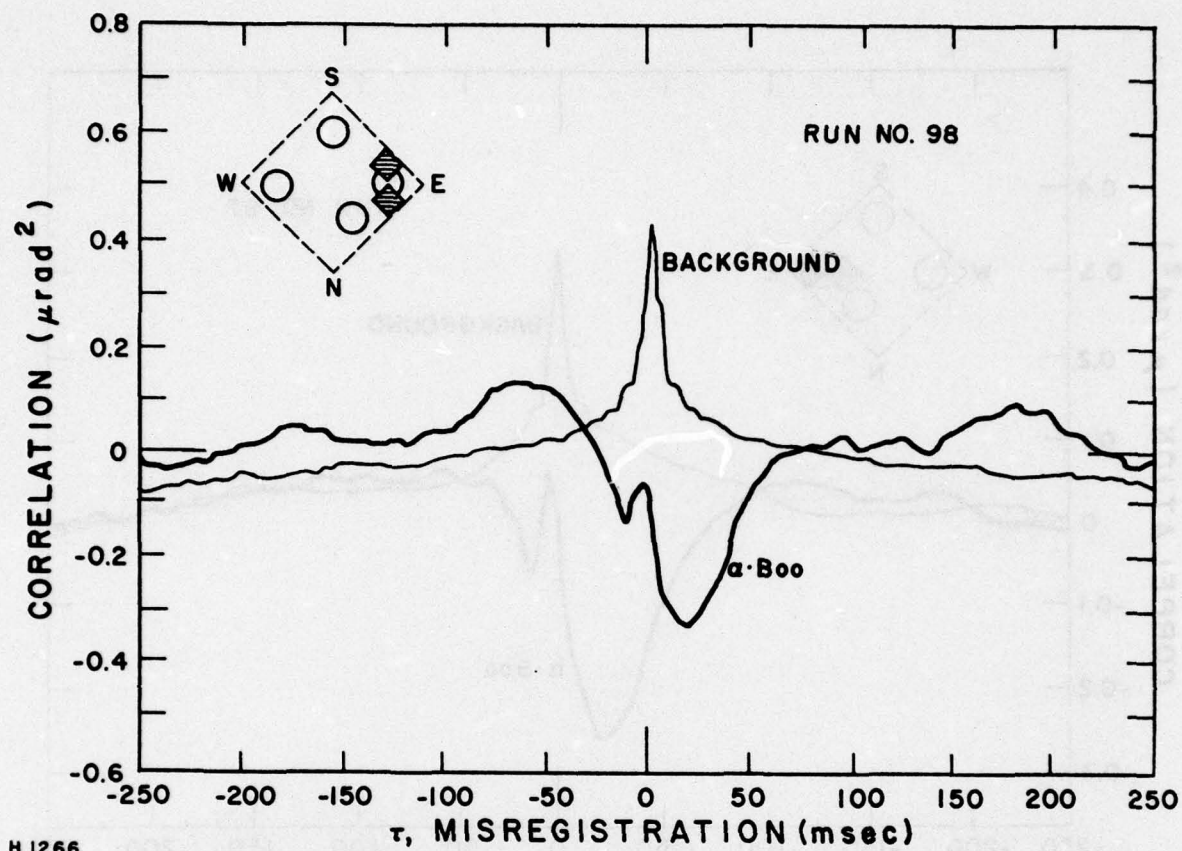


Figure 38 Filter #9, Data, Run 97





H 1266

Figure 39 Filter #9 Data, Run 98

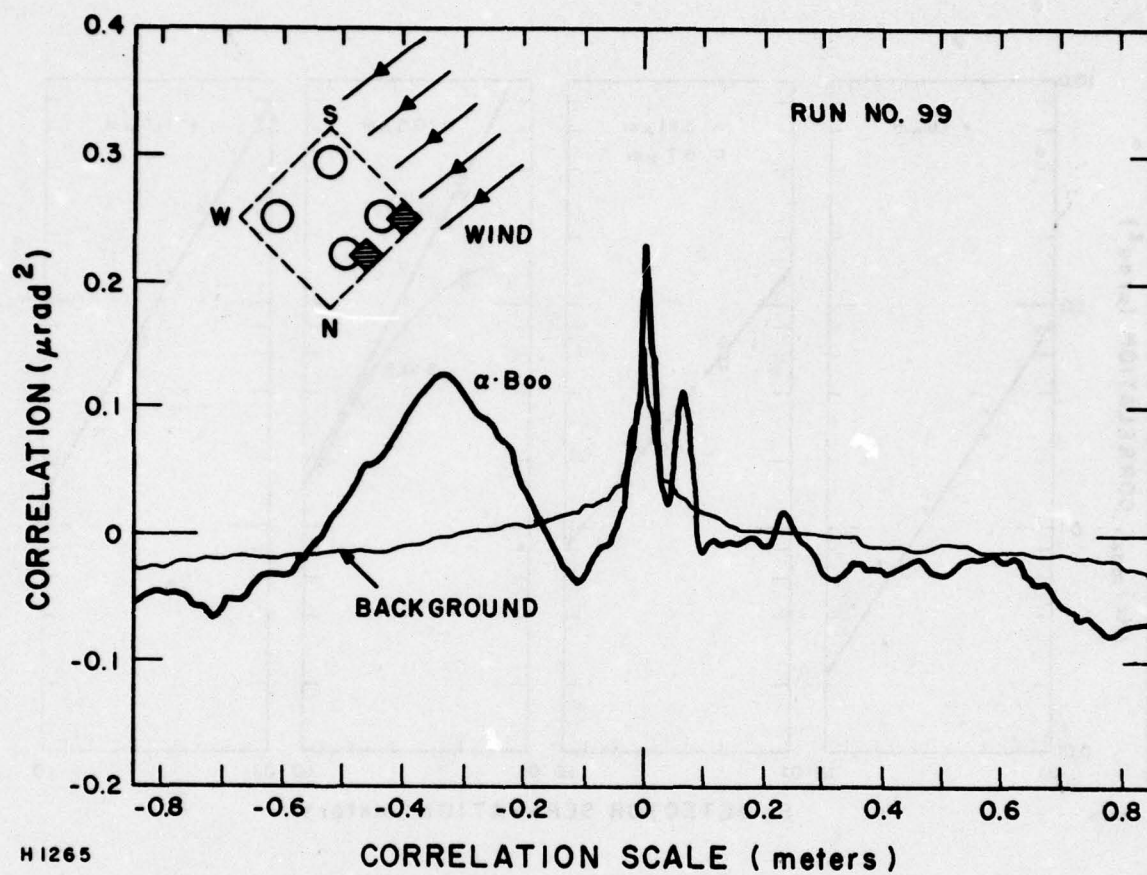


Figure 40 Filter #9 Data, Run 99

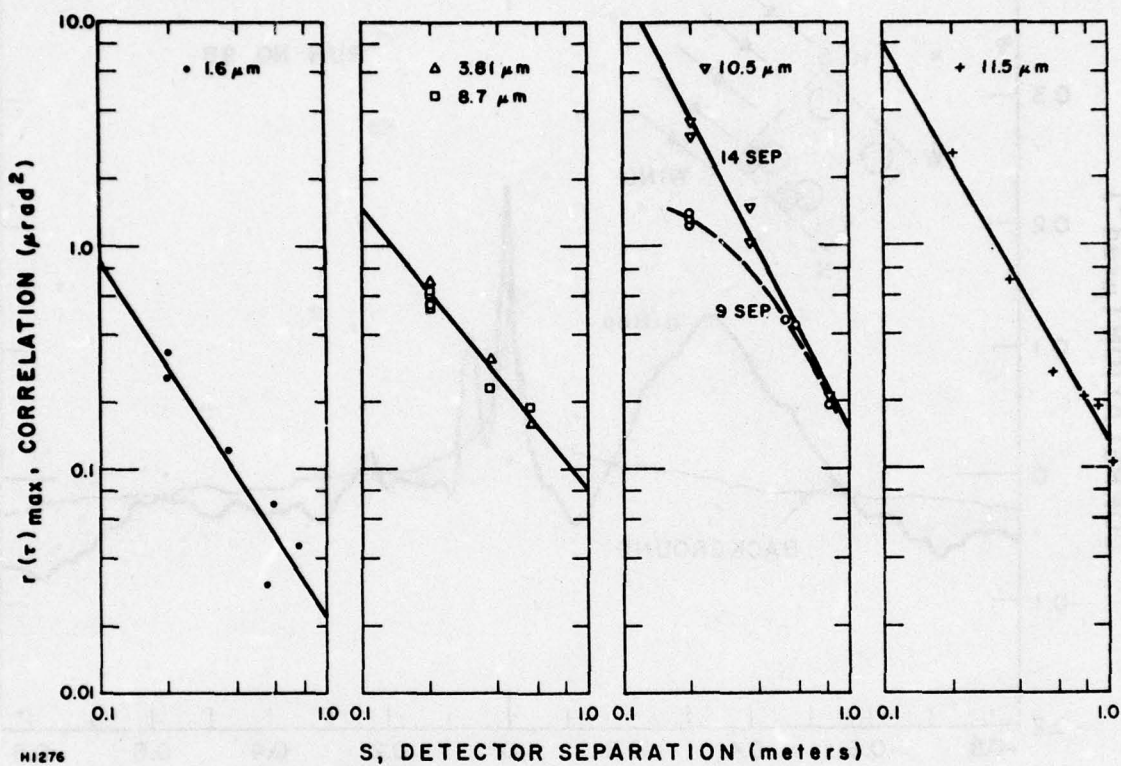


Figure 41 Tilt Scaling Summary



the four detectors of a quadrature set we obtain, in principle, the total intensity history for a single subaperture. Owing to differences in the sensitivity contours of independent detectors this isn't precisely true as illustrated in Figure 14. The figure shows calibration data which results from translating, in steps, a point radiance source in the Cassegrain image surface. Translating the source produces motion of the subaperture pattern projected onto the array and, consequently, the signal changes observed in the lower (staircase) trace. This trace is the sum of signals from the two detectors shown cross-hatched in the figure. The upper trace is the sum of four detectors, made for the same calibration run, and demonstrates the expected insensitivity to spot motion except for extreme excursions. The abscissa scale is in  $\mu$ radians. Since excursions in excess of  $12 \mu$ radians were infrequently encountered during the observations, variations recorded for the four set are probably not due to close-in refractive structure. Sample planet Mercury variations are shown in Figures 42 and 43 which are plots of the autocorrelation function for the sum of the four detectors illustrated. Ordinate scales are normalized to total inband irradiance and the traces are the result of  $4^{m}17^s$  signal averages. The peak 'twinkle' ranges between 2 and 3% for these  $10.5 \mu$ m and  $11.5 \mu$ m Mercury observations. The spectral density distribution is given by the transforms plotted in Figures 44 and 45.

The author wishes it known that he deeply appreciates the efforts of Dr. Merlin Miller, of the laboratory staff, who prepared the scaling estimates which established the measuring resolution required for the Hartmann experiment and the many hours of freely offered help and useful suggestions provided by Donald Ruffatto, of the observatory staff, during the course of preparations and the experiments.

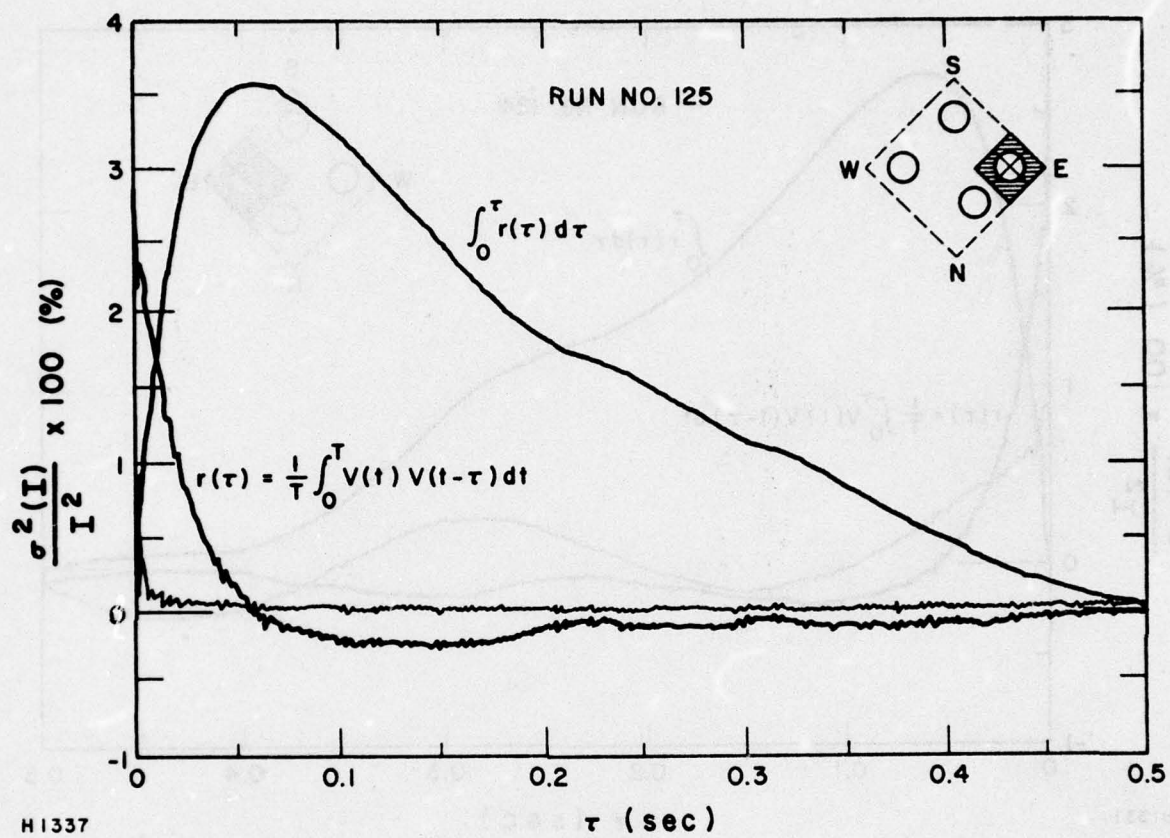


Figure 42 Four-Detector Autocorrelation, Run 125



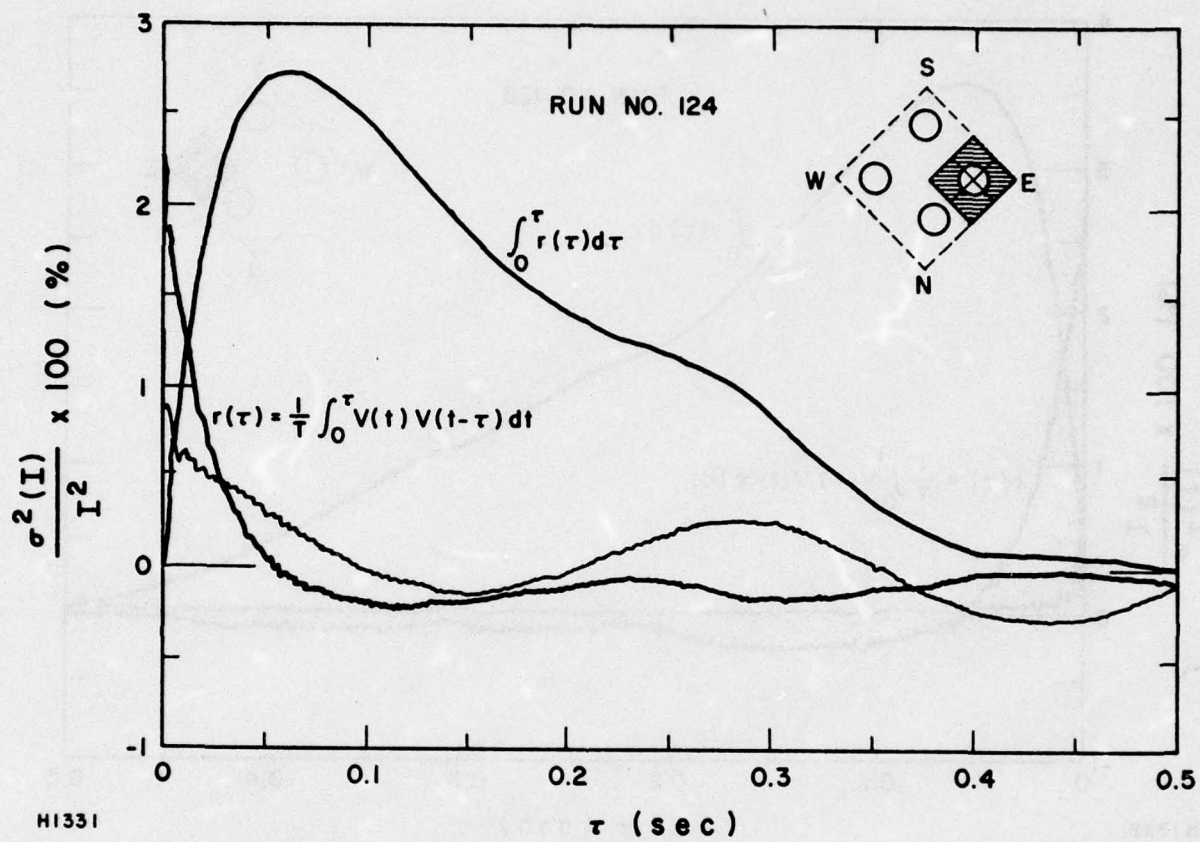


Figure 43 Four-Detector Autocorrelation, Run 124

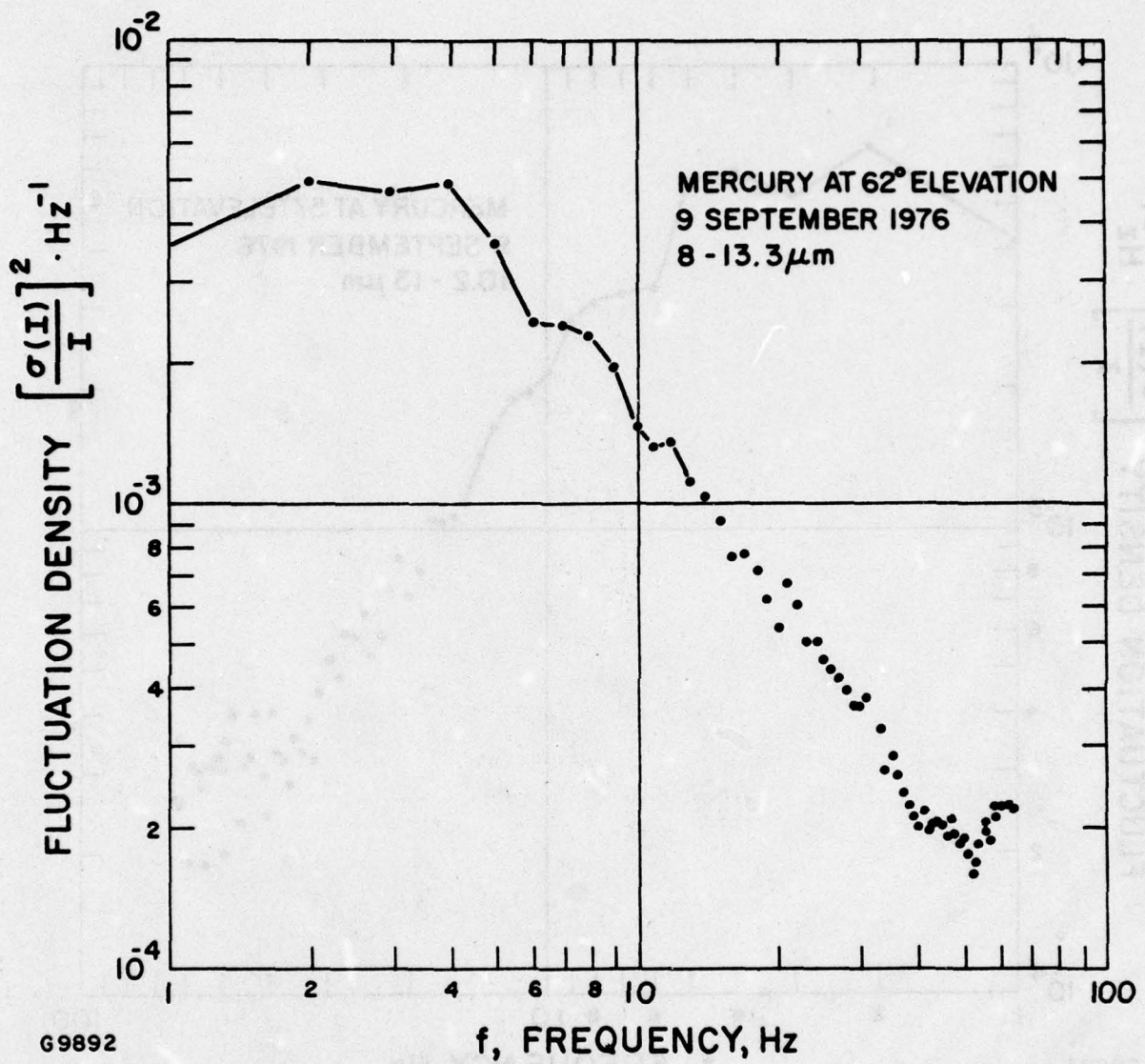


Figure 44 Scintillation Spectral Density

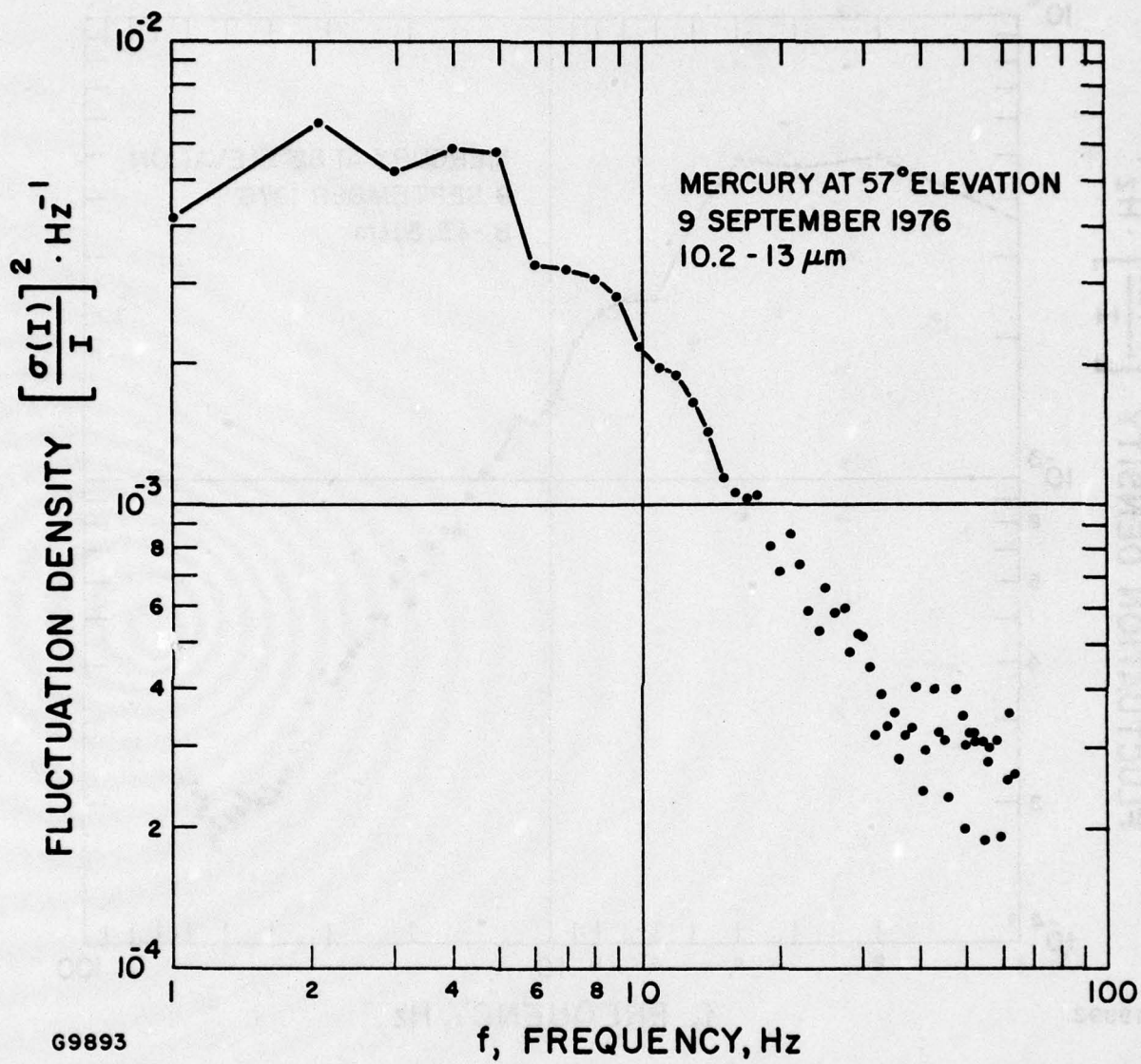


Figure 45 Scintillation Spectral Density



APPENDIX A  
ATMOSPHERIC ABSORPTION

1.0 SCOPE AND BACKGROUND

This addendum describes work performed and some interim results achieved through February 1976 on the IR Atmospheric Measurements Program.

The program consists of a series of instrumented observations intended: a) to characterize certain optical properties of earth's atmosphere and b) to demonstrate the feasibility of routinely determining the thermal signatures of deep-space earth satellites with an existing ~~satellite~~ AMOS. Work was begun by AERL in July 1975 in accordance with ~~contract~~ F30602-75-C-0235 as directed by DARPA's agent: RADC. The ~~program~~ modified program, was scheduled to be completed May 1977.

## 2.0 LONG INTEGRATION SIGNAL PROCESSING

Modifications to the signal conditioning and recording facilities of an existing long wave infrared sensor, AMTA, <sup>(1, 2)</sup> were authorized with the intent of enabling observations of faint deep-space satellites to be made with it routinely. AMTA, like all LWIR point-radiometers used under atmosphere for space observations, is limited in precision by fluctuating emission from both warm atmosphere and optics. At AMOS these two sources produce four to five decades greater flux level, at the detector surface, than typical targets. The line of sight of one or more AMTA detectors is deviated by an oscillating mirror to alternately encompass and exclude the target. AMTA's scan mirror is driven to follow a 45 Hz square-wave which toggles the line of sight 24 arc seconds, an angular distance corresponding to the detector spacing. In the absence of a target, thermal eddies in the atmosphere affect a noise-like detector output which must be integrated to produce a smooth mean value so the target, when present, will obtrude.

Although the spatial distribution of radiant structure in the atmosphere was of intense interest to the IR community in the late 1950's, rather little is available by way of study reports today. The Wiener spectrum <sup>(3)</sup> is one enduring description; it predicts the power spectral density of noise, produced by a slot scanning the atmosphere, will vary inversely with the square of spatial frequency. It has been suggested <sup>(4)</sup> that a corner ought to occur between one and ten cycles per radian, below which the spectrum is uniform. This description suggests that the noise recorded during an observation ought to be highly correlated between detectors which are separated by, at most, 550  $\mu$ radians. The background is expected to trend monotonically across the array and first order differencing between adjacent 'identical' detector channels should eliminate the influence of atmosphere.

1. This reference will be made available to qualified military and government agencies on request from RADC (OCSE) Griffiss AFB NY 13441.
2. This reference will be made available to qualified military and government agencies on request from RADC (OCSE) Griffiss AFB NY 13441.
3. University of Michigan report #IRIA 2389-7-X (July 1957).
4. D. Korff, private communication.



Figure A-1 shows how this is accomplished with AMTA. Owing to the toggling motion of the scan mirror and the large scale structure of background granularity, most of the detectors (for this illustration) output 45 Hz signals whose components are in phase between detectors. Detector channel #7 is subtracted from channel #13, therefore, background contribution from the two interfere destructively; if the radiant gradient is uniform and the detectors are identical, cancellation is complete. On the other hand, target signals from the two are out of phase to begin with so subtracting #13 - #7 sums target contributions. Fine atmospheric structure, photon arrival fluctuations, amplifier and detector self-noise is uncorrelated between channels; therefore using a pair of detectors improves S/N by  $\sqrt{2}$ . Unless the detector channels have identical responsivities, there will be a non-zero average for the difference, #13 - #7, even in the absence of a target. To overcome this effect the telescope line of sight is shifted to put the target on a second pair of toggling detectors for an equal amount of observation time. The change in the mean value of the signal history for each pair, produced by moving the LOS, is attributed to target and no observation time is lost while background is measured because the target is always in view.

Satellites and R/V's at slant ranges of 2500 km or less can be thermally characterized with a few seconds of data while small objects in synchronous orbit will require  $10^3$  seconds or longer. Satellites in Keplerian orbits provide the required observation time. (In principle, synchronous satellites can be observed indefinitely.) Unfortunately, AMOS experience teaches that background statistics are apt to be non-stationary over periods longer than an hour. Double differencing using 'tare' detectors helps to compensate for long term trending of the mean gradients of atmospheric radiance.

Figure A-2 shows the organization of signal conditioning and recording hardware. Four such two-detector signal processors comprise the long term averaging system. The band pass filter, illustrated in the figure, is optional. The analog to digital converter is a precision unit with 16-bit resolution which reads the first integrator 45 times per second. Two types of software are available: FAST and SLOW modes. For the first named, the summation register acts as a buffer storage only, and 45 readings for each of four processors is recorded on nine-track digital tape each second. The SLOW mode



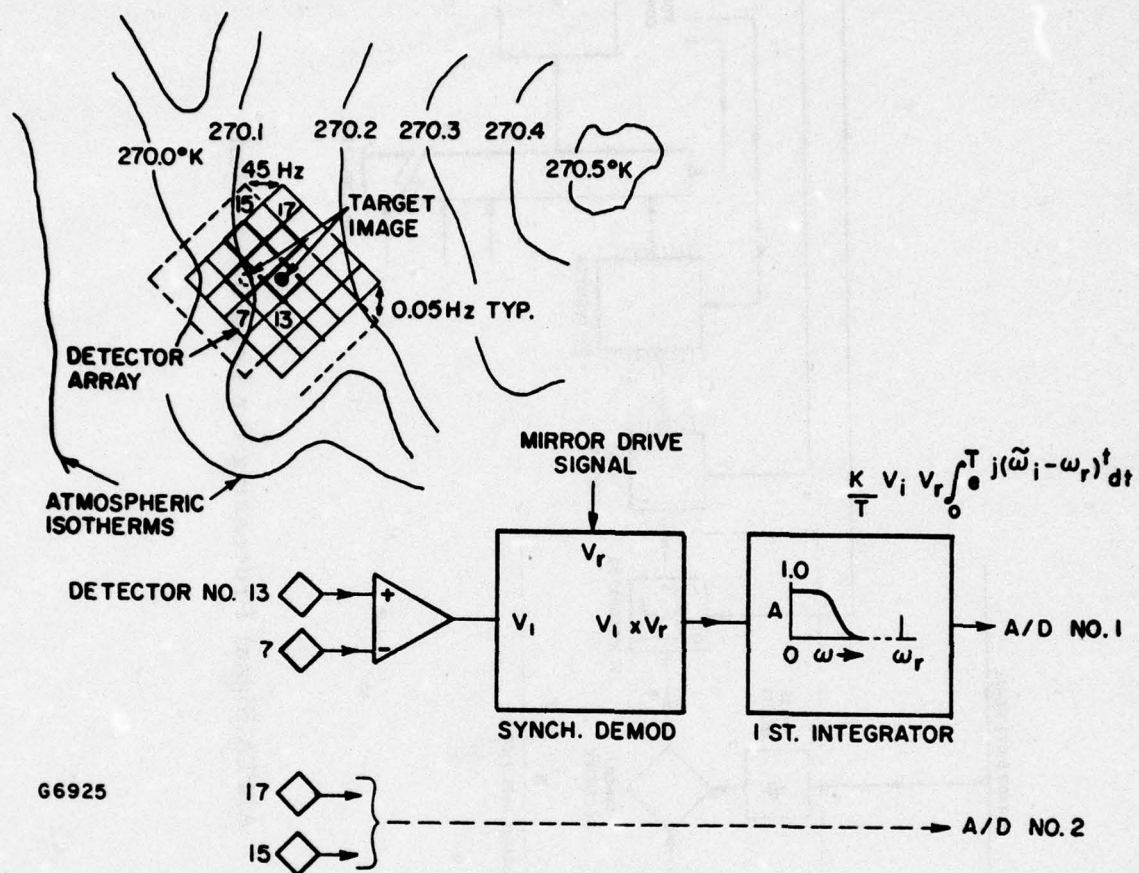
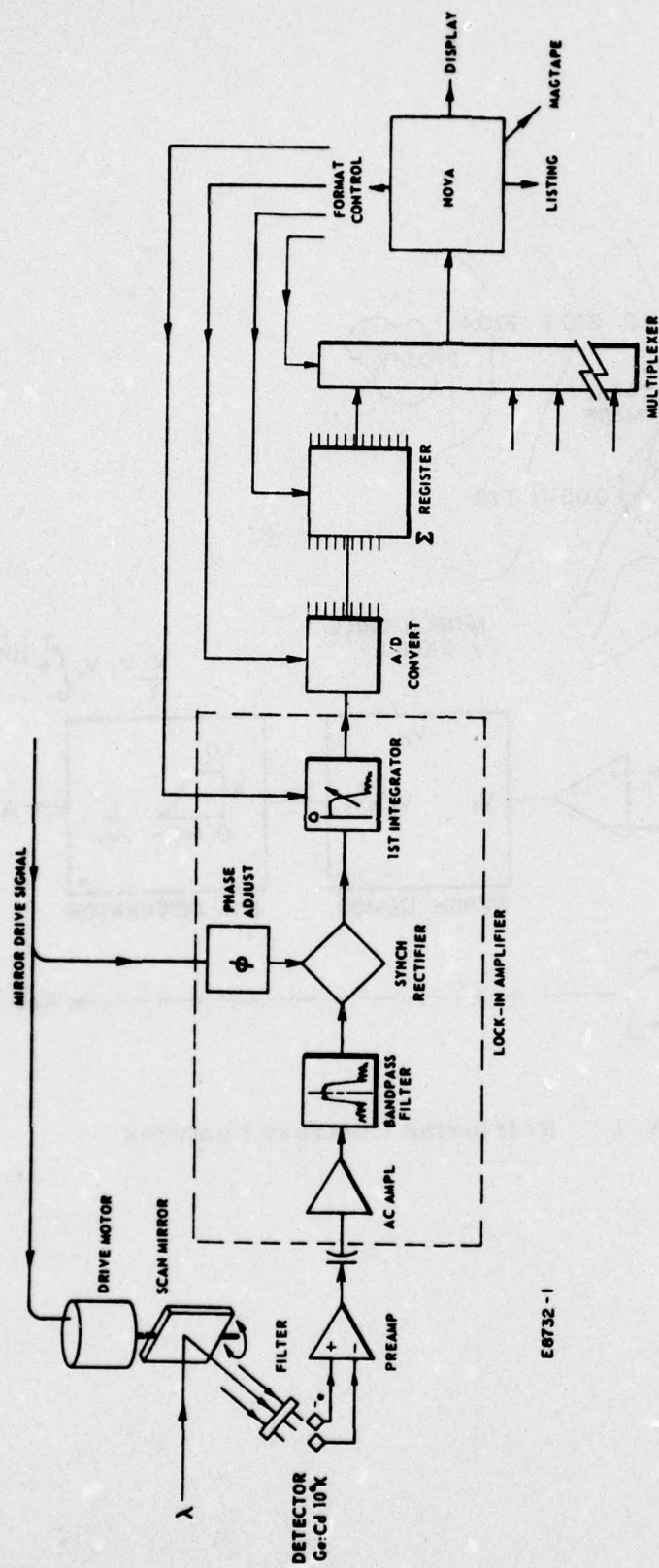


Figure A-1 Retrieving Contrast Features



E0732-1

Figure A-2 AMTA Signal Processing for Long Integration



permits real-time TTY interaction and recording with some sacrifice in time resolution: The average of 45 readings is recorded on tape once each second for each processor. The TTY will printout the average of the difference between (selected) pairs of processors once each (selected) averaging time. The minimum averaging time for this mode is ten seconds; the maximum is  $10^4$  seconds.

During the course of long observations the background signal, outputted by the first integrator, has changed by as much as a volt per hour (trending) while  $10^{-20} \text{ w} \cdot \text{cm}^{-2}$  target irradiance (a measuring goal) produces  $1.7$  to  $2.0 \times 10^{-5}$  volts. Seventeen bits are required to encompass this range. The 16-bit converters thus provide a  $2 \times 10^{-20} \text{ w} \cdot \text{cm}^{-2}$  uncertainty per reading. In principle, the mean value of a set of readings may be determined with greater than the encoding resolution by averaging. For example: if two value-adjacent (separated by one least significant bit) digital estimates exactly straddle the actual mean value the least significant bit will be 'lit' for exactly 50% of the sample readings. The average of sixteen readings should yield one additional bit resolution with 90% confidence. Sixteen-bit precision converters are available from two manufacturers. The only available converter with higher resolution is a state-of-the-art oven stabilized digital voltmeter, manufactured by Hewlett Packard, which offers one microvolt resolution over a  $\pm 1$  volt range (equivalent to 21 bits). One such instrument was incorporated into the system to monitor the performance of the other converters. Its BCD output, which represents a 1.1 second averaged reading is recorded once every two seconds along with the other data. The HP voltmeter is generally left in parallel with the 16-bit converter monitoring the detector pair closest to the nominal telescope line of sight.

Data processing includes calculating standard deviation, mean value and least-squares fit to first order trending with time for the average values obtained per telescope LOS dwell time. This is typically ten seconds so the 16-bit value is the average of 450 readings while the HP value is the (second) average of only five readings. Nevertheless, the HP values generally have 10% smaller normalized mean deviation for signal flux near threshold for five minute observations.



No manufacturer will describe the performance of an encoder, a voltmeter, or A/D converter beyond its LSB resolution. We tested the 16-bit units with signals incremented in steps smaller than LSB during system tests and again during operational tests at AMOS. The units did exhibit the ability to interpolate.

The key limitation to long term averaging is the accurate identification of all sources of trending. For this reason the detector bias voltage bus and the 'absolute' value of detector signals is impressed on the same nine-track tape. Changes in apparent sky brightness can be deduced from the absolute value history. Effective quantum gain for the photoconductors is a function of detector bias which controls charge mobility. Although the bias bus is reasonably well regulated, changes have been observed during long integration missions.

The nine-track record also includes radiometer filter number, Universal time from the observatory time code generator, three event flags and a typed-in initializing statement which identifies the mission name, date and detector channel assignments.

Calibration is accomplished by directing exitance from a chopper modulated reference black body into the telescope entrance aperture. The chopper is phase locked to the system 45 Hz reference signal which, at other times, drives the radiometer oscillating mirror. The reference source is mounted on the secondary mirror support structure of the 1.2 meter telescope. A remotely commanded mirror directs black body energy into the telescope as required. In practice, the dwell time for this mirror is adjusted to correspond to the dwell time employed for the on and off-axis detector channels by the telescope LOS during the mission. Atmospheric extinction is determined by observing standard stars and by best-fitting an absorptance model to sky radiance gradient data obtained in near real time.

## 2.1 RESULTS

LWIR flux from certain stars, two asteroids and a number of deep space satellites were measured with the new system in January 1976. Some results are presented here:

### Long Integration

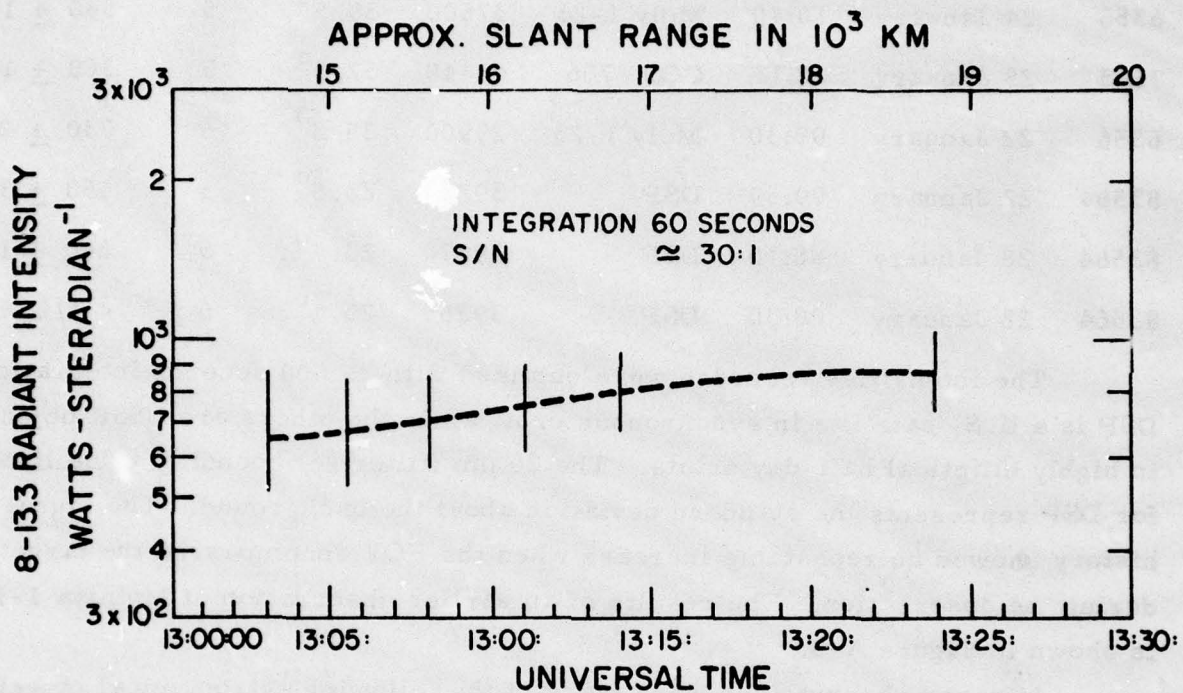
<u>ADC #</u>	<u>Date</u>	<u>Time</u>	<u>Name</u>	<u>Range</u>	<u>Elev.</u>	<u>Filter</u>	<u>Intensity w · ster<sup>-1</sup></u>
6356	24 January	10:40	Moly 1-23	37500	39.5°	5	530 ± 120
7625	23 January	08:15	COS #706	40440	52.5°	5	360 ± 160
6356	22 January	09:30	Moly 1-23	29900	39.8°	5	730 ± 250
83564	22 January	09:59	DSP	39223	23.0°	5	450 ± 360
83564	28 January	08:10	DSP	39270	23.1°	5	640 ± 136
83564	28 January	08:30	DSP	39269	23.1°	6	< 410

The intensities recorded were obtained with  $\leq 600$  seconds integration. DSP is a U.S. satellite in synchronous orbit while the others are USSR objects in highly elliptical half-day orbits. The 20  $\mu\text{m}$  (filter #6) bounding value listed for DSP represents the standard deviation about the background. The signal history showed no repeatable increase when the FOV encompassed the target during the observation. The results of an earlier observation of Molniya 1-19 is shown in Figure A-3.

Infrared observations were made of the following astronomical objects:

<u>Star Name</u>	<u>AMTA Filter #</u>	<u>Objectives</u>
$\beta$ And	2, 5, 6	Calibration and extinction determination
$\alpha$ Tan	2, 5, 6	" " "
R Leo	2, 5, 6	" " "
R Hya	2, 5, 6	" " "
MNL Cyg	5, 6	" " "
$\epsilon$ Per	5, 6	Long average observation
$\delta$ Tan	5, 6	" " "
$\gamma$ Hya	5	" " "
$\beta$ Her	5	" " "
$\tau$ Pup	5	" " "





G6986

Figure A-3 Molniya 1-19 Thermal Signature



<u>Asteroids</u>	<u>AMTA Filter #</u>	<u>Objectives</u>
Ceres	2, 5, 6	Temperature measurement test
Juno	5, 6	" " "
Vesta	2, 5, 6	" " "

The first five are bright, familiar, infrared stars which, with the exception of  $\beta$  And, are used for AMTA calibration in support of observations generally not requiring integration beyond one second. The signatures obtained for  $\alpha$  Tau, MNL Cyg, R Leo and R Hya were repeatable night after night within  $\pm 2\%$  and correspond to catalog values<sup>(5, 6)</sup> within  $\pm 9\%$  for filters #5 and #2. Correspondency at 20  $\mu\text{m}$  (filter #6) was considerably poorer:  $\pm 58\%$  or 0.5 stellar magnitudes. This is probably due to incorrect atmospheric extinction assumptions. Considerably fewer  $m_Q$  observations are published than either  $m_N$  or  $m_M$ . AMOS brightness results for  $\beta$  And compare well with recent observations by F.J. Low and G. Rieke:<sup>(7)</sup>

	$m_M$	$m_N$	$m_Q$	$T_{\text{eff}}(N/Q)$	$T_{\text{eff}}(M/N)$
AMOS	- 1.87	- 2.13	- 2.41	1300°K	2740°K
Ref 7	- 1.97	- 2.05	- 2.20	2130°K	5500°K
$\lambda_{\text{eff}}$	5 $\mu\text{m}$	10.6 $\mu$	21 $\mu\text{m}$		

The temperatures listed are calculated by fitting the indicated two color spectral irradiances to a black body.  $\beta$  And is listed<sup>(8)</sup> as spectral type MO III star, which suggests<sup>(9)</sup> a visual color temperature of 3200°K, and as a suspected variable,<sup>(8)</sup> which might easily account for the different apparent temperatures observed.

5. J. Heath, AMOS Star Library, Lockheed Missiles and Space Company, Inc. (April 1974).
6. F.J. Low, Sky Survey, Semi-Annual Technical Report, AFCRL #70-0179, Univ. of Arizona (15 March 1970).
7. N. Carleton (editor), Methods of Experimental Physics, Vol. 12, Astrophysics, p. 453, Academic Press, N.Y. (1974).
8. D. Hoffleit, Catalog of Bright Stars, 3rd Ed. Yale University Observ. (1964).
9. C.W. Allen, Astrophysical Quantities, 3rd Ed. p. 206, Univ. of London, Athlone Press (1973).

The next five stars listed in the observation table are much fainter. These were selected to demonstrate that familiar visual stars which are known to be stable and free of spectral trauma (principally class V, sun-like stars) should have predictable signatures in the LWIR. If this proves to be true, such stars provide useful calibration standards now that long integration has produced the required sensitivity. Excepting  $\delta$  Tau, none of those observed are listed in our rather extensive LWIR star catalogs. Reference 6, which describes observations made before March 1970, reports  $m_N = +2.55$  for this star. Our own measurements indicate  $m_N = +1.50$  and these results repeat within 0.3 stellar magnitudes.

Of the three asteroids observed two, Ceres and Juno, yield temperature and diameter estimates while Vesta exceeded background only for  $5 \mu m$  (filter #2). I suspect we were actually looking at an  $m_V = +8.9$ , KO star (GC 818). The apparent surface temperature of the asteroids Ceres and Juno was measured using the newly installed system. Multicolor data from 20 and 22 January observations were also used to determine size and surface albedo for these objects. The newly developed atmospheric extinction models were used for filter #6 data.

	$m_{ph}^{(10)}$	radius, km		Range, km <sup>(10)</sup>	Temp <sup>o</sup> K	$a_S$
		AMOS	Allen <sup>(9)</sup>			
Ceres	+ 7.7	$409 \pm 34$	380	$3.049 \times 10^8$	$235 \pm 7.4^o K$	0.86
Juno	9.6	$155 \pm 33$	100	$2.693 \times 10^8$	$215 \pm 18.3^o K$	0.51

It is assumed that these objects radiate as grey bodies between 8 and  $22 \mu m$  with emissivity something like earth's moon, i.e.:  $\epsilon_{TH} \approx 0.89$ .

In the regime where  $e^{C_2/\lambda T} \gg 1$  spectral intensity of thermal radiators is exponentially proportional to inverse temperature, and obversely, temperature is given by

$$T = \left[ K_1 \ln \frac{I_{\lambda 1}}{I_{\lambda 2}} + K_2 \right]^{-1}, \quad I_{\lambda 1} \text{ and } I_{\lambda 2} \text{ is intensity at } \lambda 1 \text{ and } \lambda 2. \quad (A-1)$$

For AMTA filters #5 and #6  $K_1 = 1.8833 \times 10^{-3}$  and  $K_2 = 5.0602 \times 10^{-3}$ , as determined from baseline measures of instrument parameters, where



T is in °K. Spectral intensity (or exoatmospheric irradiance) was established by instrument response to known black body existence and correcting for atmospheric extinction. Temperatures listed in the table are the average of four permutations of two data sets, for each color, for each of two detectors. Area is calculated directly from exoatmospheric irradiance because range is known.<sup>(10)</sup> The objects are assumed to be spherical.

Albedo is calculated from the temperature as follows: for passive grey bodies in equilibrium with solar radiation, temperature goes with inverse square root of solar distance and the maximum temperature a grey body can reach is  $393.6^\circ\text{K}/\sqrt{R}$ ; where R is solar distance in A. U. The measured temperature, a function of the optical properties of the surface, is given by:

$$S_o a_s = \sigma \epsilon_{TH} T^4 \quad (\text{A-2})$$

where  $S_o$ ,  $a_s$ ,  $\sigma$  and  $\epsilon_{TH}$  are the solar constant, effective absorptance of the surface for solar radiation, Stefan-Boltzmann constant and thermal (total hemispheric) emissivity, respectively. For grey bodies  $a_s \equiv \epsilon_{TH}$  and

$$T_{\max}^4 = \frac{S_o}{\sigma} = \frac{(393.6)^4}{R^2} \quad (\text{A-3})$$

Albedo is then given by

$$1 - a_s = 1 - \frac{R^2 T^4}{(393.6)^4} \epsilon_{TH} \quad (\text{A-4})$$

Observation of Ceres, Juno and stars for calibrating the sensor yielded data for calculating NEFD; some results are given here:

NEFD, Filter #5				
Integration Time				
Det. #	1 sec	120 sec	360 sec	600 sec
13	18Z	4.9Z	1.1Z	0.77Z
25	13Z	3.2Z	2.5Z	0.76Z

10. American Ephemeris and Nautical Almanac for 1976, U. S. GPO.



NEFD, Filter #6				
Integration Time				
Det. #	1 sec	120 sec	360 sec	600 sec
25	26Z	6.2Z	4.3Z	
13	21Z	3.7Z		2.4Z

The noise equivalent flux density is determined from the standard deviation about the mean for stellar signals. Popular practice for reporting sensitivity entails dividing measured s. d. by the square-root of the number of readings; while this yields a more satisfying result, it is mathematically correct only for stationary random processes where the individual readings are truly independent. With long term trends produced by small local weather condition changes one cannot be certain the statistical properties of the background remain stationary. Note that these results apply to single detectors: #13 and #25, not combinations of two adjacent detectors discussed earlier. The double differencing capability had not been tested during the performance period covered by this report.

### 3.0 ATMOSPHERIC EXTINCTION SCALING - TASK 4.1

Thermal observations of foreign satellites can yield important mission clues. The effective surface temperature of operational satellites may be determined by making multi-color measurements of thermal exitance. When such observations are made from beneath atmosphere extinction correction uncertainties at long wavelengths can seriously limit the validity of conclusions. The principal source of uncertainty is the amount of  $H_2O$ , which strongly affects absorption in the Q-window (16-23  $\mu m$ ) region, along the line of sight. On mountain tops, where abrupt weather modifications are common, water vapor content changes so rapidly that extinction, determined by observing stars, may not be applicable to a satellite measurement made an hour later. During the course of LWIR observations we have recorded<sup>(1)</sup> a monotonic sky signal increase, correlated with increasing zenith distance, when the instrument is scanning clear sky. At 20  $\mu m$  this signal is principally due to thermal emission from atmospheric water vapor as shown in Figure A-4. By measuring radiance gradient an absorption model may be calculated. Moreover, if the radiometer is arranged to provide an absolute measure of background radiance, extinction may be deduced for a satellite mission even when there is no orderly relation between absorptance and zenith distance.

To prove this concept facilities for measuring and recording mean detector resistance for ten detector channels were incorporated into the AMTA system. This facility shares (see Figure A-5) a tape recorder, rack space and a minicomputer with the long period averaging system described earlier in this report. Resistance (actually d.c. detector output) is monitored, digitized, multiplexed, averaged and recorded on nine-track digital tape along with the contrast data from astronomical and satellite observations without interfering with or degrading AMTA performance in any way. The hardware was installed at AMOS in December 1975 and became operational in January. Figure A-6 is a system block diagram of the extinction measuring add-on for AMTA.



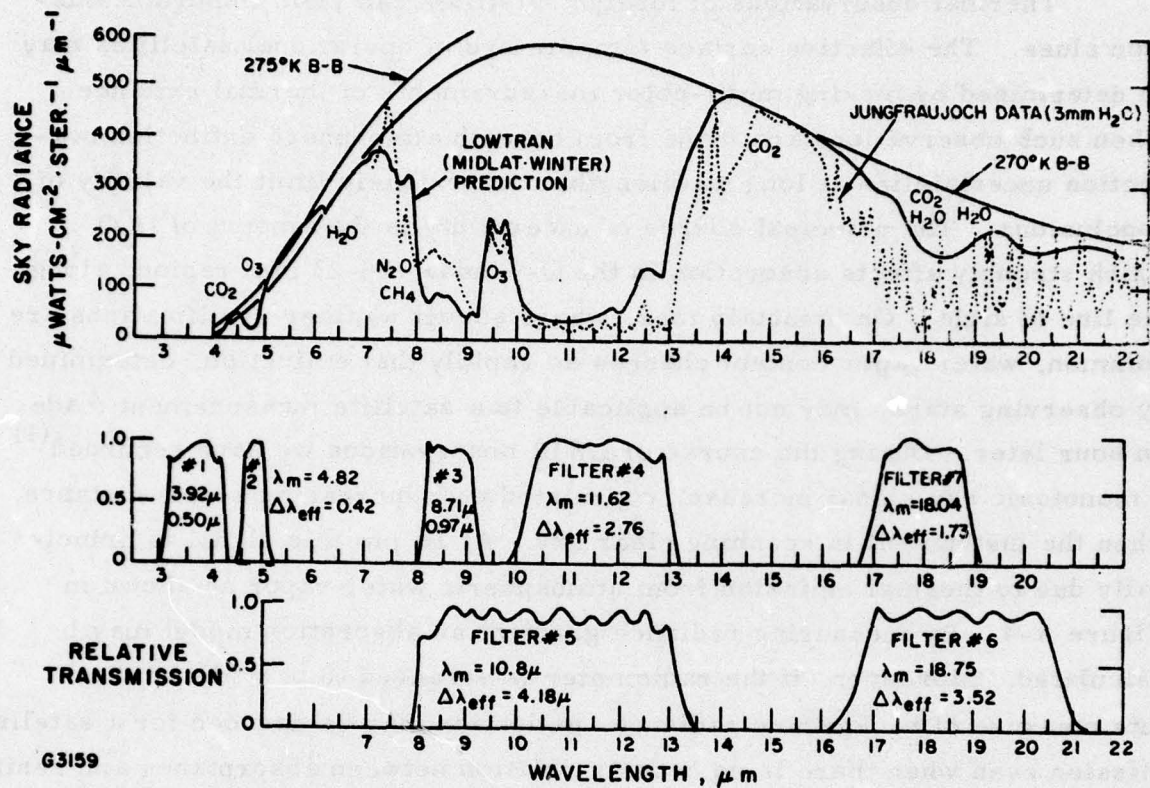


Figure A-4 Sky Radiance Measurement



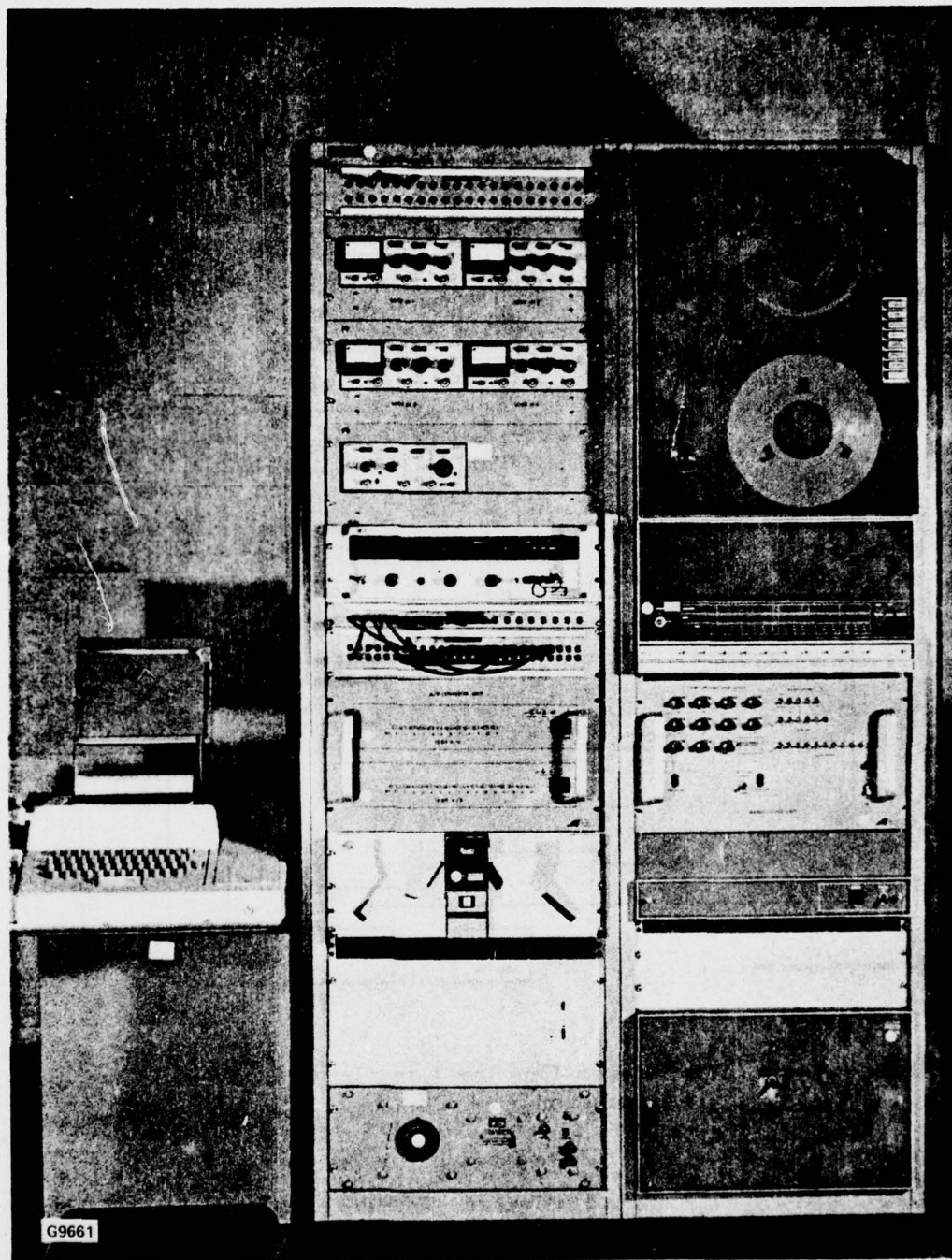


Figure A-5 AMTA Add-Ons for Long Duration Observations

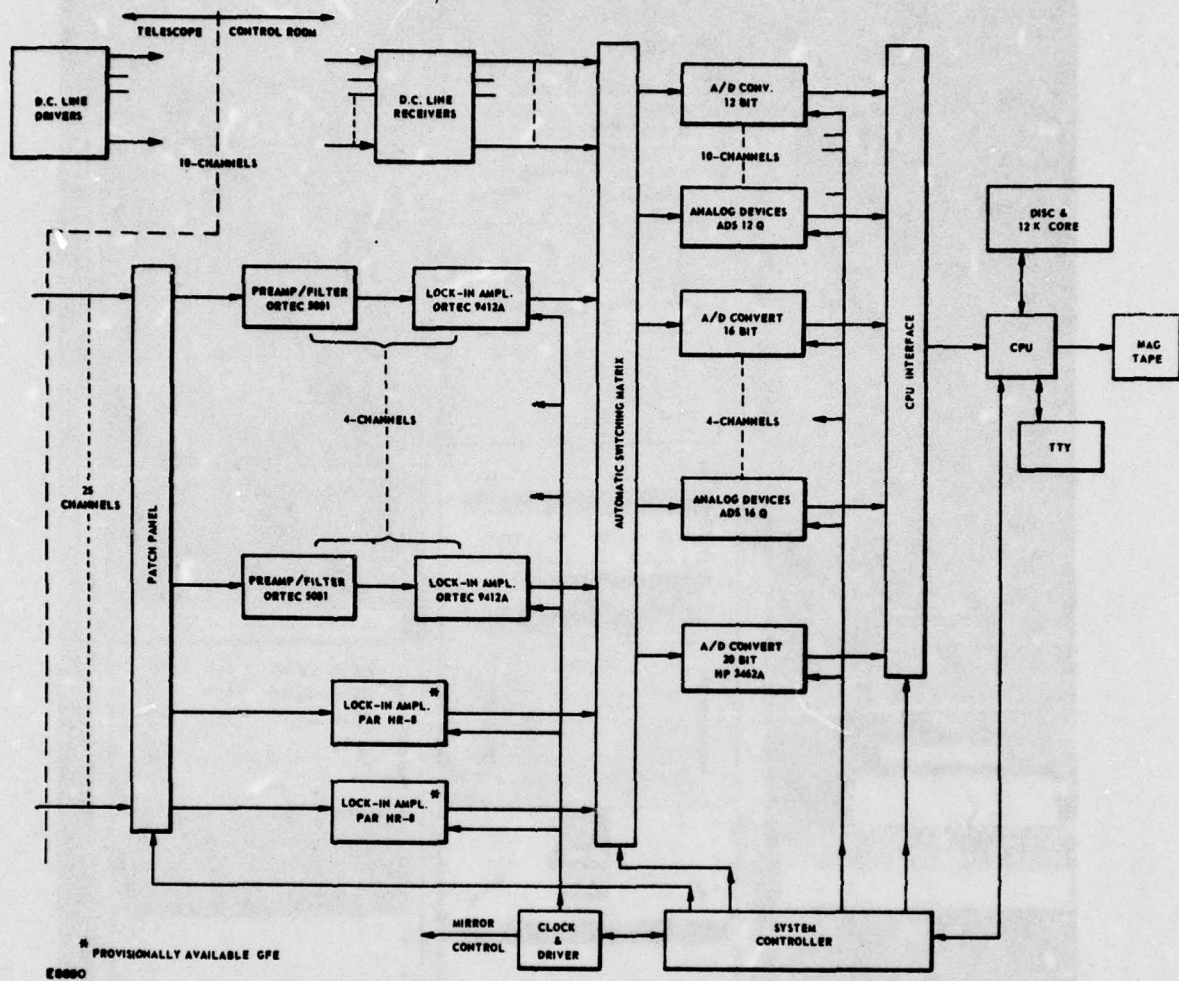


Figure A-6 AMTA Add-Ons for Long Integration and Atmospheric Transmission



The d. c. output of each of ten detectors is digitized with 12-bits per ten volts resolution, eight times each minor scan cycle. The four readings for each of the two scan mirror positions are averaged and recorded separately. This produces ninety recorded readings, each second, for each detector. These numbers are retrieved from tape and averaged to any desired degree of smoothness along with the mission data. An eleventh 12-bit A/D converter monitors detector bias which is also recorded on tape ninety times per second.

Detector voltage is related to absolute radiance by means of the same black body reference source used to interpret mission data. To unwind instrument bias and off-set due to emission of the optics the sensor filter wheel is rotated to block all detectors with an opaque port refrigerated, like the filters themselves, to  $\approx 40^{\circ}\text{K}$ . The detector array lies at the bottom of a cylindrical low reflectance light shield and is maintained at  $11^{\circ}$  to  $14^{\circ}\text{K}$ . The array semiconductors will not respond to photons less energetic than  $22\text{ }\mu\text{m}$ ; the blocked light shield thus establishes the 'zero photon' detector resistances. Next, the blocking port is replaced with the interference filter(s) to be used during the mission; (the AMTA filter wheel is remotely commanded and its disposition is automatically recorded on the data tape once each second) and the telescope dust-covers are closed. The resulting detector outputs represents response to the optical train exitance with assumed unity emissivity. The calculated emissivity for all cascaded optical surfaces which are not refrigerated is  $\epsilon = 0.205$ . This value is applied to the difference between the dust cover reading and the blocked detector reading to establish what fraction of the output, recorded during the measurement, to attribute to warm instrument optics.

In January 1976 tests were conducted with the newly installed hardware to confirm the validity of relating atmospheric brightness to transmission. Measurement procedures were described in MIOP 015 (Mission Instruction and Operational Plan) distributed at AMOS. The data taken in January did produce a plausible zenith distance related expression for atmospheric extinction but sufficient 'standard star' observations to fully validate the model were not undertaken, due to press of other work. The model at  $20\text{ }\mu\text{m}$  (filter #6) assumes, since most of the water is in the first 2 km above AMOS, that a temperature scaled 1.4 km above altitude can be assigned to the dominant radiating constituent and that the output produced by looking just above  $0^{\circ}$  elevation is representative of total absorption ( $\epsilon = 1.0$ ).



The data tapes were reduced in Everett where software for computing extinction from spectral radiance data was completed and exercised with "sky scan" radiance data obtained from AMOS as a result of January activities there.

The apparent spectral radiance of the atmosphere is attributed to its effective temperature and emissivity. A radiance gradient measurement will yield emissivity and transmission since  $1 - \epsilon(\lambda) = \tau(\lambda)$ . Transmission as function of elevation angle is given by

$$\tau(\lambda) = \exp \left( \frac{-\alpha(\lambda)}{\left( \frac{P_o}{P_h} \sin El \right)^{\beta(\lambda)}} \right) \text{ for uniform exponential atmosphere (A-5)}$$

above  $\approx 10^\circ$  elevation (4 air masses at AMOS).  $P_h$ ,  $P_o$  are atmospheric pressure at the altitude of the observer and sea level respectively; and  $\beta(\lambda)$  is a number,  $\leq 1.0$ , depending upon the concentration profile of the absorbing medium and whether the line absorbers are saturated. In the visible, where extinction is attributed primarily to scattering and the medium is tenuous for broad spectral intervals,  $\beta(\text{vis}) = 1.0$ . In the LWIR where molecular absorption dominates, and the line centers are apt to be saturated, theory predicts  $\beta(\lambda) \geq 0.5$ . The radiance data obtained in January seems to bear this out at  $19 \mu\text{m}$  but not at  $10 \mu\text{m}$ .

When fully developed the sky foreground radiance measuring scheme promises to permit unwinding the transmission affected modulation, produced, e. g., by the line-of-sight crossing patches of localized water vapor, from proper target attitude change affected signals. Figure A-7 illustrates just such a disorderly sky during the 'Filter #2' data run. In the figure detector output voltage is related to zenith distance expressed in sea level equivalent air masses. Experiments conducted in January, however, were designed to prove the general concept and data was fitted to a monotonic sky model.

The data recorded on magnetic tape 22 January 1976 consists of a time-tagged history of d. c. voltage outputted by five detector channels while the telescope stepped in elevation from  $+4^\circ$  to zenith in accordance with a pre-arranged schedule. Since detector channel output change is linearly proportional to radiance change:

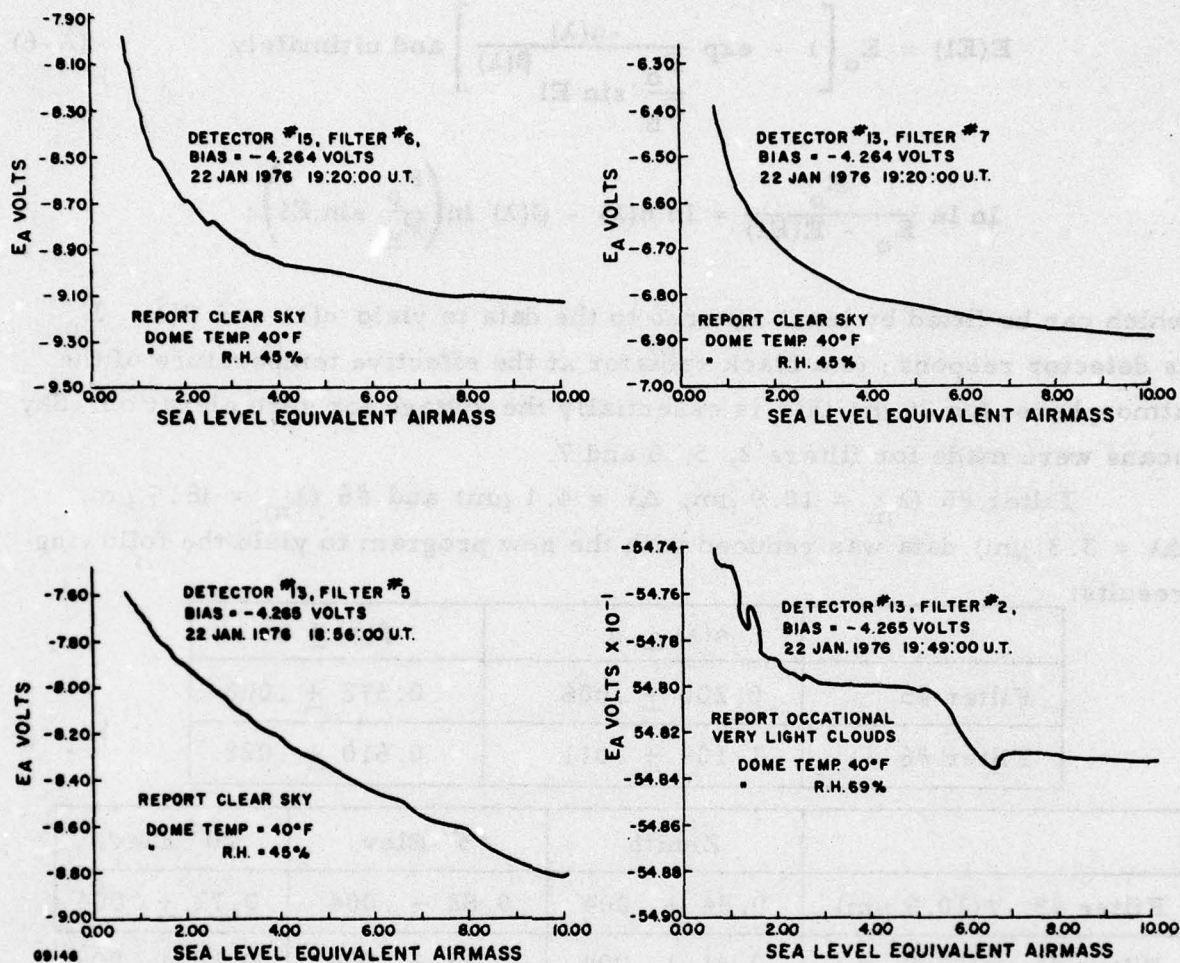


Figure A-7 Air Mass Related to Detector Output



$$E(E1) = E_o 1 - \tau(\lambda) ,$$

$$E(E1) = E_o \left[ 1 - \exp \frac{-\alpha(\lambda)}{\frac{P_o}{P_h} \sin E1} \beta(\lambda) \right] \text{ and ultimately} \quad (A-6)$$

$$\ln \ln \frac{E_o}{E_o - E(E1)} = \ln \alpha(\lambda) - \beta(\lambda) \ln \left( \frac{P_o}{P_h} \sin E1 \right);$$

which can be fitted by least squares to the data to yield  $\alpha(\lambda)$  and  $\beta(\lambda)$ .  $E_o$  is detector response to a black radiator at the effective temperature of the atmosphere; for 20  $\mu\text{m}$  this is essentially the voltage for zero elevation. Sky scans were made for filters 2, 5, 6 and 7.

Filter #5 ( $\lambda_m = 10.9 \mu\text{m}$ ,  $\Delta\lambda = 4.1 \mu\text{m}$ ) and #6 ( $\lambda_m = 18.9 \mu\text{m}$ ,  $\Delta\lambda = 3.3 \mu\text{m}$ ) data was reduced with the new program to yield the following results:

	$\alpha(\lambda) \pm \sigma$	$\beta(\lambda) \pm \sigma$
Filter #5	$0.200 \pm .006$	$0.372 \pm .008$
Filter #6	$1.109 \pm .011$	$0.610 \pm .028$

	Zenith	45° Elev.	20° Elev.
Filter #5, $\tau(10.9 \mu\text{m})$	$0.84 \pm .004$	$0.82 \pm .004$	$0.77 \pm .004$
Filter #6, $\tau(18.9 \mu\text{m})$	$0.41 \pm .004$	$0.33 \pm .004$	$0.18 \pm .008$
Air Masses	0.704	0.996	2.058

The values and scatter for  $\alpha(\lambda)$  and  $\beta(\lambda)$  are the averages for five detectors; Eq. (A-5) was used to compute transmission.

The sensor was calibrated with a precision black body and then observations were made of the apparent 10.9  $\mu\text{m}$  and 18.9  $\mu\text{m}$  brightness of the IR star, NML Cygnus, at 47° elevation. Using the average of eight exoatmospheric brightness values, from astronomical literature, yielded transmission of 0.77 and 0.30 for filters 5 and 6, respectively; this should be compared to the 45° values deduced from radiance gradient data. Published brightness



values span 28% about the mean. \*\* Since this is typical for IR stars, extinction is more properly determined by following a single star as it sets through two or more air masses, or by observing several "standard" stars at different zenith distances. But there are very few well observed IR stars with N and Q brightness uncertainties small (compared to transmission uncertainties) listed in the catalogs. Following rising/setting stars entails telescope time, which was not available in the press of other work, and in any event yields chancy results with changing weather.

Filter #2 ( $5 \mu\text{m}$ ) and filter #7 ( $18 \pm 0.8 \mu\text{m}$ ) data from 22 January and more data filters #5 and #6 obtained during changing weather on 11 February 1976 and being analyzed. A total of seven sets of additional sky scans plus accompanying calibrations have been requested.

---

\*\* Note that the ratio of  $\tau(18.9)/\tau(10.9)$  reduced from radiance measures and from star data agree very closely: 0.39 and 0.40 respectively; the apparent temperature of NML Cyg is better known than its brightness.

(The reverse of this page is blank)

#### 4.0 MEASURING PRECISION CONSTRAINTS

To improve immunity to the AMOS EMI environment, some long term drift problems attributed to cabinet temperature changes and common mode response problems, hardware modifications described during the 19 February briefing are being implemented. Fabrication is 20% complete and an additional twenty man days of labor should suffice to complete this work.

The sky scan data produced verification of the long reported belief that radiant structure in the atmosphere limits the sensitivity of a fast-slewing radiometer. Wind driven eddies are observed at AMOS even when tracking stars; F. J. Low<sup>(7)</sup> refers to 'sky noise' which is probably the same thing. The sky scan measuring procedure in January involved moving the telescope up from the horizon to zenith in an orderly series of stepstare operations. Detector resistance (d.c. voltage) was recorded for five channels in order to chart the relation between apparent brightness and zenith distance as explained earlier. The highly amplified a.c. outputs were recorded too. This was done to provide data relating NEFD to zenith distance, a sort of no-effort aside to the primary measurement. It turned out that deviation about the mean background was consistently higher for 'step' than for 'stare'. Standard deviation of the recorded background was converted to equivalent entrance aperture flux by relating to the output voltage change produced by the black body reference source. The results are plotted in Figure A-8. The dotted trace is a least-squares fit to the 'stepping' data; the solid curve, which ties the 'stare' points together, is calculated for 'still-air' sky and shifted upward a factor of six. Note that above 40° elevation moving the telescope produces a factor of two more 'uncertainty', but conditions wherein motion makes no difference do exist here while, at lower elevation, motion consistently degraded measuring precision. On rare occasions measurements near zenith with a fixed telescope have yielded  $2.5 \times Z$  NEFD. The results shown with slewing help to explain why data from satellites in low orbit and data obtained at low elevation is so unexpectedly 'ragged'. Experiments for characterizing the spatial frequency density distribution of radiant atmospheric structure (Weiner spectrum measurements) have been discussed.



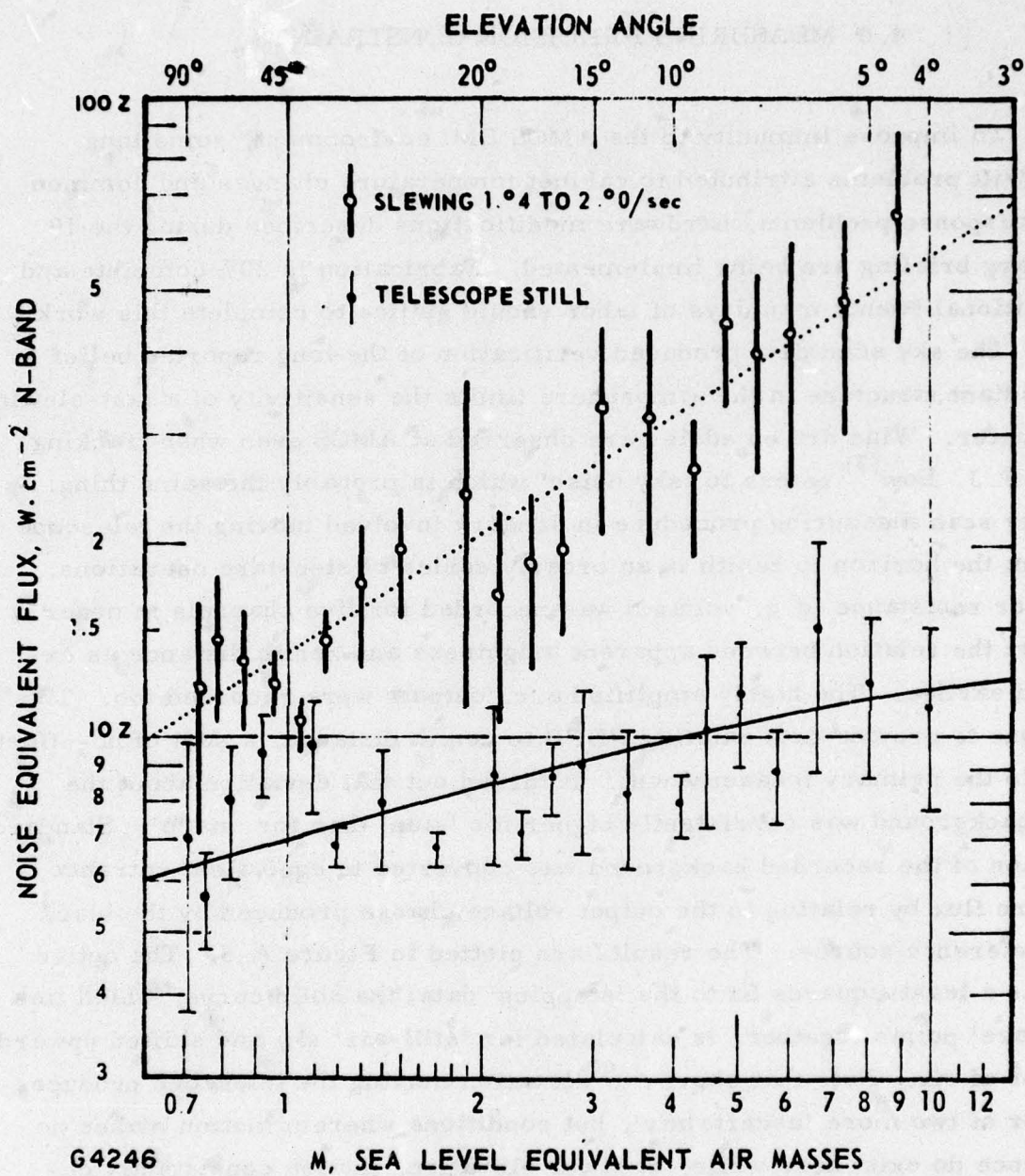


Figure A-8 Sensitivity with Slewing



As self-scanning (CCD, CID, etc) focal planes develop and extremely populous arrays become practical, real time clutter cancellation becomes a distinct possibility. Dave Fried has suggested that, if detector spacing is at least twice as fine as the finest significant atmospheric clutter, the clutter in the track direction is completely defined and its interference with a stationary target becomes surmountable. Weiner spectrum information is needed to define the required pixel and frame rate scaling.

(The reverse of this page is blank)

APPENDIX A  
REFERENCES

1. This reference will be made available to qualified military and government agencies on request from RADC (OCSE) Griffiss AFB NY 13441.
2. This reference will be made available to qualified military and government agencies on request from RADC (OCSE) Griffiss AFB NY 13441.
3. University of Michigan report #IRIA 2389-7-X (July 1957).
4. D. Korff, private communication.
5. J. Heath, AMOS Star Library, Lockheed Missiles and Space Company, Inc. (April 1974).
6. F. J. Low, Sky Survey, Semi-Annual Technical Report, AFCRL #70-0179, Univ. of Arizona (15 March 1970).
7. N. Carleton (editor), Methods of Experimental Physics, Vol. 12, Astrophysics, p. 453, Academic Press, N.Y. (1974).
8. D. Hoffleit, Catalog of Bright Stars, 3rd Ed. Yale University Observ. (1964).
9. C. W. Allen, Astrophysical Quantities, 3rd Ed. p. 206, Univ. of London, Athlone Press (1973).
10. American Ephemeris and Nautical Almanac for 1976, U.S. GPO.

(The reverse of this page is blank)



## APPENDIX B

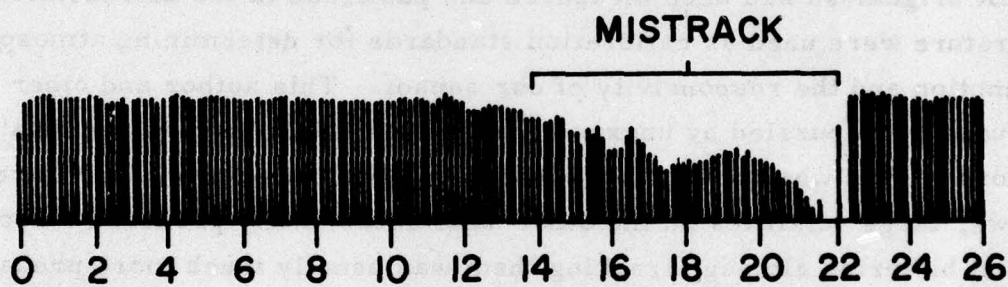
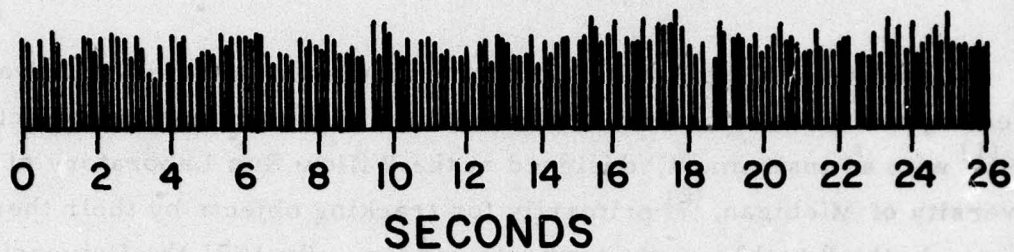
### TWINKLE

Observers at the AMOS facility began making infrared observations of reentry vehicles, artificial earth satellites and astronomical objects in 1969<sup>(1)</sup> with an instrument, designed at the Willow Run Laboratory of the University of Michigan, <sup>(2)</sup> primarily for tracking objects by their thermal exitance in the 8 to 13  $\mu\text{m}$  atmospheric window. By 1971 the University of Michigan Tracker (UMT) had developed to the point where satellite and celestial object measurements were made routinely with it. Stars whose LWIR brightness had been measured and published in the astronomical literature were used as calibration standards for determining atmospheric extinction and the responsivity of our sensor. This author and other observers were puzzled by unexpectedly ragged LWIR 'calibration data' recorded even when bright stars were accurately tracked. As Figure B-1 shows, large satellites on the other hand occasionally produced smooth signal histories although tracking them was usually much more precarious. In the figure, the series of pulses is produced in each case by the image sweeping across the detector field of view stop approximately twelve times per second. The field stop contains a picket fence reticle pattern which periodically occults the image during each sweep producing a short burst of 1.4 millisecond pulses which are averaged to result in a single pulse, approximately 30 milliseconds wide, once per sweep.

AMOS analog records of infrared star observations generally contain random amplitude fluctuations three to ten times more prominent in the 8-13  $\mu\text{m}$  atmospheric transmission window than in the visible. We refer to

- 
1. This reference will be made available to qualified military and government agencies on request from RADC (OCSE) Griffiss AFB NY 13441.
  2. This reference will be made available to qualified military and government agencies on request from RADC (OCSE) Griffiss AFB NY 13441.





D9508

Figure B-1 Pegasus IR Twinkle

observations made with the same size (48-inch) collecting aperture; signal history features which endure from ten to several hundred milliseconds and detectors much larger than the image diameter for both wavelengths. Because the IR intensity fluctuations (actually voltage fluctuations) were much more prominent than baseline noise and appear to increase monotonically with atmospheric path length more rapidly than attenuation scaling will account for, they are attributed to scintillation produced by atmospheric refraction structure even though theory predicts little or no difference should be observed between 0.5 and 10  $\mu\text{m}$ . Figure B-1 is a chart recording of the processed output of a UMT detector made during observation of the infrared object NML Cyg (upper trace) and the Pegasus U. S. satellite, SDC #1384. The 'star' is assumed to produce a  $\lambda/D$  point image while Pegasus subtends over eight arcseconds; strikingly different voltage fluctuations are evident. Observations similar to those typified by Figure B-1 led to the notion that object size information might be embedded in endo-atmospheric irradiance fluctuation statistics. Determining whether the observed radiation arises from the object as a whole or largely from some small portion is of interest.

Actually, the observed fluctuations may be attributed to any of the following causes: (a) system noise; (b) line-of-sight wander; or (c) atmospheric propagation effects. In addition, the difference between earth satellite and stellar variance may be due to the signal conditioning equipment which includes an integrator to smooth out high speed signal changes; the line-of-sight moves 100 to 300 times sidereal rate for near-in satellites. We have concluded, however, from observational evidence summarized here, that the fluctuations are probably due to 'twinkle' that is to say: distant refraction features in the turbulent atmosphere producing interference between light rays arriving at the telescope via slightly different paths.

With regard to (a) noise, note in Figure B-1 that although the star (upper) trace is written with twice the deflection gain of the Pegasus record, this in itself cannot account for the smoothness of the latter. Also, in the mistrack region at 21.8 seconds, the background noise is lost in the baseline. It is therefore evident that peak signal fluctuations are not due to instrument noise or radiant atmosphere interfering with target flux. Moreover,



it is easily shown that satellite photon exitance statistics cannot account for such large variations. Figure B-2 for example relates noise-in-signal to target size and range for surfaces in equilibrium with insolation and earth-shine. For Pegasus, with  $\epsilon A \approx 30 \text{ meters}^2$  observed at 400 km, noise-in-signal produces a negligible fraction of the observed fluctuation. Finally, if system and background noise are important and relatively constant contributors, normalized fluctuation ought to be inversely proportional to target irradiance. This, however, does not appear to be the case as illustrated in Figure B-3. In the figure normalized standard deviation,  $M$ , measured during observations of a number of infrared stars, is related to their known brightness; there is not enough correlation exhibited to confidently tie the two parameters together.

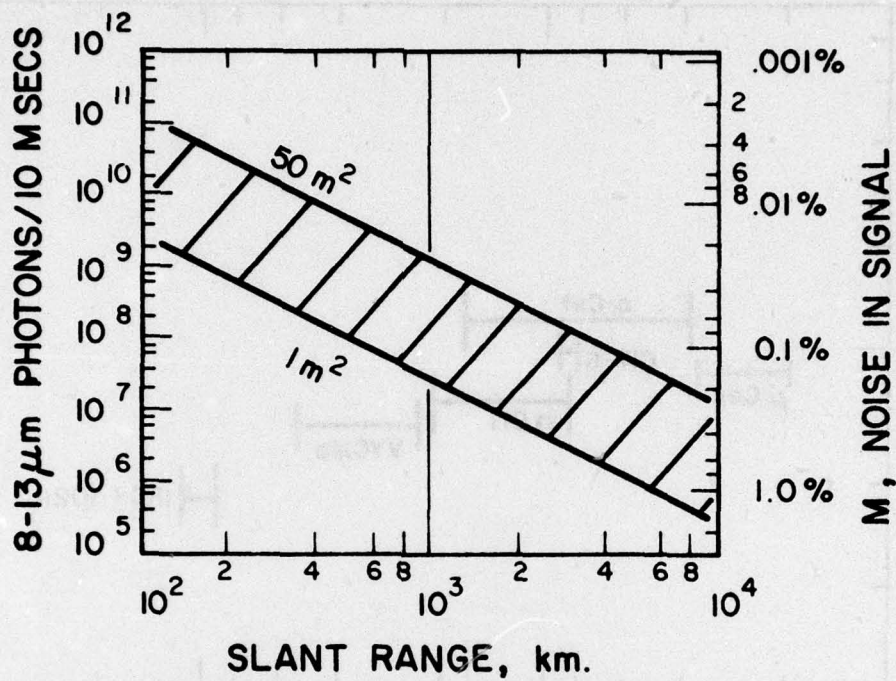
Line-of-sight wander or random mistracking convolved with detector sensitivity contours, might also account for fluctuation but this is unlikely with UMT. The tracker is fitted with field lenses to provide a 'Maxwellian field-of-view' for each detector. These lenses image the telescope entrance pupil onto the semiconductor surface such that, in principle, the position and intensity profile of the pupil image is constant and independent of the target image within the field-of-view stop. While principle was imperfectly reduced to practice in this case, ten arcseconds of wander would be required<sup>(3)</sup> to account for the observed stellar twinkle. Ten arcseconds wander might be produced by disturbance torques due to wind gusts buffeting the telescope but winds in excess of 25 knots would be required and observations are rarely attempted under such conditions.

Twinkle strength should be related to atmospheric path length and Figure B-4, which ties  $M\%$  to zenith distance for various stars observed with UMT, shows just such relation. Atmospheric transmission dependence is not severe enough ( $\tau = \exp(-0.1 m)$ , where  $\tau$  is 8-13  $\mu\text{m}$  transmission and  $m$  is air mass) to account for the observed trending. Unfortunately, weather information is unavailable to factor into these observations, note, for example, the NML Cyg measures for 28 February shown in the figure

---

3. Loc cit 1, p. 117





D9509

Figure B-2 Satellite Observation Noise-In-Signal

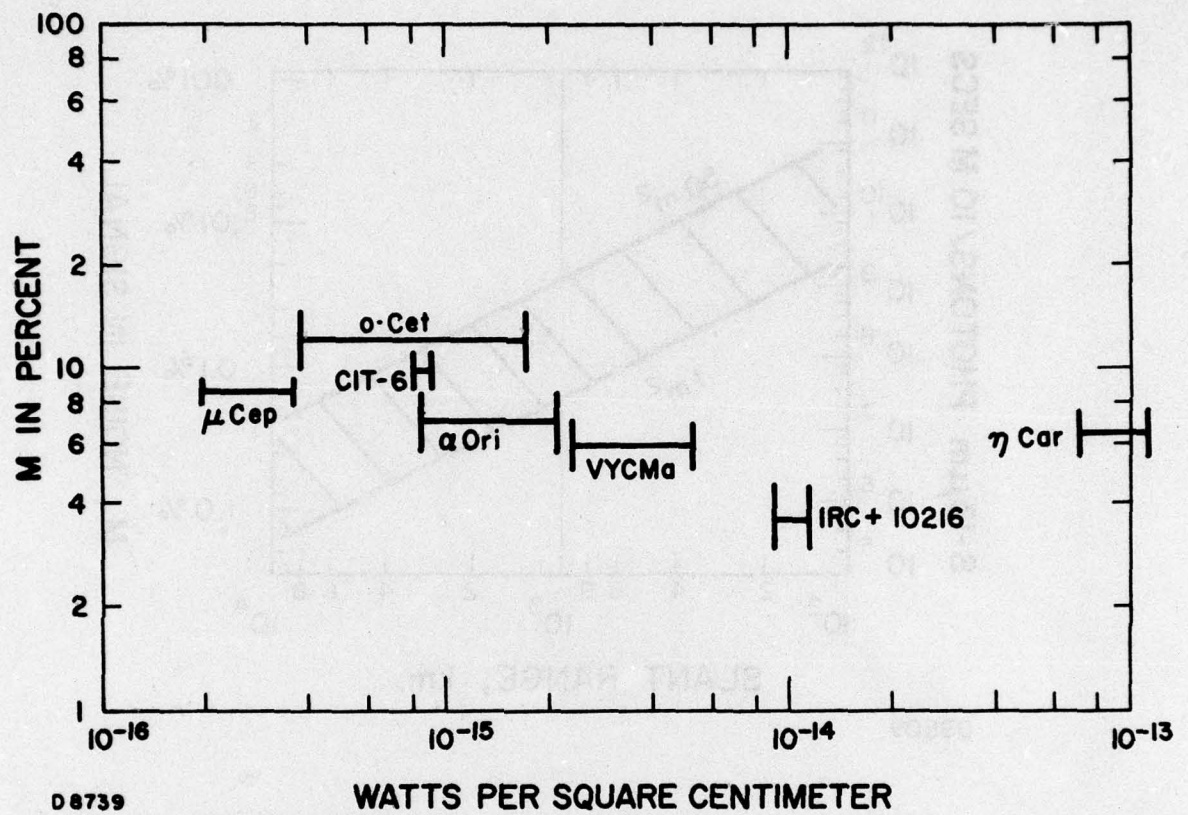


Figure B-3 Stellar Scintillation Related to Irradiance



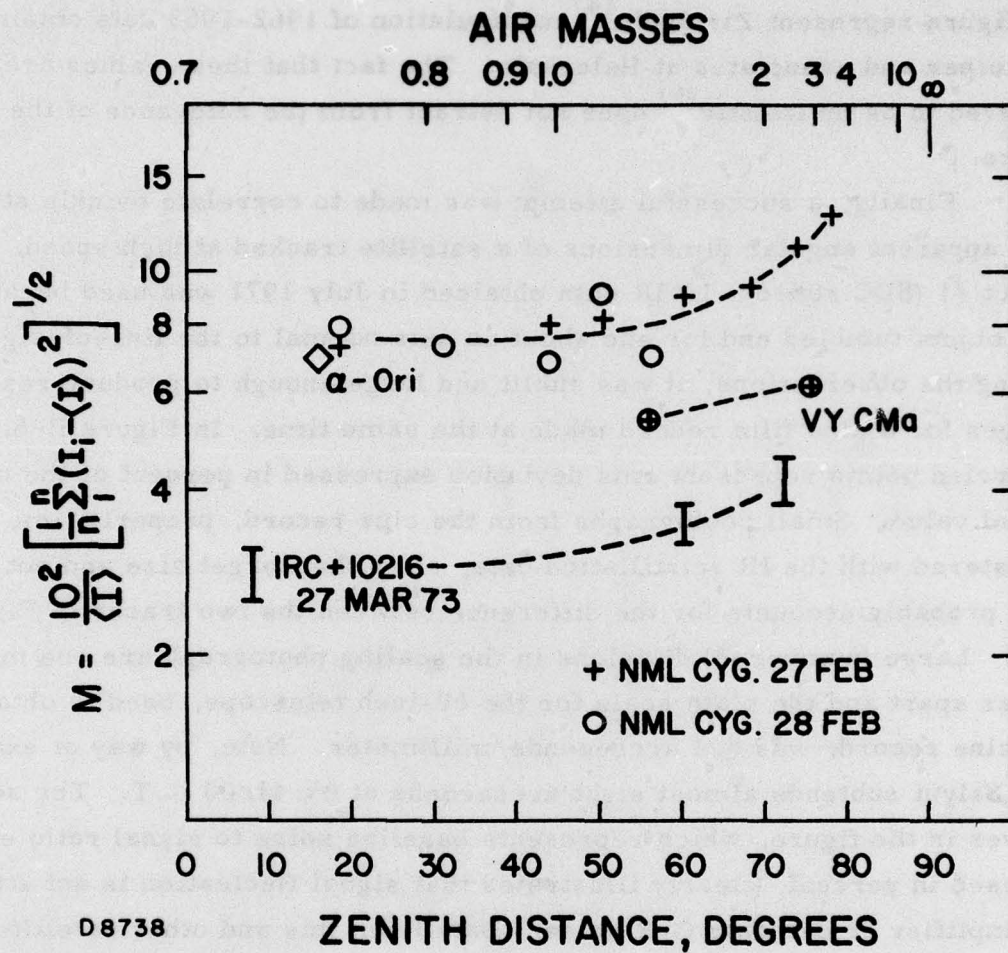


Figure B-4 Stellar Scintillation Related to Zenith Distance

illustrate that weather changes may override path length dependence on an hour by hour basis. Generally February and March are not auspicious months for observations as illustrated in Figure B-5. [Small circles in the figure represent Zirkind's<sup>(4)</sup> manipulation of 1962-1963 data obtained by Kuiper and associates at Haleakala. The fact that these values are now believed to be optimistic<sup>(5)</sup> does not detract from the relevance of the figure. ]

Finally, a successful attempt was made to correlate twinkle strength with apparent angular dimensions of a satellite tracked at high speed. Salyut #1 (SDC #05160) LWIR data obtained in July 1971 was used because this object tumbled end for end about an axis normal to the line-of-sight during the observations; it was sunlit and large enough to produce resolved images for a cine film record made at the same time. In Figure B-6, the encircled points represent rms deviation expressed in percent of the mean signal value. Small photographs from the cine record, properly time registered with the IR scintillation data, show that target size and not track rate probably accounts for the difference between the two traces in Figure B-1. Large (numbered) divisions in the scaling photograph are one millimeter apart and the plate scale for the 60-inch telescope, used to obtain the cine record, was 8.4 arcseconds/millimeter. Note, by way of example, that Salyut subtends almost eight arcseconds at 05:41:00 U. T. The solid curves in the figure, which represents baseline noise to signal ratio expressed in percent, clearly illustrates that signal fluctuation is not attributable to amplifier or detector G-R noise. Data from this and other satellite observations were combined to produce the dashed curve in Figure B-7 which relates twinkle strength to object size.

---

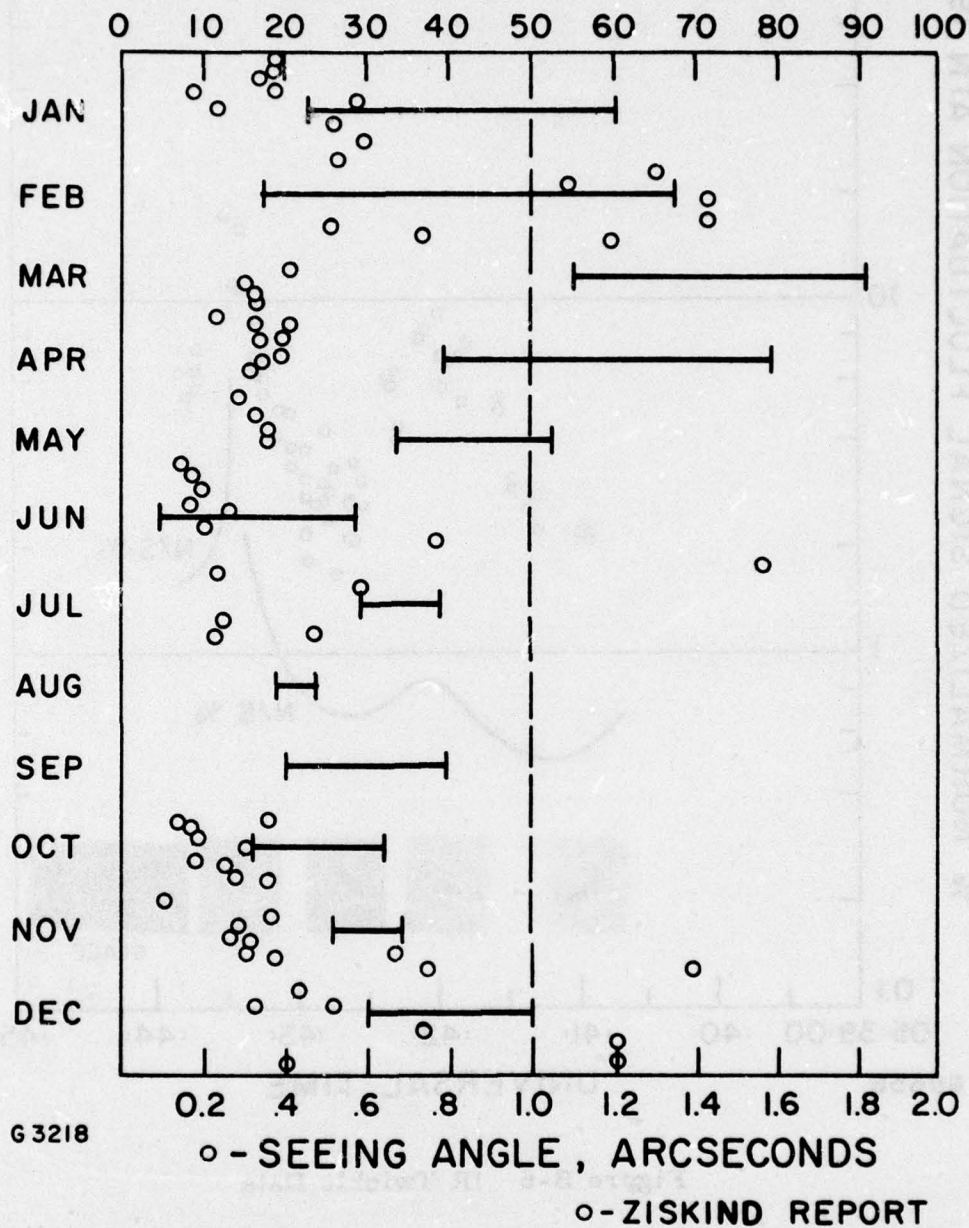
4. Zirkind, R., Project AMOS: An Infrared Observatory, Ap. Opt. 4, #9 p. 1077 (September 1965).

5. Miller, M. and Kellen, P., Turbulence Characterization and Control, RADC-TR-75-185, p. 5 (July 1975).



1962 - 1971

% OF MISSIONS COMPROMISED BY WEATHER



G 3218

Figure B-5 AMOS Weather

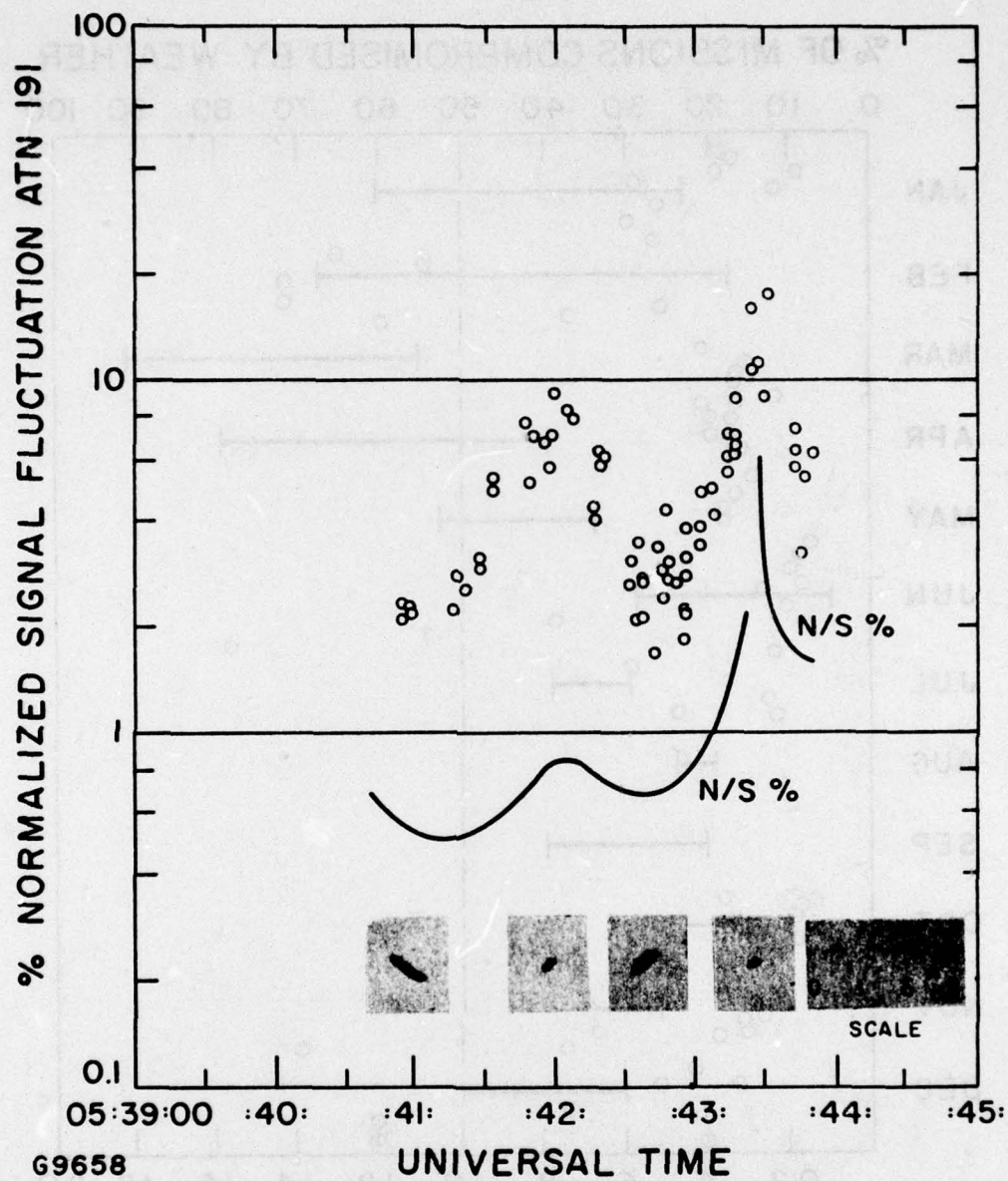


Figure B-6 IR Twinkle Data



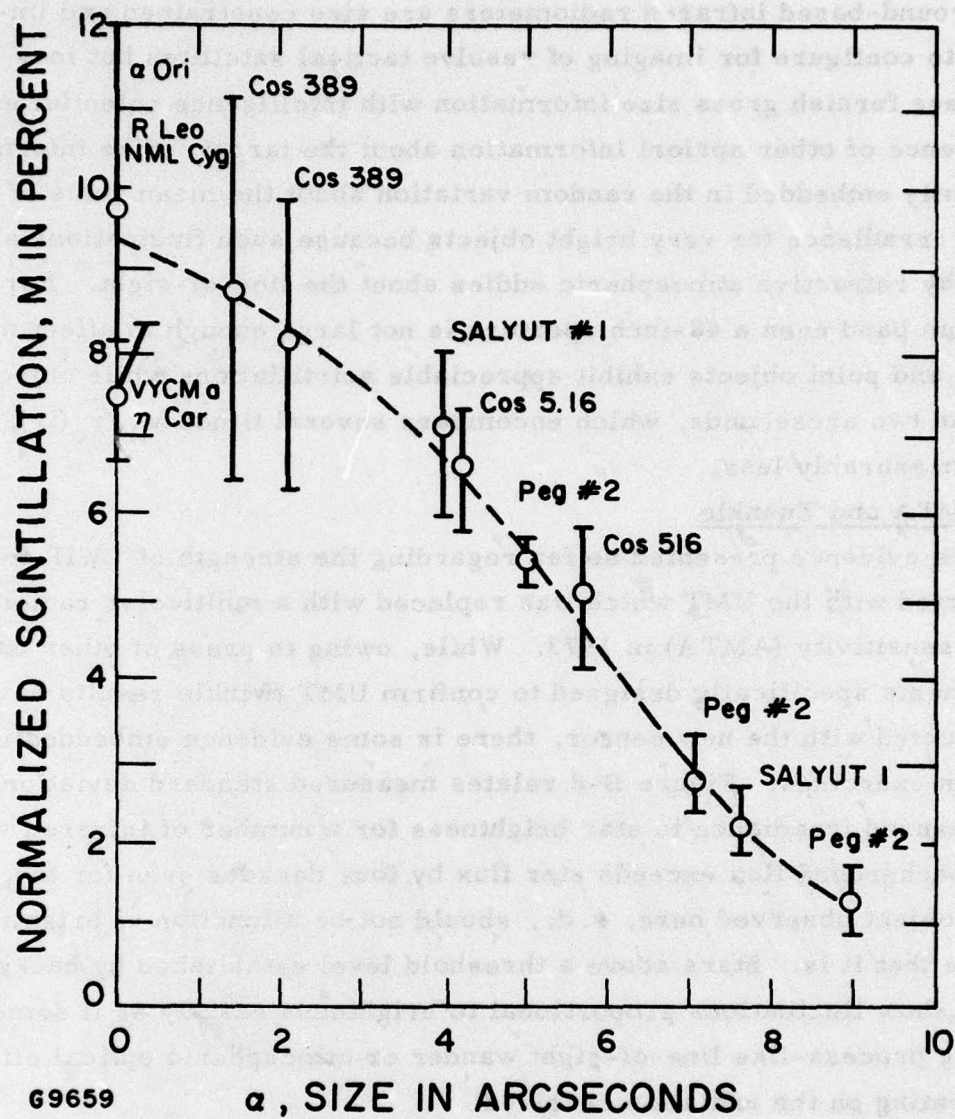


Figure B-7 Target Sizing with IR Twinkle

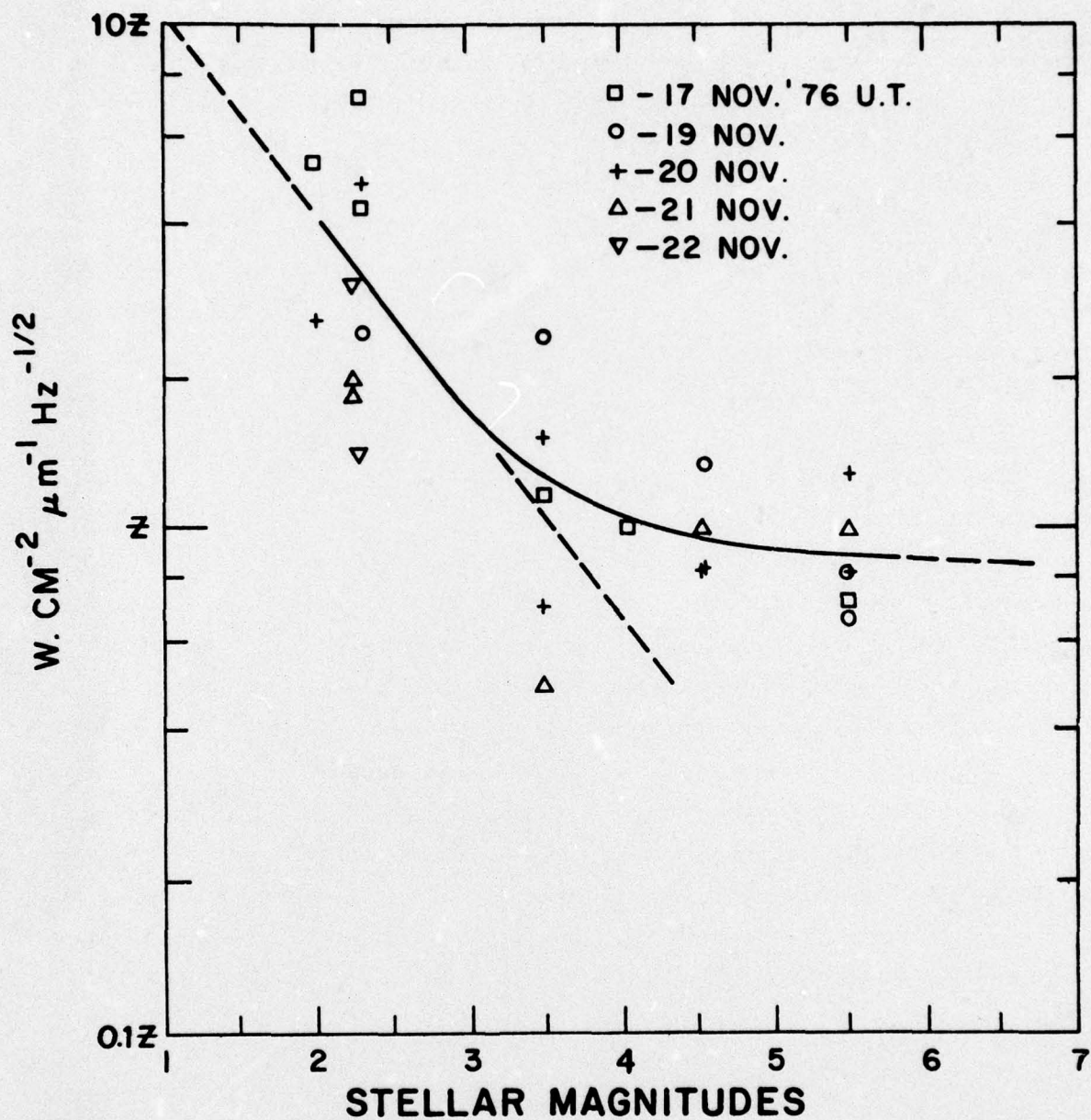
### Conclusions

Ground-based infrared radiometers are size constrained and impractical to configure for imaging of resolve tactical satellites but may nevertheless furnish gross size information with intelligence potential even in the absence of other apriori information about the target. Size information is apparently embedded in the random variation about the mean value of the measured irradiance for very bright objects because such fluctuations are produced by refractive atmospheric eddies about the line-of-sight. For the 8-13  $\mu\text{m}$  band even a 48-inch aperture is not large enough to affect much averaging and point objects exhibit appreciable scintillations while objects larger than two arcseconds, which encompass several times  $\lambda_{\text{ir}}/r_o(\text{ir})$ , produce measurably less.

### AMTA and Twinkle

The evidence presented so far regarding the strength of LWIR twinkle was collected with the UMT which was replaced with a multicolor radiometer of higher sensitivity (AMTA) in 1973. While, owing to press of other business, measurements specifically designed to confirm UMT twinkle results have not been conducted with the new sensor, there is some evidence embedded in calibration exercises. Figure B-8 relates measured standard deviation about measured irradiance to star brightness for a number of infrared stars. Because background flux exceeds star flux by four decades even for the brightest object observed here, s. d., should not be a function of brightness, yet we see that it is. Stars above a threshold level established by background statistics show fluctuations proportional to brightness exactly as if some modulating process-like line-of-sight wander or atmospheric optical effects were operating on the radiation received.





G9663

Figure B-8 NEFD Related to Object Brightness

## APPENDIX B

### REFERENCES

1. This reference will be made available to qualified military and government agencies on request from RADC (OCSE) Griffiss AFB NY 13441.
2. This reference will be made available to qualified military and government agencies on request from RADC (OCSE) Griffiss AFB NY 13441.
3. Loc cit B1, p. 117.
4. Zirkind, R., Project AMOS: An Infrared Observatory, Ap. Opt. 4, #9 p. 1077 (September 1965).
5. Miller, M. and Kellen, P., Turbulence Characterization and Control, RADC-TR-75-185, p. 5 (July 1975).

(The reverse of this page is blank)



**MISSION**  
**of**  
**Rome Air Development Center**

RADC plans and conducts research, exploratory and advanced development programs in command, control, and communications (C<sup>3</sup>) activities, and in the C<sup>3</sup> areas of information sciences and intelligence. The principal technical mission areas are communications, electromagnetic guidance and control, surveillance of ground and aerospace objects, intelligence data collection and handling, information system technology, ionospheric propagation, solid state sciences, microwave physics and electronic reliability, maintainability and compatibility.

